Alma Mater Studiorum - Università di Bologna

DIPARTIMENTO DI CHIMICA "G. CIAMICIAN"

Dottorato di Ricerca in SCIENZE CHIMICHE

Ciclo XXVII

Settore concorsuale di afferenza: **03/A2**

Settore scientifico-disciplinare: **CHIM/02**

Simulation of Smart Materials

Presentata da **Micaela Matta**

Coordinatore Dottorato   **Relatore**

Prof. Aldo Roda   Prof. Francesco Zerbetto

Esame Finale Anno 2015

Contents

Summary

Organic electronic devices have undoubtedly been the protagonist of the last decades of materials chemistry research. With this respect, impressive advance on the development of nanofunctional materials for organic electronic applications has been made. Despite initial skepticism regarding the performances of such systems, organic-based electronic devices are now appearing on the market: flexible displays, electronic paper, bio-compatible sensors, only to name a few.

If, on one hand, nanofabrication, microscopy and organic synthesis have contributed to fill the performance gap between organic electronic devices and their inorganic homologues, there are still many unknown variables affecting both efficiency and durability of such devices. This is particularly true for Organic Solar Cells (OSCs) and Organic Field Effect Transistors (OFETs).

Overcoming these obstacles is possible, if experimental and theoretical efforts are put together in a virtuous cycle: prior computational screening of possible molecular candidates for future devices is followed by fabrication and characterization, then ex post modelling to interpret experimental results and help in identifying possible bottlenecks. A wise use of computational simulations of organic electronic materials represent thus an inexpensive and faster way of increasing our control over the wide range of variables while developing marketable devices.

Within this framework, the aim of this thesis is the elucidation of structure-properties relationship of molecular semiconductors for electronic devices. This involves the use of a comprehensive set of simulation techniques, ranging from quantum-mechanical to numerical stochastic methods, and also the development of ad-hoc computational tools. In more detail, the research activity regarded two main topics: the study of electronic properties and structural behaviour of liquid crystalline (LC) materials based on functionalised oligo(p-phenyleneethynylene)

3

(OPE), and the investigation on the electric field effect associated to OFET operation on pentacene thin film stability.

A short overview of this dissertation is henceforth presented.

The first chapter contains a general description of organic semiconductors and related devices, focusing on OFETs and OSCs. The basic rules governing their operations, the issues limiting their diffusion, together with the key strategies employed to overcome them are discussed. Particular emphasis is put on liquid crystalline materials as solution-processable, ordered self-assembled for "smart" materials.

In Chapter 2, the theory behind the computational models used or developed in this thesis is presented. Electronic structure methods, particularly DFT, are used to characterize both ground and excited state properties of conjugated molecules. Molecular mechanics allows instead to simulate bigger system by neglecting electronic motion, such as thin film layers or liquid crystalline supercells. Moreover, numerical simulations based on Monte Carlo algorithms can instead model the evolution of nano-scale objects, using a stochastic description which overpasses molecular detail, e.g, exciton dynamic simulations.

Chapter 3 contains a short background on molecular exciton and aggregates theories; it focuses on the photophysical properties of excimers and J-H aggregates.

The fourth chapter deals with the spectroscopic, structural and computational characterization of a novel family of substituted OPE liquid crystals, as potential thermochromic materials; this work has been carried out in collaboration with the CNRS in Strasburg and the group of Prof. Ceroni at the University of Bologna. In more detail, the simulations can not only provide evidence for the characterization of the liquid crystalline phases of different OPEs, but elucidate the role of charge transfer states in donor-acceptor LCs containing an endohedral metallofullerene moiety. Such systems can be regarded as promising candidates for organic photovoltaics. Furthermore, exciton dynamics simulations are performed as a way to obtain additional information about the degree of order in OPE columnar phases.

In Chapter 5, ab initio and molecular mechanics simulations are used to investigate the influence of an applied electric field on pentacene reactivity and stability. The reaction path of pentacene thermal dimerization in the presence of an external electric field is investigated; the results can be related to the fatigue effect observed in OFETs, that show significant performance degradation even in the absence of external agents. In addition to this, the effect of the gate voltage on a pentacene monolayer are simulated, and the results are then compared to X-ray diffraction measurements performed for the first time on operating OFETs. This work is the result of a collaboration with the groups of Prof. Milita and Prof. Biscarini, respectively at CNR IMM and University of Modena and Reggio Emilia.

The Conclusion offers a general perspective of the obtained results and future

developments of the present work.

The key ideas and context of a project started during the last year of this PhD are reported in the Perspectives, the final chapter of this dissertation. This work in progress involves the study of a self-assembled system of protonated porphyrins and carbon nanotubes (CNTs), that is characterized by interesting photophysical properties and is a promising material for photovoltaic applications.

Chapter 1

Organic electronics

This chapter focuses on molecular semiconductor-based electronic devices. The properties of organic semiconductors, which are determined by their aromatic structure, are illustrated; they represent an attractive alternative to inorganic materials because of their low cost of production and processing, their tunability, and the possibility of fabricating flexible devices.

The key concepts governing the operation of two of the most employed and studied devices, organic field-effect transistors (OFETs) and organic solar cells (OSCs), are then introduced. Both systems rely on charge separation and migration phenomena; in OFETs this is caused by the applied electric field, while in OSCs it is due to photoexcitation of a species (the donor) which then gives electron transfer to a second one (the acceptor). In the following sections, the most important issues and bottlenecks regarding further development of these devices are briefly discussed.

Furthermore, the properties of liquid-crystals (LC) are presented, as well as their application in mechanocromic, thermochromic and photovoltaic materials. These systems represent an elegant and efficient solution to the need of long-range order and microsegregation in photovoltaic devices. Another section is dedicated to carbon nanomaterials, in particular fullerenes and carbon nanotubes, which are being intensely investigated as electron acceptors for OSCs.

Finally, a general introduction on computational modelling of organic-based electronic devices is presented.

1.1 Organic semiconductors

Organic semiconductor materials include a broad library of π-conjugated molecules and polymers(see Figure 1.1); they are divided in two categories, according to whether their charge carriers arise from removal of electrons from the manifold of filled π molecular orbitals or from the addition of electrons to empty π orbitals, respectively. The former are called hole-transporting materials or p-type (positive charges, HT) semiconductors, and have both low ionization potentials and electronic affinities; the latter are called electron-transporting materials or n-type (negative charges, ET) semiconductors, and are characterized by high ionization potential and electronic affinity. Some characteristic organic semiconductors are shown in Figure 1.1.

As might be already clear from the above definitions, these materials do not have free charge carriers unless they are exposed to an electric field, as in OFETs or OLEDs (Organic Light Emitting Diodes), or photoexcited, as in OSCs. [1] Differently from their inorganic counterparts, in organic semiconductors molecules only weakly interact via Van der Waals forces; therefore there are no energy bands, but charges are localized on (portions of) single molecules and are generally associated with a certain degree of structural distortion. Within this framework, charge transport can be described as a series of successive electron-transfer reactions between neutral and charged units. The charge mobility μ is a measure of the tendency of charges to migrate through the material; it is defined in units of velocity per unit field and is dependent on both the electric field and temperature.

The π-system of conjugated molecules, that accounts for charge-carrier generation and transport, is also responsible for electronic transitions in the UV-Vis-NIR region, which translate in absorption and emission spectra, and non-linear optical properties. These properties, together with flexibility, low cost and tunability make them an advantageous alternative to inorganic semiconductors. Large-area and flexible displays, biomedical or ambient sensors, memories, lighting; these are just some of the potential applications for organic-based devices. Finally, the continuous improvement seen in OPV performances [2] paves the way for the future replacement of their inorganic counterparts.

1.2 Organic field-effect transistors

Although the first patent of a field-effect transistor dates back to the 1930s, it wasn't until the 1980s that the first organic-based devices were fabricated. Since then, researchers have been more and more involved in discovery, design, and synthesis of π-conjugated systems for OFETs, device optimization, and exploitation
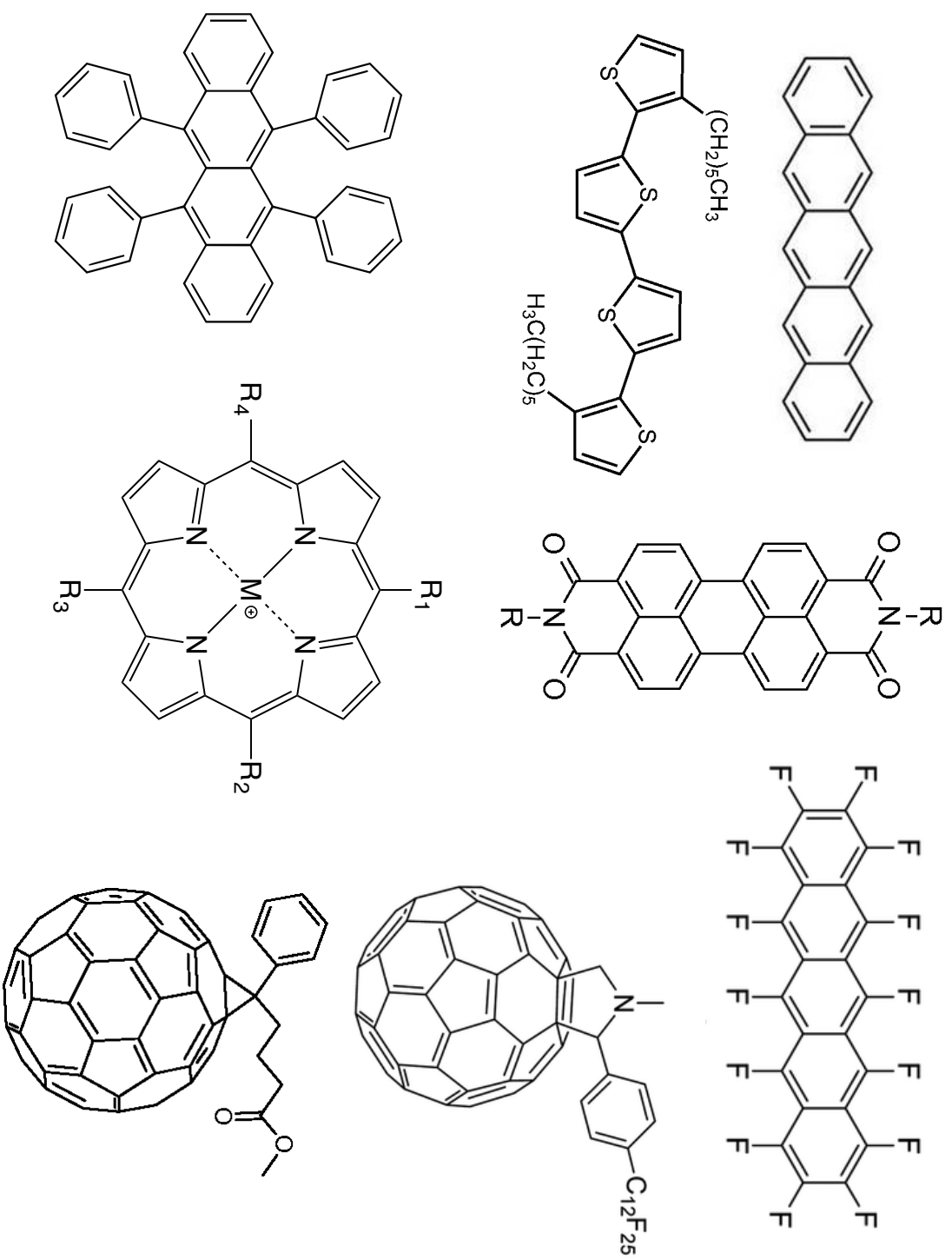
Figure 1.1: Molecular structure of some popular molecular p-type (left) and n-type (right) semiconductors.

of the new possibilities offered by organic materials in terms of flexibility, ease of functionalization, selectivity to different stimuli and bio-compatibility. [3–5]

Organic field-effect transistors (OFETs) are devices whose electric response is based on the application of a voltage on an organic semiconductor layer. Their basic architecture is made of: the organic semiconducting layer, the gate insulator layer, and three electrodes identified as source, drain, and gate (see Figure 1.2). These components can be assembled in different ways, and more layers can be added, but their operation process is essentially the same. When there is no voltage applied to the gate electrode, the transistor is in the off-state and no current flows between the source and drain electrodes. When a negative (positive) voltage higher than a threshold voltage V_T is applied to the gate, hole (electron) carriers in the organic semiconductor layer accumulate at the interface with the gate dielectric, hole (electron) transport from the source to the drain electrode is observed. Such device is called a p-channel (n-channel) device. It is well established that only the first few monolayers of the semiconductor material effectively concur to the current flow. The latter depends on the magnitudes of V_G, V_{SD} and V_T:

$$I_D = \frac{W}{L}\mu C_i \left[(V_G - V_T)V_D - \frac{V_D^2}{2} \right] \tag{1.1}$$

Where I_D is the drain current, W and L represent the semiconducting channel width and length, μ is the mobility and C_i is the capacitance of the dielectric. The main parameters characterizing OFETs performance are: i) μ, the drift velocity of carriers under unit electric field; ii) the current on/off ratio; and iii) the threshold voltage V_T. The latter is related to the minimum voltage required to generate a current flow, and is found to change over time: this effect is known as bias stress and it has been generally ascribed to the charge trapping, either within the semiconductor, at the semiconductor/dielectric interface, or in the gate dielectric. The longer the gate bias is applied, the more carriers are trapped, and hence the larger is the V_T shift. The trapped carriers contribute to the charge balance in the OFET, but not to the drain current.

It has been shown that the longitudinal electrostatic potential generated during OFET operation drops rapidly at grain boundaries; this generates a step-wise electric field profile across the semiconductor channel with essentially zero electric field within domains and intense electric fields across boundaries. [6] In this respect, the molecular packing motif at the grain boundaries affects the charge transport across adjacent crystalline grains, [7] highlighting how charge transport follows pathways dictated by the orientation of adjacent crystalline domains. [8] Consequently, charge carriers move by percolation along grain boundaries.

As a result, the morphology of semiconductor-electrode and semiconductor-dielectric

interfaces is perhaps the most important variable that allows to control the device performances. This is because interfaces represent the main sources of defects in the semiconductor layer, which in turn translate into charge traps and current loss. A significant effort is currently being put into minimizing fabrication defects while developing low-cost printing techniques. This can be achieved, for instance, by changing the substrate temperature or applying an electric field during the sublimation in high vacuum, [9] as well as by applying solvent annealing or thermal gradients during the deposition by solution methods. [10, 11] Other strategies involve the confinement of the region where molecules can interact during the growth, the modification of the dielectric interface, the introduction of lattice strains by using solution-shearing method [12] or the introduction of conformational disorder by modifying the chemical structure. [13]

Another characteristic of OFET devices is the organic semiconductor stability to light, air and water: all these factors can severely reduce the device life and performances. This is true for pentacene-based devices (see Chapter 5), where an encapsulation layer is thus needed to achieve longer lived and stable devices. [14]

In summary, the continuous research on the structural (and consequently, electrical) stability of organic semiconductor layers is expected to yield promising results extending both the operational and shelf life of OFETs under realistic application conditions. [15]

1.3 Organic photovoltaics

Solar cells allow to convert light energy into electrical energy. This broad definition includes dye sensitized solar cells, hybrid organic-inorganic solar cells, and organic donor-acceptor based heterojunction solar cells. [17] In particular, the latter have seen the rapid increase in reported efficiencies, which at the moment have exceeded 10%. [18, 19] An organic pn-heterojunction solar cell typically consists of a thin active organic layer sandwiched between a high work function anode, usually a transparent indium tin oxide (ITO) layer, and a relatively low work function metal cathode. The active layer is made up of two light-absorbing organic semiconductors, one with an electron-donating character (donor) and the other with an electron-accepting character (acceptor). These semiconductors could either be deposited as two distinct layers where the donor-acceptor interface resides only between the two layers, or constitute a mixed phase where interaction between donor and acceptor exists throughout the blended layer. In the latter case, we talk about heterojunction solar cells, which represent the current state of the art in organic photovoltaic devices. Bulk heterojunction devices are obtained mainly through solution processing of a mixture of the two semiconductors, while ordered structures require more sophisticated self-organization of the components. A scheme
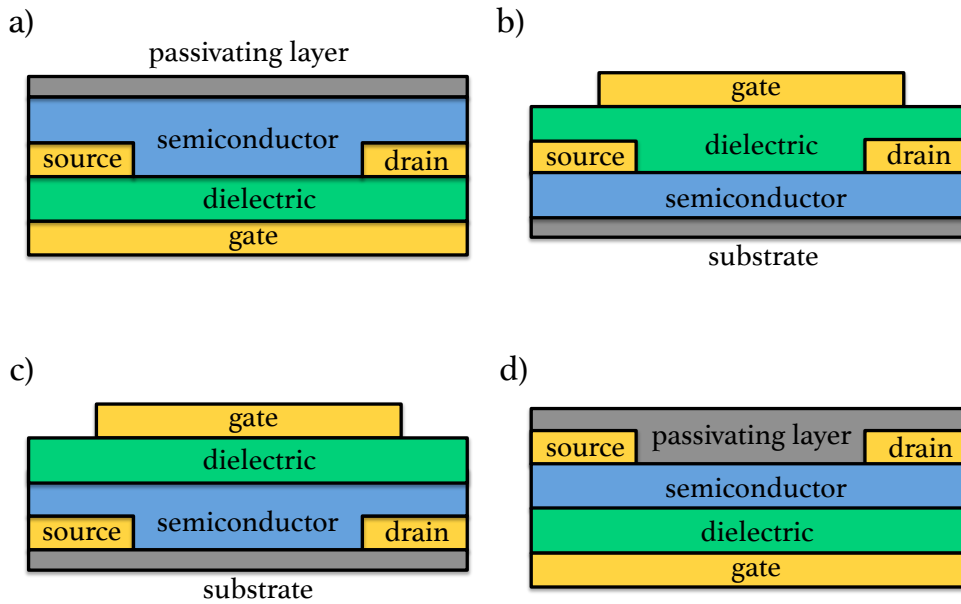
Figure 1.2: Schematic representation of different OFET architectures. a) bottom gate - bottom contact, b) top gate - bottom contact, c) top gate - bottom contact, d) bottom gate, top contact.

of the different architectures is reported in Figure 1.3.

The key steps in the operation of pn-heterojunction OPVs are: (i) light absorption and exciton formation, (ii) diffusion of excitons, (iii) charge carrier generation and separation at the donor/acceptor interface, (iv) charge transport and (v) charge collection at both electrodes (see Figure 1.4). The first step is determined by the portion of the solar spectrum range that is where the donor molecule absorbs light; a common strategy to maximize the coverage of the solar spectrum is to use many complementary chromophores. [20]

However, undesired processes such as exciton quenching phenomena and charge recombination may occur, reducing energy conversion efficiency. In this respect, the morphology of the organic film and the interface has a deep influence. [21] Therefore, two main requirements have to be fulfilled for yielding an efficiently working device. These are: i) long-range order, to favour exciton and charge migration and assure good overlap of the π orbitals; ii) high degree of intermixing between the domains of donor and acceptor moieties, in order to maximize exciton separation efficiency. [22] The distance from the exciton creation site to the heterojunction must be smaller than the exciton diffusion length. As for the first point, crystalline materials seem to be suitable, but grain boundaries and other defects limit orbital overlap and cause charge trapping. Furthermore, obtaining macroscopic single crystals is a
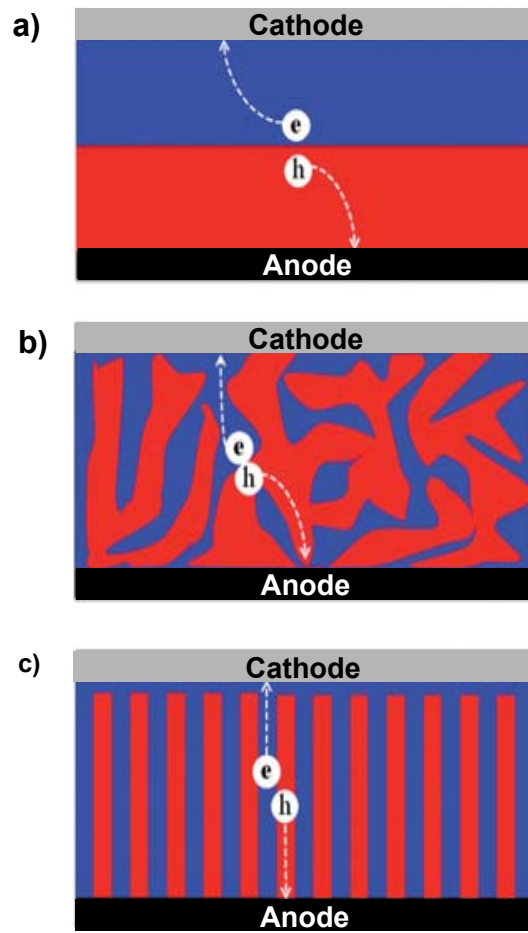
Figure 1.3: Scheme of different p-n solar cells architectures: a) bilayer; b) bulk heterojunction; c) ordered heterojunction. Adapted from [16].
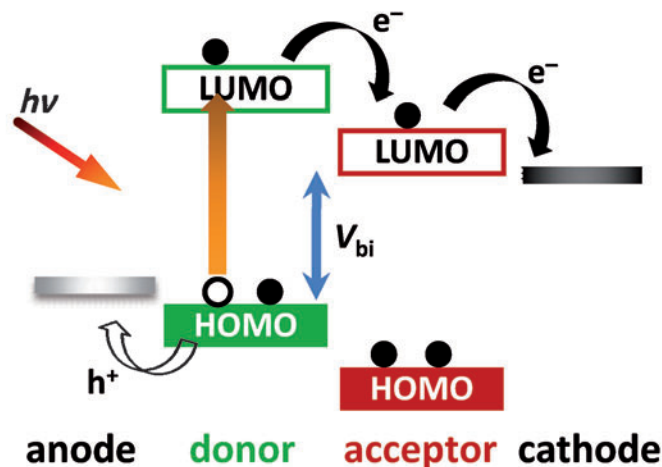
Figure 1.4: Scheme of the fundamental processes in donor-acceptor heterojunction solar cells. Adapted from [2].

strenuous task to achieve, not to mention that device flexibility would be at stake. Finally, to accomplish the second point, the development of new heterojunction paradigms has a key role. In the following sections of this chapter, some possible solutions to these issues will be presented.

1.4 Liquid crystals for organic electronics

The discovery of liquid crystals (LCs) dates back to the 1880s. Since then, mesomorphic materials have been object of a steadily growing interest, that already some years ago met the exponential raise in the research area of organic electronic devices. The two distinctive characteristics of liquid crystals are their fluid-like nature and their long range order - either orientational, positional or both.

For thermotropic LCs - molecules that do not require any other external agent in order to form the liquid crystalline phase - temperature is the main control variable. The mesomorphic phase is confined between the melting point, for $T > T_m$, and the clearance point ($T < T_c$). The typical molecules able to form liquid crystals, defined mesogens, are formed generally by a rigid core (often of aromatic kind, either linear of circular) and flexible terminal chains, usually aliphatic hydrocarbons. However mesogenicity, defined as a system's ability of forming mesogens, is not stricly confined to individual molecules: polymers, functionalised nanoparticles, molecular aggregates are also known to form analogous phases.

Thermotropic LCs can give rise to different phases, depending on the temperature range and classified according to their degree of order. [23, 24] Nematic phases
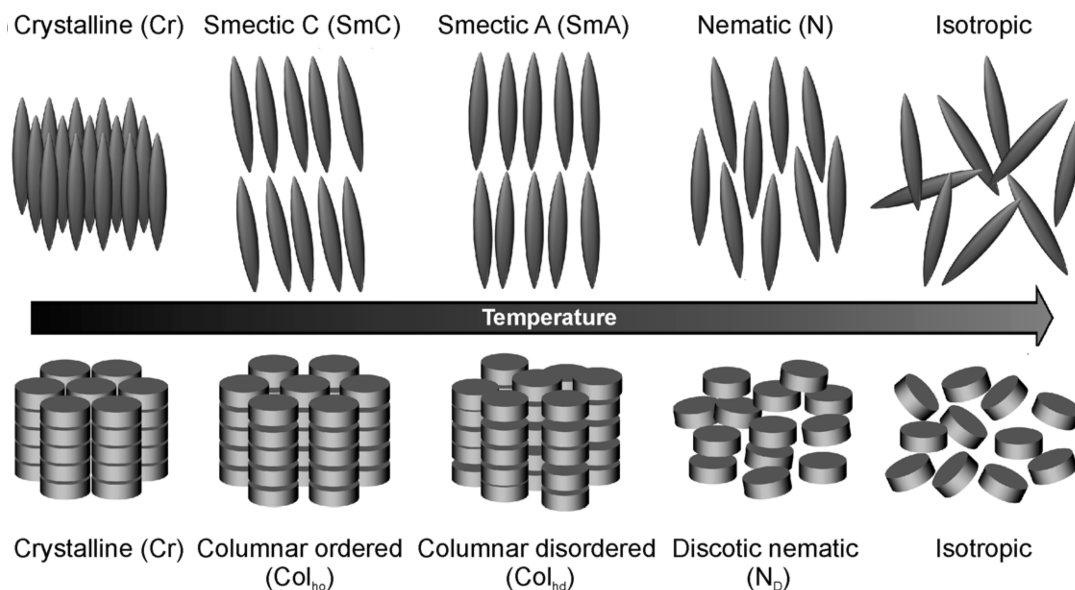
13

Figure 1.5: Scheme of different liquid crystalline phases for discotic and calamitic (rod-like) molecules. Adapted from [24].

are the simplest, as they exhibit orientational but no positional order. Adding 1D positional order, a so-called smectic phase is reached, with mesogens organized in layers but still able to move beneath them. Moving to a 2D lattice we encounter columnar phases, frequently formed by discotic molecules piled up like coins in an hexagonal lattice (see Figure 1.5). These are also the most frequently employed in OE applications. Finally, chiral mesogens form chiral, helicoidal LC phases having a well defined periodicity, known as cholesteric. [25]

In some cases, a change in the LC mesophase can also correspond to a different photophysical behaviour. This is the case of thermochromic and mechanochromic materials, for which the conversion between different states is triggered either by changing the temperature or applying a mechanical stress to the material. [26] Regarding LCs applications in solar cells, it is evident that many π-conjugated species studied for photovoltaic applications are also capable of forming mesophases. [27] The first OSC made from a blend of the discotic liquid crystal hexabenzocoronene and a perylene dye was presented in 2001. [28] As for the role of flexible chains, it was found that longer substituents reduce the efficiency of electron-hole separation, while short side-chains increase the crystallinity as well as the performances. Also, the strategy of mesogen functionalization with suitable electron acceptors has been successfully undertaken, particularly with fullerene derivatives. [29, 30] Besides single molecular properties, however, the main advantage of using mesophases in OPVs is given by the long range order provided by the

LC lattice, which results in an orbital overlap that can virtually be extended over macroscopic distances. Moreover, LCs are very suitable for solution processing, which makes them less expensive compared to other lithographic or vacuum deposition techniques. [31] Furthermore, careful molecular design of homeotropic-aligned heterostructures of donor and acceptor can maximize intermixing and, consequently, charge separation efficiency.

Before concluding, a possible drawback of using liquid crystalline systems for organic electronics must be mentioned. Since molecule mobility in the liquid crystalline state is quite high, it may lead to weaker π-π interactions and thus to limited charge hopping. To overcome this problem, the most promising approach is to rapidly quench the mesophase to lower temperatures, preventing crystallization and reaching a glassy state characterized by both long-range order and small molecular fluctuations. [25, 31]

1.5   Fullerene- and carbon nanotube-based devices

Among the many allotropic forms of carbon, fullerenes, nanotubes and graphene represent respectively the zero-, mono- and bidimensional ones. All three are being exploited in organic electronic applications due to their outstanding mechanical and semiconducting properties.

From the mathematical point of view, fullerenes are convex polyhedra with alternating pentagonal and hexagonal faces. While the first fullerene to be discovered is made of 60 carbon atoms, fullerenes having up to 100 carbon atoms are commonly obtained. [32] Due to their high electron affinity, fullerenes can be classified as mild oxidizing agents; therefore they are suitable as electron acceptors in organic photovoltaic cells and their substituents represent the state of the art in bulk heterojunction solar cells. [33]

Fullerenes can also serve as encapsulating agents for noble gases, rare earths or small molecules; such complexes are known as endohedral (metallo)fullerenes. In some cases, the species forming such complexes are not stable themselves. That is the case of I_h-C_{80} and rare earth nitrides, that yield $M_3N@I_hC_{80}$; these complexes are characterized by notable optical and electronic properties. [34, 35] (See Chapter 4).

Single-wall carbon nanotubes (SW-CNTs) can be seen as rolled-up graphene sheets with a very high aspect ratio. A typical CNT has a diameter of the order of 1 nm, and can be up to 10^6 times longer. The way the graphene sheet is rolled to yield a CNT is described by two chiral indexes n and m, which characterize both the aspect and the electronic properties of the nanotube (see Figure X). Armchair (n,n) SW-CNTs are metallic, while those either of zigzag (n,0) type or of chiral

(n,m) type are metallic only if (n-m)/3 is an integer; all others are semiconductors with a band gap inversely proportional to their diameter. [32]

The outstanding electronic and mechanical properties of CNTs make them suitable not only in organic electronics (e.g., transistors, [36] solar cells, batteries, hydrogen storage devices [37]), but also for acoustics, textiles and structural applications; even water treatment uses are being explored, not to mention drug delivery and other biologically relevant applications.

As far as photovoltaic cells are concerned, semiconductor SW-CNTs make promising electron acceptors because of their high mobility, large aspect ratio and ultrafast charge transfer with donors such as P3HT. They can be effectively dispersed in semiconducting polymers or π-conjugated semiconductors like porphyrins, overcoming in this way both their well known tendency to form bundles and their low solubility and processability. [38] A self-assembled system of porphyrins and CNTs is presented in the last chapter of this dissertation, Perspectives.

1.6 Computational simulations of organic electronic materials

Over the past decades, the ever-increasing research field of organic electronics has also taken benefit from the development of computational simulation techniques applied to these materials. If, on one hand, Molecular Dynamics simulations of systems made of thousands of atoms have now become accessible, the development of first principles methods able to treat bulk-like systems is now pushing these boundaries even further. Moreover, the so-called multiscale approach which extends the study of a complex system from the electronic structure of its smaller constituents, to the mesoscale of their assembly in 3-D structures, to the calculation of bulk properties using, for instance, stochastic methods, represents nowadays the standard approach in the modeling of complex functional materials for electronics. Simulations can be used either to design new functional organic molecules, and thus predict their electronic and structural properties [39, 40], or to reproduce experimental conditions, providing further insight on them. [41] While a comprehensive review of all the different methodologies and applications of molecular modeling of organic electronic materials is beyond the scope of this sections, some important examples are reported hereafter.

To begin with, the evaluation of molecular energy levels involved in photoexcitation, photoemission, charge transfer or exciton transfer is a fundamental application of electronic structure methods. The latter allow to identify the nature of the excited states involved in such processes, together with the structural factors determining their yield. [42–50] Considering instead processes on a higher time-length

scale, such as self-assembly, molecular deposition, formation of crystalline phases or interfaces, atomistic or coarse-grained molecular dynamics can still yield an accurate description of intermolecular interactions. [51–54] These methods allow to reproduce or predict molecular phenomena where just one or a few kinds of interactions can effectively influence the evolution of the system. Finally, the modeling of the device as a whole can be tackled by replacing molecular detail by a stochastic description [51, 55], or using finite elements methods, [56] reaching thus more realistic time and space domains at the expenses of molecular detail. [57]

In the following chapter, the theoretical foundations of the methods used in this dissertation are briefly discussed.

Bibliography

[1] M. ONeill and S. M. Kelly, *Adv. Mater.*, **2011**, 23, 566-584.

[2] A. Mishra and P. Bäuerle, *Angew. Chem. Int. Ed. Engl.*, **2012**, 51, 2020-2067.

[3] 1 S. Allard, M. Forster, B. Souharce, H. Thiem and U. Scherf, *Angew. Chem. Int. Ed. Engl.*, **2008**, 47, 4070-4098.

[4] M. D. Angione, S. Cotrone, M. Magliulo, A. Mallardi, D. Altamura, C. Giannini, N. Cioffi, L. Sabbatini, E. Fratini, P. Baglioni, G. Scamarcio, G. Palazzo and L. Torsi, *Proc. Natl. Acad. Sci. U. S. A.*, **2012**, 109, 6429-6434.

[5] Y. Wakayama, R. Hayakawa and H.-S. Seo, *Sci. Technol. Adv. Mater.*, **2014**, 15, 024202.

[6] P. Annibale, C. Albonetti, P. Stoliar and F. Biscarini, *J. Phys. Chem. A*, **2007**, 111, 12854-12858.

[7] J. Rivnay, L. H. Jimison, J. E. Northrup, M. F. Toney, R. Noriega, S. Lu, T. J. Marks, A. Facchetti and A. Salleo, *Nat. Mater.*, **2009**, 8, 952-958.

[8] D. Gentili, F. Di Maria, F. Liscio, L. Ferlauto, F. Leonardi, L. Maini, M. Gazzano, S. Milita, G. Barbarella and M. Cavallini, *J. Mater. Chem.*, **2012**, 22, 20852-20856.

[9] T. Mandal and A. Garg, *J. Appl. Phys.*, **2013**, 114, 154517.

[10] G. De Luca, E. Treossi, A. Liscio, J. M. Mativetsky, L. M. Scolaro, V. Palermo and P. Samorì, *J. Mater. Chem.*, **2010**, 20, 2493.

[11] G. Schweicher, N. Paquay, C. Amato, R. Resel, M. Koini, S. Talvy, V. Lemaur, J. Cornil, Y. Geerts and G. Gbabode, *Cryst. Growth Des.*, **2011**, 11, 3663-3672.

[12] G. Giri, E. Verploegen, S. C. B. Mannsfeld, S. Atahan-Evrenk, D. H. Kim, S. Y. Lee, H. A. Becerril, A. Aspuru-Guzik, M. F. Toney and Z. Bao, *Nature*, **2011**, 480, 504-508.

[13] L. Ferlauto, F. Liscio, E. Orgiu, N. Masciocchi, A. Guagliardi, F. Biscarini, P. Samorí and S. Milita, *Adv. Funct. Mater.*, **2014**, 24, 5503-5510.

[14] M. Wright and A. Uddin, *Sol. Energy Mater. Sol. Cells*, **2012**, 107, 87-111.

[15] J. Mei, Y. Diao, A. L. Appleton, L. Fang and Z. Bao, *J. Am. Chem. Soc.*, **2013**, 135, 6724-6746.

[16] M. He, F. Qiu and Z. Lin, *J. Mater. Chem.*, **2011**, 21, 17039.

[17] M. Wright and A. Uddin, *Sol. Energy Mater. Sol. Cells*, **2012**, 107, 87-111.

[18] M. C. Scharber and N. S. Sariciftci, *Prog. Polym. Sci.*, **2013**, 38, 1929-1940.

[19] J. Roncali, P. Leriche and P. Blanchard, *Adv. Mater.*, **2014**, 26, 3821-3838.

[20] K. Cnops, B. P. Rand, D. Cheyns, B. Verreet, M. A. Empl and P. Heremans, *Nat. Commun.*, **2014**, 5, 3406.

[21] B. H. Wunsch, M. Rumi, N. R. Tummala, C. Risko, D.-Y. Kang, K. X. Steirer, J. Gantz, M. Said, N. R. Armstrong, J.-L. Brédas, D. Bucknall and S. R. Marder, *J. Mater. Chem. C*, **2013**, 1, 5250-5260.

[22] C. Poelking, M. Tietze, C. Elschner, S. Olthof, D. Hertel, B. Baumeier, F. Würthner, K. Meerholz, K. Leo and D. Andrienko, *Nat. Mater.*, **2014**, 12, advance online publication.

[23] S. K. Pal, S. Setia, B. S. Avinash and S. Kumar, *Liq. Cryst.*, **2013**, 40, 1769-1816.

[24] E.-K. Fleischmann and R. Zentel, *Angew. Chem. Int. Ed. Engl.*, **2013**, 52, 8810-8827.

[25] J. P. F. Lagerwall and G. Scalia, *Curr. Appl. Phys.*, **2012**, 12, 1387-1412.

[26] Y. Sagara and T. Kato, *Angew. Chem. Int. Ed. Engl.*, **2011**, 50, 9128-9132.

[27] S. Sergeyev, W. Pisula and Y. H. Geerts, *Chem. Soc. Rev.*, **2007**, 36, 1902-1929.

[28] L. Schmidt-Mende, A. Fechtenkötter, K. Müllen, E. Moons, R. H. Friend and J. D. MacKenzie, *Science*, **2001**, 293, 1119-1122.

[29] R. Deschenaux, B. Donnio and D. Guillon, *New J. Chem.*, **2007**, 31, 1064-1073.

[30] Z. Xu and C. Gao, *Nat. Commun.*, **2011**, 2, 571.

19

[31] W. Pisula, M. Zorn, J. Y. Chang, K. Müllen and R. Zentel, *Macromol. Rapid Commun.*, **2009**, 30, 1179-202.

[32] P. C. Dresselhaus, M.S., Dresselhaus, G., Eklund, *Science of Fullerenes and Carbon Nanotubes*, Elsevier, **1996**.

[33] Y. Shen and T. Nakanishi, *Phys. Chem. Chem. Phys.*, **2014**, 16, 7199-7204.

[34] R. B. Ross, C. M. Cardona, D. M. Guldi, S. G. Sankaranarayanan, M. O. Reese, N. Kopidakis, J. Peet, B. Walker, G. C. Bazan, E. Van Keuren, B. C. Holloway and M. Drees, *Nat. Mater.*, **2009**, 8, 208-212.

[35] M. Liedtke, A. Sperlich, H. Kraus, A. Baumann, C. Deibel, M. J. M. Wirix, J. Loos, C. M. Cardona and V. Dyakonov, *J. Am. Chem. Soc.*, **2011**, 133, 9088-9094.

[36] M. Engel, J. P. Small, M. Steiner, M. Freitag, A. a Green, M. C. Hersam and P. Avouris, *ACS Nano*, **2008**, 2, 2445-2452.

[37] D. Jariwala, V. K. Sangwan, L. J. Lauhon, T. J. Marks and M. C. Hersam, *Chem. Soc. Rev.*, **2013**, 42, 2824-2860.

[38] D. A. Britz and A. N. Khlobystov, *Chem. Soc. Rev.*, **2006**, 35, 637-659.

[39] N. M. OBoyle, C. M. Campbell and G. R. Hutchison, *J. Phys. Chem. C*, **2011**, 115, 16200-16210.

[40] A. N. Sokolov, S. Atahan-Evrenk, R. Mondal, H. B. Akkerman, R. S. Sánchez-Carrera, S. Granados-Focil, J. Schrier, S. C. B. Mannsfeld, A. P. Zoombelt, Z. Bao and A. Aspuru-Guzik, *Nat. Commun.*, **2011**, 2, 437.

[41] B. G. Sumpter and V. Meunier, *J. Polym. Sci. Part B Polym. Phys.*, **2012**, 50, 1071-1089.

[42] F. May, M. Al-Helwi, B. Baumeier, W. Kowalsky, E. Fuchs, C. Lennartz and D. Andrienko, J. Am. Chem. Soc., 2012, 134, 13818-13822.

[43] D. Beljonne, J. Cornil, L. Muccioli, C. Zannoni, J.-L. Brédas and F. Castet, *Chem. Mater.*, **2011**, 23, 591-609.

[44] J. L. Brédas, J. P. Calbert, D. a da Silva Filho and J. Cornil, *Proc. Natl. Acad. Sci. U. S. A.*, **2002**, 99, 5804-5809.

[45] D. L. Cheung and A. Troisi, *Phys. Chem. Chem. Phys.*, **2008**, 10, 5941-5952.

[46] D. L. Cheung and A. Troisi, *J. Phys. Chem. C*, **2010**, 114, 20479-20488.

[47] S. R. Yost, L.-P. Wang and T. Van Voorhis, *J. Phys. Chem. C*, **2011**, 115, 14431-14436.

[48] S. Braun, W. R. Salaneck and M. Fahlman, *Adv. Mater.*, **2009**, 21, 1450-1472.

[49] S. Osella, A. Narita, M. G. Schwab, Y. Hernandez, X. Feng, K. Müllen and D. Beljonne, *ACS Nano*, **2012**, 6, 5539-5548.

[50] A. E. Jailaubekov, A. P. Willard, J. R. Tritsch, W.-L. Chan, N. Sai, R. Gearba, L. G. Kaake, K. J. Williams, K. Leung, P. J. Rossky and X.-Y. Zhu, *Nat. Mater.*, **2013**, 12, 66-73.

[51] P. Clancy, *Chem. Mater.*, **2011**, 23, 522-543.

[52] E. Yıldırım, M. Yurtsever, B. Kenarlı and a. L. Demirel, *Macromol. Theory Simulations*, **2011**, 20, 340-349.

[53] J. Anwar and D. Zahn, *Angew. Chem. Int. Ed. Engl.*, **2011**, 50, 1996-2013.

[54] D. Beljonne and J. Cornil, Eds., *Multiscale Modelling of Organic and Hybrid Photovoltaics*, Springer Berlin Heidelberg, Berlin, Heidelberg, **2014**, vol. 352.

[55] A. G. Gagorik and R. Hutchison, *J. Phys. Chem. C*, **2012**, 116, 21232-21239.

[56] M. Mesta, M. Carvelli, R. J. de Vries, H. van Eersel, J. J. M. van der Holst, M. Schober, M. Furno, B. Lüssem, K. Leo, P. Loebl, R. Coehoorn and P. A. Bobbert, *Nat. Mater.*, **2013**, 12, 652-658.

[57] J. Nelson, J. J. Kwiatkowski, J. Kirkpatrick and J. M. Frost, *Acc. Chem. Res.*, **2009**, 42, 1768-1778.

Chapter 2

Molecular modelling

In this chapter, a brief introduction of the theory and methods used in this dissertation is presented. The first sections are devoted to different electronic structure methods; then, atomistic molecular mechanics (MM) and dynamics (MD) calculations are approached; finally, the fundamentals of stochastic Monte Carlo algorithms are explained.

Among the many semi-empirical methods, where only valence electrons are considered, ZINDO remains perhaps the most important and used for the calculation of electronic spectra. Being parametrized for a large number of atoms, included transition metals, ZINDO is a very effective and low-cost method.

Density Functional theory (DFT) and its time-dependent derivation (TD-DFT), which provide an accurate and inexpensive description of electronic structure, are used to obtain information on both the ground state and the excited state of a system. The theoretical foundation of DFT lies on the assumption that all information about the state of a molecule can be obtained by studying is electronic density. Despite being exact in principle, the goodness of DFT relies on the different approximations made to calculate the correlation energy term, that accounts for the electron-electron repulsion. The main functionals used in this work, CAM-B3LYP and M06-2X, are discussed. They allow to compensate the self-interaction error when dealing with delocalized π-systems and charge-transfer excitations.

Molecular Mechanics, on the other side, is another atomistic method which describes molecules as a set of hard spheres held together by classical mechanics forces. Electrons are ignored and energy depends only on nuclear positions. The sum of all energy terms describing the interactions between the atoms is called Force Field. Molecular Dynamics simulations allow to describe the evolution of a system in time: starting from randomly assigned velocities, the forces acting on each atom are evaluated and used to calculate the corresponding acceleration.

The equations of motion are integrated by dividing the simulation time in short intervals, and for each a new set of velocities and atomic position is obtained. The collection of atomic positions over time represents the trajectory of the system. Finally, moving forward in the space domain, stochastic numerical methods allow to treat systems having realistic dimensions as a catalog of Markovian events. The basic Monte Carlo (MC) algorithm starts by generating a random distribution of the possible states of the system; its evolution depends on the probabilities of the different events according to the so-called Metropolis criterion. Among the wide range of its applications, MC is also used to simulate charge or exciton transport in bulk materials, where different molecules are represented as a collection of jump probabilities.

2.1   Semiempirical SCF-MO theory

When computational chemistry was still a young science, and computing power was infinitely smaller, even carrying out Hartree Fock (HF) calculations for small systems was no trivial task. A certain number of chemists started to develop less refined methods, that would make affordable the modeling of large system without significant accuracy losses. There are two different kinds of approximations in order to lighten HF theory and speed up calculations. The first way is the indirect calculation of two-electron integrals, which require most of the computational effort, and their numerical approximation. This simplification can be justified in the case of two electrons on two different atoms which are such far away from each other that their interaction is negligible. A second way, that allows to obtain a "chemically virtuous" approximation, [1] is to introduce a term accounting for electronic correlation. Then, it is possible to obtain even better results with a coarser method. The simplifications invoked above usually require the use of parameters chosen so as to better fit experimental data: from here the term semiempirical. Semiempirical methods can be considered as derived from empirical methods like the Hückel model (that considers only π valence electrons), [2] and the extended Hückel model (for all valence electrons). [3] INDO and NDDO were first created in the 1960's and 70's but are still in use and under development. The Intermediate Neglect of Differential Overlap (INDO) method [4] is a modification of the CNDO (Complete Neglect of Differential Overlap). [5] Originally, only s and p valence orbitals were included. In CNDO, two-electrons integrals are defined as:

$$(\mu\nu|\lambda\sigma) = \delta_{\mu\nu}\delta_{\lambda\sigma}(\mu\mu|\lambda\lambda) \tag{2.1}$$

The only integrals that do not disappear are the ones that involve identical orbitals on different atoms:

$$(\mu\mu|\lambda\lambda) = \gamma_{AB} \tag{2.2}$$

A and B correspond to the atoms where μ and λ are. γ_{AB} is commonly treated as a parameter. This simplification is what gives the name to the model and consistently lightens calculations, because the remaining integrals can be computed algebrically and not analitically.

The major difference between these two methods is that while CNDO uses ZDO (Zero Differential Overlap) on all two-electrons integrals, INDO introduces different values for two-electron integral with electrons belonging to different orbitals on the same atom (one-center two-electron). This refinement results in a more accurate geometry prediction and in the possibility of modeling electronic transitions and reproducing UV-Vis spectroscopy. Later on, Ridley and Zerner [6] carried on a parametrization of INDO, called INDO/S or ZINDO model from Zerner's software, [7] especially developed for spectroscopic problems. This model has been extended to include also elements with d and f orbitals.
The Neglect of Diatomic Differential Overlap (NDDO) method [8] improves the INDO by adding more flexibility in the evaluation of two-center two-electron integrals. Both in INDO and CNDO, all of them are substituted by a single parameter, γ_{AB}. Instead, in NDDO the integrals $(\mu\nu|\lambda\sigma)$ where μ and ν are on the same atom do not disappear, and the same is true for λ and σ. The number of possible integrals to evaluate increases a lot going from INDO to NDDO, because every combination of s- and p-orbitals (and, in modern models, also d-orbitals) gives rise to a different integral, and thus to a different parameters. The majority of modern semi-empirical methods, such as AM or PM series, [9, 10] is based on NDDO.

2.2   Density Functional Theory

The Density Functional Theory (DFT) is of the most important electronic structure methods. It is based on the model developed in 1927 by Thomas and Fermi, who for the first time thought about studying multi-electronic systems starting from their electronic density instead of the wave function Ψ of the Schrödinger equation. [11–13] In 1964, Hohenberg and Kohn published the Existence Theorem and the Variational theorem, that are fundamental for the development of DFT. The first one states that all the information about the ground state of a molecule can be uniquely determined by studying the electronic density $\rho_0(x, y, z)$, which only depends on the position. As a consequence, the electronic energy is a function of $\rho_0(x, y, z)$, or more precisely a functional: $E_0 = E_0[\rho_0(x, y, z)]$. The second one,

which has an equivalent in Hartree-Fock (HF) theory, identifies an energy functional for the system and demonstrates that the correct ground state density minimizes that functional.

The electronic energy of a multi-electronic system can be represented as:

$$E[\rho(\vec{r})] = T_{ni}[\rho(\vec{r})] + V_{Ne}[\rho(\vec{r})] + V_{ee}[\rho(\vec{r})] + E_{xc} \tag{2.3}$$

where the first three terms correspond to the kinetic energy for non-interacting electrons, the nuclear-electron interaction, and the interelectronic repulsion, respectively. E_{xc}, defined as the exchange and correlation energy, is a term that accounts for two different contributions: the first is a correction to the kinetic energy for the interacting electrons, and the second represents a correction to the electron-electron repulsion. The former, known as the exchange term, is known, even if it is difficult to calculate exactly; the correlation term, instead, is not known in its exact form. DFT is, in principle, exact. What determined the the different approximations made to estimate the E_{xc} term determine the effective goodness of the method. [14]

How can we calculate all the system properties from the density? The Kohn Sham (KS) method is a self consistent field (SCF) procedure similar to the HF method; we start from the equation

$$h_i^{KS}\chi_i = \varepsilon_i\chi_i \tag{2.4}$$

where χ_i is a set of orthonormal KS orbitals related to the density by $\rho = \sum_{i=1}^{n} \mid \chi_i^2 \mid$. The KS monoelectronic operator h_i^{KS} can be written as

$$h_i^{KS} = -\frac{1}{2}\nabla_i^2 - \sum_{k}^{nuclei} \frac{Z_k}{\mid \vec{r_i} - \vec{r'} \mid} + \int \frac{\rho(\vec{r'})}{\mid \vec{r_i} - \vec{r'} \mid}d\vec{r'} + V_{xc} \tag{2.5}$$

In the same way as in the HF-SCF theory, the energy and the Molecular Orbitals (MO) coefficients are calculated starting from an initial guess for the density ρ. The MO coefficients are then used to obtain a new density. The procedure is carried on until the new values do not differ significantly from the old ones, that is until the value of a set root mean square gradient is reached.

In order to perform DFT calculations it is necessary to search for an expression for the correlation energy. The first approximation to be developed was the Local Density Approximation (LDA), which was then extended to the Local Spin Density Approximation (LSDA) for open-shell systems. The value of ϵ_{XC} in a certain point depends only on the value of the density at that point. The only requirement ρ has to satisfy is to be unambiguous. This very broad definition is actually referred to those functionals derived from the uniform electron gas model, where the density has the same value all over space. These local models are limited, but still used for sizeable systems like proteins.

Gradient corrected functionals represent the next step in the development of correlation functionals; the Generalized Gradient Approximation (GGA) is generally applied as an additional term to the LSDA functional:

$$\varepsilon_{xc}^{GGA}[\rho(\vec{r})] = \varepsilon_{xc}^{LSDA} + \Delta\varepsilon_{xc}\frac{\mid \nabla\rho(\vec{r}) \mid}{\rho^{4/3}(\vec{r})} \tag{2.6}$$

Exchange and correlation parts are often developed as two separate functionals; they can be chosen independently from each other and have to be reported indicating the respective acronyms.

Some of the most popular GGA functionals, like Becke's exchange functional B, [15] have incorporated empirical parameters that account for the exchange energies of some atoms; others, like the functional of Perdew, Burke and Enzerhof (PBE), [16] have none. The most used exchange functional was developed by Lee, Yang and Parr (LYP); [17] unlike others, it does not incorporate LSDA correlation.

Meta-GGA functional expand the GGA approach by taking into consideration also the second derivative of the density. This improvement in performance is affected by the difficulty of evaluating the Laplacian of the density. As far as calculation costs are concerned, GGA and MGGA are substantially the same. These functionals are defined as "pure" to distinguish them from hybrid functionals. The latter contain also a term derived from HF exchange energy:

$$E_{xc} = aE_x^{HF} + (1-a)E_{xc}^{DFT} \tag{2.7}$$

where a is a variable. Hybrid functionals are parametrized for certain elements and classes of molecules, so they can fail for some systems. Nontheless, they generally show the best performances over GGA and MGGA functionals.

Overcoming self-interaction error: M06 and CAM-B3LYP

One of the most known issue of DFT methods is represented by the self-interaction energy error (SIE). The classical electrostatic repulsion term

$$J[\rho] = \iint \frac{\rho(\bar{r}_i\rho(\bar{r}_j)}{r_{ij}}d\bar{r}_id\bar{r}_j \tag{2.8}$$

does not completely vanish for a one-electron system because the density interacts with itself. Since $E_{xc}[\rho]$ is never exact and independent of $J[\rho]$, there is generally a residual energy due to self-interaction effects. As a consequence, DFT methods tend to reproduce an over-delocalized electron density. Because of this drawback, the use

of corrected DFT methods is fundamental in dealing with charge-transfer states, Rydberg excitations or systems having weakly bound electrons. In recent years, several functionals have been formulated to overcome SIE. A popular example is given by the long-range interaction corrected CAM-B3LYP [18] functional, which adopts the Coulomb attenuating method. The key step is the partitioning of E_x into the sum of long-range (LR) and short-range (SR) contributions:

$$E_x = E_X^{LR} + E_X^{SR} \tag{2.9}$$

While the long-range part is evaluated through the exact orbital expression, the short-range part is expressed in terms of the DFT one-particle density matrix. Other functionals developed against SIE errors belong to the M05 and M06 families [19]. They implicitly account for medium-range (defined by Truhlar and Zhao as 5 Åor less [20]) electron correlation because of the way they are parametrized, and this is sufficient to describe the dispersion interactions within many complexes. M06-2X, a global hybrid functional with 54% Hartree Fock exchange, is the functional giving the best performances of the family for non-bonded interactions. To conclude, while CAM-B3LYP is suitable for charge-transfer or Rydberg states, M06-2X is particularly indicated when dealing with systems characterized by important non-covalent interactions. Both functionals have been used in the work presented in this dissertation.

2.3   Time-Dependent DFT and electronic excited states

Although DFT was initially developed as a ground-state theory, it is also possible to apply it to electronic excited states. In 1984, a theoretical enounciation of Time-Dependent DFT was published as the time dependent version of the Hohenberg-Kohn theorem by Runge and Gross. [21] The most popular theory is called Linear Response DFT (LR-DFT): it is based on the time-dependent perturbation theory and the perturbation is represented as a weak oscillating electric field. The change in the density induced by the perturbation is found to be proportional to the difference in energy between the ground state E_0 and the excited states E_J. If this operation is repeated while varying the ground-state geometry, one can optimize the excited state geometry by minimizing the excitation energy.
As far as accuracy is concerned, this theory works quite well for single excitations, and gives better results than Configuration Interaction Singles (CIS) [22]. Some known limitations involve charge-transfer excitations, long conjugated chains, and

high energy excited states, for which TD-DFT performs poorly. Altogether, this method is more flexible, less demanding and more suitable for large systems than other very accurate post-HF models like Complete Active Space SCF (CASSCF) [23].

Together with the excitation energy, oscillator strengths f_{ij} can be easily obtained:

$$f_{ij} = \frac{2}{3\hbar^2}(E_2 - E_1) \sum_{\psi_j} \sum_{\alpha=x,y,z} |\langle \psi_i | R_\alpha | \psi_j \rangle|^2 = 1.44 \times 10^{-19} \int \epsilon(\nu) d\nu \qquad (2.10)$$

Oscillator strengths depend on the transition probability and therefore can be used to predict the aspect of absorption spectra. Using gaussian functions centered around the probability peaks, theoretical spectra similar to experimental ones can be obtained and compared. Of course, a certain error is expected because UV-Vis spectra are measured in condensed phase; the here used Quantum Mechanical (QM) calculations, instead, are done considering an isolated molecule in gaseous phase, at 0 K, where only Zero Point Vibrational Energy (ZPVE) contribution remains. Hence, results from TD-DFT can be shifted in respect to experimental data. This shift - if we consider the theoretical prediction to be exact - is due to the effect of solvent, known as solvatochromism. It is not predictable whether the solvent will cause a blue or a red shift.

As a final remark, the data obtained with TD-DFT can be considered reliable, if the functional is chosen carefully and within the known limitations (vide supra). The spectra, even if shifted, are qualitatively accurate because the solvent has usually little effect on the oscillator strength.

2.4   Relativistic effects and Pseudopotentials

In atoms with high nuclear charge Z, the effective speed of inner shell electrons tends to be closer to the speed of light c. The relativistic mass of the electron, m_{rel}, is a function of the electron speed; when v_e tends to c, m_{rel} tends to infinity. The change in the electron mass affects Bohr radius due to the direct proportionality between them. This results in a contraction of the orbitals having low principal quantum numbers, like s and p shells; on the other side, d and f electrons are better screened from the nucleus and thus can expand further.

When dealing with heavy elements, it is important to take into account relativistic effects; this is done by performing relativistic HF calculations, using the so-called Dirac-Fock equations. Since this approach is very demanding, it is preferable to perform one all-electrons Dirac-Fock calculation for each heavy atom separately and then use the results to generate a Relativistic Effective Core Potential (RECP). The core Atomic Orbitals are assumed to remain the same going from isolated atom

to molecules, and the valence electrons are treated explicitly non-relativistically. RECPs are available for most of the elements at https://bse.pnl.gov/bse/portal.

Functionals used in this thesis

- PBE0 (hybrid): Adamo's [24] modification of the parameter-free exchange and correlation functional developed by Perdew, Burke and Ernzerhof in 1996 [16].

- HSE06 (hybrid): Heyd-Scuseria-Ernzerhof functional with a screened Coulomb potential developed in 2004 [25].

- B3LYP (hybrid): exchange and correlation functional developed by Becke (three parameters) [15]; correlation functional of Lee, Yang and Parr in 1993 [17].

- CAM-B3LYP (hybrid): long range corrected version of B3LYP developed by Handy in 2004 [18].

- M06 and M06HF(hybrid): 2008 standalone functionals of Truhlar and Zhao [19].

2.5   Molecular Mechanics simulations

If the molecular systems become too large or the quantum mechanical calculation are too time-consuming, Molecular Mechanics (MM) simulations represent a feasible and accurate alternative. They rely mainly on Born Oppenheimer approximation, thus ignoring electronic motion and treating only nuclear motion from a classical point of view. The Hamiltonian of a system containing N particles can be written as a sum of kinetic and potential energy:

$$H(q^N, p^N) = K(p^N) + V(q^N) \tag{2.11}$$

the kinetic energy K is defined as a function of particle masses and momenta:

$$K = \sum_{i=0}^{N} \sum_{\alpha} \frac{p_{i\alpha}^2}{2m_i} \tag{2.12}$$

The potential energy V is defined in terms of different intra- and inter-molecular forces, such as bond stretching and rotation, angle bending, and non-bonded

interactions. The following expression contains all these terms and represents a standard, simple Force Field (FF): [26]

$$V(q^N) = \sum_{bonds} \frac{k_i}{2}(l_i - l_{i,0})^2 + \sum_{angles} \frac{k_i}{2}(\theta_i - \theta_{i,0})^2$$

$$+ \sum_{torsions} \frac{V_N}{2}[1 + cos(n\omega - \lambda)] \qquad (2.13)$$

$$+ \sum_{i=1}^{N} \sum_{j=i+1}^{N} \left\{ 4\varepsilon_{ij} \left[\frac{\sigma_{ij}}{r_{ij}}^{12} - \frac{\sigma_{ij}}{r_{ij}}^{6} \right] + \frac{Q_i Q_j}{4\pi\varepsilon_0 r_{ij}} \right\}$$

Atoms are treated as rigid spheres and bonds as springs. Their degrees of freedom are represented by 'penalty' functions, where energy rises if bonds or angles deviate from their equilibrium values. In more detail, the first term represents a harmonic potential for bond deformation, where l_i denotes the bond length, $l_{i,0}$ its equilibrium value, and k_i the force constant. The same applies for the bending potential, and it bending term θ_i. The third term represents a torsional potential, meaning the rotation around a bond: V_n influences the rotational barrier, n controls the periodicity and λ the phase.

Non-bonded interactions are classified as Van der Waals attraction, steric repulsion, and electrostatic attraction/repulsion. They are usually calculated between all atom pairs belonging to different molecules or separated by at least three bonds. The former is described using a Lennard-Jones potential, with parameters ε_{ij} determining the depth of the potential well and σ_{ij} controlling the interatomic distance for a given atom pair. Electrostatic interactions are modelled using a Coulomb potential, where Q are the atomic charges and r_{ij} the distances between atom pairs.
These terms constitute the essential building blocks of a FF, but more complicated ones exist having a larger number of terms.

Inter-atomic interactions are thus represented by a series of parameters, which depend on the kind of atoms involved, and on their classification within the FF, the so-called "atom type", defining the atomic behaviour in a determined chemical environment. E.g., a sp^3 carbon must be differentiated from a sp^2 carbon, which in turn is different from a carbon atom inside an aromatic π system. Common force fields differ from each other for the systems they are targeted to reproduce; some are more suitable for biological systems, other for organic aromatic molecules, others for organic-inorganic systems. To sum up, a FF can be defined as a collection

of atom type definitions.

Once the desired FF is chosen, the most challenging and time-consuming part of a MM calculation is the choice of the proper set of parameters to correctly describe a given set of molecules. That often involves a re-parameterization process, aimed at reproducing both their ab initio potentials and experimental properties.

2.6 MM3 Force Field

MM3 [27] is one of the most suitable force fields for the description of organic molecules, especially conjugated systems since it features corrections to torsions and bond lengths of the atoms involved in the π system, that are evaluated with a self iterating procedure. [28] In general, bond stretching terms V_{str} and angle bending terms V_{bend} are evaluated through displacements of the bond lengths and angles from their reference values $_0$ and ϑ_0:

$$V_{str} = 71.94 k_s (l - l_0)^2 1 - 2.25(l - l_0) + \frac{7}{12} 2.55(l - l_0)^2]$$

$$V_{bend} = 0.021914 k_\theta (\theta - \theta_0)^2 1 - 0.014(\theta - \theta_0) + 5.6 \times 10^{-5} (\theta - \theta_0)^2 \qquad (2.14)$$

$$- 7.0 \times 10^{-7} (\theta - \theta_0)^3 + 9.0 \times 10^{-10} (\theta - \theta_0)^4]$$

Torsional contributions between non bonded atoms in 1-4 relative position, V_{tors}, are expanded in a series of cosine functions of the dihedral angle, ω:

$$V_{tors} = \frac{V_1}{2}(1 + cos\omega) + \frac{V_2}{2}(1 - cos2\omega)\frac{V_3}{2}(1 + cos3\omega) \qquad (2.15)$$

Also energy cross-terms, such as the coupling stretching-bending, V_{s-b}, stretching-torsion, V_{s-t}, and between different angle bending, V_{b-b}, are considered:

$$V_{s-b} = 2.51118 k_{s\theta}[(l - l_0) + (l' - l'_0)](\theta - \theta_0)$$

$$V_{s-t} = 11.915 \frac{k_{s\omega}}{2}(l - l_0)(1 + cos3\omega) \qquad (2.16)$$

$$V_{b-b} = 0.021914 k_{\theta\theta'}(\theta - \theta_0)(\theta' - \theta'_0)$$

Van der Waals energy terms between non-bonded atoms are described by a function that takes into account the attractive and repulsive terms through the inverse of

the sixth power and an exponential function of the interatomic distance:

$$V_{VdW} = \varepsilon \left\{ -2.25 \left(\frac{r_{VdW}}{r} \right)^6 + 1.84 \times 10^5 e^{-12.0(r/r_{VdW})} \right\} \tag{2.17}$$

In the original implementation of the FF, electrostatic interactions are calculated by means of dipoles, using fixed charges for each atom. In some of the presented studies, a different approach was using atomic charges derived from the Charge Equilibration method, [29] as will be explained in the following section.

2.7 Atomic charges: the Charge Equilibration method

Within the framework of MM simulations, there are several ways of accounting for the polarizability of molecules. Ideally, the assignment of atomic charges for large systems should be done without recurring first to ab initio electronic structure calculations, with a reliable and computationally feasible method. This discussion will focus on a model that does not require any additional information other than molecular geometry: the Charge Equilibration (QEq) method developed by Rappé and Goddard [29]. This method is employed in the Universal Force Field (UFF) [30] and, in principle, can be used to calculate charges for any atom in the periodic table.

To begin with, we define the atomic energy as a function of charge using a truncated series expansion:

$$v_A(q) = v_{A0} + q_A \left(\frac{\delta v}{\delta q} \right)_{A0} + \frac{1}{2} q_A^2 \left(\frac{\delta^2 v}{\delta q^2} \right)_{A0} \tag{2.18}$$

For the neutral, positively charged and negatively charged species, the previous expression becomes:

$$v_A(0) = v_{A0}$$

$$v_A(+1) = v_{A0} + q_A \left(\frac{\delta v}{\delta q} \right)_{A0} + \frac{1}{2} q_A^2 \left(\frac{\delta^2 v}{\delta q^2} \right)_{A0} \tag{2.19}$$

$$v_A(-1) = v_{A0} - q_A \left(\frac{\delta v}{\delta q} \right)_{A0} + \frac{1}{2} q_A^2 \left(\frac{\delta^2 v}{\delta q^2} \right)_{A0}$$

The energy of the positively charged species is equal to the ionization potential (IP), while that of the negatively charged species is the electron affinity (EA). The combination of both expressions results in:

$$\left(\frac{\delta v}{\delta q}\right)_{A0} = \frac{1}{2}(IP - EA) = \chi_A^0$$

$$\left(\frac{\delta^2 v}{\delta q^2}\right)_{A0} = IP - EA \tag{2.20}$$

Where χ_A is the electronegativity.

The difference (IP - EA) can be interpreted as the Coulomb repulsion between two electrons in the same orbital, defines by Rappé and Goddard as an "idempotential", $J_{AA}{}^0$. This yields:

$$v_A(q) = v_{A0} + \chi_A^0 q_A + \frac{1}{2} J_{AA}^0 q_A^2 \tag{2.21}$$

The total electrostatic energy of a system is thus:

$$v(q_1, ..q_N) = \sum_{i=1}^{N} (v_{A0} + \chi_A^0 q_A + \frac{1}{2} q_A^2 J_{AA}^0) + \sum_{A=1}^{N} \sum_{B=A+1}^{N} q_A q_B J_{AB} \tag{2.22}$$

Since $J_{AA}(R) \to J_{AA}^0$ as $R \to 0$, we can formulate a more compact expression:

$$v(q_1, ..q_N) = \sum_{i=1}^{N} (v_{A0} + \chi_A^0 q_A) + \sum_{A=1}^{N} \sum_{B=1}^{N} q_A q_B J_{AB} \tag{2.23}$$

The last term is a Coulomb potential between charges q_A and q_B, that scales as $1/r$. This works well for distant atoms, but when two atoms are so close that their densities overlap, J_{AB} does not give the correct asymptotical behaviour. To overcome this problem, a shielding factor has to be introduced. This takes the form of a Coulomb integral between atomic densities, represented as Slater-type orbitals (STO):

$$\phi_{n\zeta} = N_n r^{n-1} e^{-\zeta r}$$

From the previous equation we can derive the appropriate Slater coefficient ζ for an atom A, simply by expressing the average atomic radius as a function of ζ.

$$R_A = r_{avg} = (2n + 1)/2\zeta_A$$

$$\zeta_A = \lambda(2n + 1)/2R_A \tag{2.24}$$

33

where λ is an adjustable parameter.

In order to calculate the actual atomic charges, we first take the derivative of the energy as a function of q_A, that gives us the atomic-scale chemical potential χ_A:

$$\frac{\delta V(q_{1,..q_N})}{\delta q_A} = \chi_A = \chi_A^0 + \sum_{A=1}^{N} q_B J_{AB} = \chi_A^0 + J_{AA}^0 q_A + \sum_{B=1,B\neq A}^{N} q_B J_{AB} \qquad (2.25)$$

where χ_A is a function of the charges on all atoms. To solve this expression, we impose two conditions: i) that all atomic chemical potentials be equal at equilibrium, and ii) that the total charge has to be equal to the summation over atomic charges.

$$\chi_1 = \chi_2 = ... = \chi_N$$

$$Q_{tot} = \sum_{i=1}^{N} Q_i \qquad (2.26)$$

As a consequence, we end up with a set of equations to be solved simultaneously, that can be represented in matrix form as:

$$\mathbf{CD} = -\mathbf{D} \qquad (2.27)$$

where

$$D_1 = -Q_{tot} \quad D_i = \chi_i^0 - \chi_1^0 \qquad \text{for} \quad i \geqslant 2$$

$$C_{1i} = Q_i \qquad C_{ij} = J_{ij} - J_{1j} \qquad \text{for} \quad i \geqslant 2 \qquad (2.28)$$

Finally, it must be noted that for each atomic species only certain values for atomic charge are allowed; this in turn limits the possible values of χ and J. Outside these values, $V(Q) \to \infty$.

The solution of the above equations yields, in principle, the correct QEq charges for all elements of the periodic table. Hydrogen, though, represents a notable exception: the Mulliken definition of $\chi_H = (IP - EA)$ yields the nonrealistic value of 7.17 eV, higher than that of carbon or nitrogen. The reason for this strong deviation is that the hydrogen atomic orbital involved in a bond cannot expand as much as it could in a free H^- ion. Therefore, the effective electronegativity of hydrogen is much smaller and, in order to account for that in the QEq scheme, an effective charge parameter must be introduced:

$$\zeta_H = \zeta_H^0 + Q_H \qquad (2.29)$$

In this way also the idempotential becomes charge-dependent:

$$J_{HH}(Q_H) = J_{HH}^0 \left(1 + \frac{Q_H}{\zeta_H}\right) \qquad (2.30)$$

To solve equation 2.27, we start with a trial value for Q_H and then iteratively solve until self-consistency is reached for all hydrogens.

2.8   Molecular Dynamics simulations

Molecular dynamics is a deterministic, time-dependent computational method. Given the position of an atom $\bar{q}$ at time t, its linear momentum $\bar{p}$ and the force $\bar{F}$ applied on it, it is always possible to determine $(\bar{q}, \bar{p}, \bar{F})(t + \delta t)$. Therefore, by the integration of Newton's equations of motion, a MD simulation yields the trajectory of the atoms of the system. The results of a MD simulation can also be used to determine macroscopic thermodynamic properties of the system on the basis of the ergodic hypothesis, stating that the statistical time averages are equal to ensemble averages of the system.

Molecular Dynamics can be performed in different ensemble systems, the most common being the micro canonical (NVE), canonical (NVT) and isothermal-isobaric (NPT) ensembles. Whatever the choice of the ensemble, in order to correctly explore the corresponding $(\bar{q}, \bar{p})$ phase space, a suitable method to integrate the equations of motion has to be chosen. Common algorithms make use of finite difference methods; from a practical point of view, this means dividing the simulation time in small, discrete intervals, which approximate the continuous evolution of the real system. Velocities and positions are expanded in a Taylor series, where δt represents the time-step:

$$r(t + \delta t) = r(t) + v(t)\delta t + \frac{1}{2}a(t)\delta t^2 + ...$$

$$v(t + \delta t) = v(t) + a(t)\delta t + \frac{1}{2}b(t)\delta t^2 + ... \qquad (2.31)$$

A popular and not computationally demanding algorithm of this sort was developed by Verlet [31]; a number of alternatives based on it were implemented, the most famous being the velocity Verlet and the Beeman algorithms. [32, 33]

At this point, it should be clear that the choice of the integration step largely determines the successful outcome of a MD simulation. For instance, the time-step must be small enough to avoid discretization errors (that is, smaller than the inverse of the fastest vibrational frequency in the system). Thus, typical time-steps are in

the order of 1 fs, although this limit can be overcome by introducing constraints that eliminate the vibrational modes of the fastest atoms (mostly hydrogens), or by eliminating hydrogen atoms (at least the non polar ones) altogether. In the latter case, we talk about United-Atom Force Fields (UAFF), where the parameters of the remaining atoms (usually carbon atoms) are rescaled accordingly to provide a good agreement with experimental data. [34–36]

A MD simulation is generally carried out through the following steps:

- **Selection of the initial configuration of the system.** The starting geometry of the simulation can either be taken from a crystallographic structure, if the studied system is in a solid. More frequently, dynamics are performed in the liquid phase; when the solvent is explicitly modeled, it is necessary to reproduce the experimental density of the system.

- **Equilibration.** In this phase, the system is allowed to relax to its equilibrium condition; its length depends on the process being modelled. In general, the equilibration is assessed by monitoring the oscillation of different thermodynamic or structural properties in time, and it can be considered complete when those are finally stabilized.

- **Production.** This is the "real" part of the simulation from where the system evolution in time can be followed, and all the relevant system properties can be calculated, either on-the-fly or during the analysis step.

- **Analysis.** The trajectory obtained during the production phase is finally examined, and possibly used to derive some time-dependent characteristics of the system.

The initial task of a MD simulation is to assign an initial velocity to each particle by randomly picking from a Maxwell-Boltzmann distribution corresponding to the temperature of the simulation:

$$p(v_{ix}) = \left(\frac{m_i}{2\pi k_B T} \right) \exp \left[-\frac{1}{2} \frac{m_i v_{ix}^2}{k_B T} \right] \tag{2.32}$$

where $p(v_{ix})$ represent the probability, for the i-th atom, of having a velocity v_{ix} along x at temperature T. The set of initial velocities has to satisfy the condition that the total linear momentum at time $t = 0$ has to be zero. During the equilibration phase, the velocities will then readjust among the different degrees of freedom of the system; they will be also properly rescaled in order to keep the temperature constant.

Periodic Boundary Conditions

An important requirement is that the modelled system should be representative of its macroscopic counterpart. In order to simulate, e.g., a molecular crystal, surface effects should be ideally suppressed and bulk interactions must prevail. This is achieved through Periodic Boundary Conditions (PBC), which create replicas of the simulation box in three dimensions by translating the original coordinates. The number of particles in the central box is fixed: for each particle leaving the box during the simulation, an image particle enters from the opposite side in order to replace it. Interactions between the original system and its images are managed through suitable cut-offs. The cubic cell is the simplest periodic system to reproduce, but the shape of the periodic cell depends on the requirements of a specific simulation.
When using PBC to model surfaces, e.g. a monolayer on a substrate, only interactions along the directions defined from the surface plane are present. This is achieved by defining large vertical periodicity so that, using a proper cut-off, no energy contribution arise from the interactions between the neighboring simulation boxes normal to the surface plane.

2.9   Monte Carlo algorithms

Monte Carlo methods are a broad family of stochastic, time-independent algorithms widely used in different fields, ranging from physics to economics, born after the first formulation by Metropolis and Ulam [37, 38] published in 1949. In its modern formulation, developed in the 1960s, [39] it is commonly referred to as Kinetic Monte Carlo (KMC). The method answers to the problem of predicting the most probable outcome of an experiment by simply repeating the same experiment many times and counting the most recurring outcome. Unlike MD, that allow to simulate the evolution in time and space of a system, KMC works by sampling a number of randomly generated replicas of the same system. The significant advantage of the latter is the possibility of tackling problems having a time-scale that goes well beyond microseconds, thus almost impossible to achieve by MD. [40] In addition to this, for the ergodic hypothesis, these two approaches must converge to yield the same information. [41]
A general Monte Carlo algorithm normally involves: i) building of an initial configuration, ii) generation of a "random move", iii) evaluation against a rule, iv)

acceptance or rejection of the move according to the Metropolis criterion:

$$B \sim \begin{cases} e^{-\Delta E/kT} & \text{if} \quad \Delta E > 0 \\ 1 & \text{if} \quad \Delta E \leq 0 \end{cases} \qquad (2.33)$$

Where B is the Boltzmann distribution, and ΔE refers to the energy difference between the two configurations (before and after the random move).

The known limitation of MC is that the probability (or kinetic constant) of every possible move has to be given as an input to the algorithm, thus requiring a prior evaluation of the involved rates. This can be done either by using experimentally available data, or through quantum-mechanical calculations, as in the case of charge or exciton transfer processes.

In this dissertation, a Monte Carlo algorithm is built in order to determine the exciton dynamics of a molecular aggregate. The detailed procedure is discussed in Chapter 4.

2.10   Software

- ZINDO calculations were performed using the ZINDO-MN2011 [7] code, available free of charge.

- DFT and TD-DFT calculations were performed using the commercially available Gaussian09 [42] software suite.

- The MD and MM simulations were performed with the Tinker molecular modeling packages [43] (versions 4 and 6).

- Visual software packages were used to prepare molecular structure input files and pictures: Molden [44] and VMD. [45]

- Graphs and plots were prepared with Gnuplot [46] and Gabedit [47].

- The Monte Carlo exciton dynamics simulations, discussed in Chapter 5, were performed using a home-made Fortran code.

Bibliography

[1] C. J. Cramer, *Essentials of Computational Chemistry*, Wiley, **2005**.

[2] E. Hückel, *Zeitschrift für Physik*, **1931**, 70, 204; **1931**, 72, 310; **1932**, 76, 628; **1933**, 83, 632.

[3] R. Hoffmann, *J. Chem. Phys.*, **1963**, 39 (6), 1397-1412.

[4] J. Pople, D. L. Beveridge and P. A. Dobosh, *J. Chem. Phys.*, **1967**, 47, 2026.

[5] J. A. Pople, D. P. Santry and G. A. Segal, *J. Chem. Phys.*, **1965**, 43, S129.

[6] J. E. Ridley and M. C. Zerner, *Chem. Acc.*, **1973**, 32, 111-134.

[7] M. C. Zerner, J. E. Ridley, A. D. Bacon, W. D. Edwards, J. D. Head, J. McKelvey, J. C. Culberson, P. Knappe, M. G. Cory, B. Weiner, J. D. Baker, W. A. Parkinson, D. Kannis, J. Yu, N. Roesch, M. Kotzian, T. Tamm, M. M. Karelson, X. Zheng, G. Pearl, A. Broo, K. Albert, J. M. Cullen, J. Li, G. D. Hawkins, J. D. Thompson, C. P. Kelly, D. A. Liotard, A. V. Marenich, C. J. Cramer, and D. G. Truhlar, ZINDO-MN version 2011, Quantum Theory Project, University of Florida, Gainesville, and Department of Chemistry, University of Minnesota, Minneapolis, **2011**. URL: http://comp.chem.umn.edu/zindo-mn/

[8] M. J. S. Dewar, W. Thiel, *J. Am. Chem. Soc.* **1977**, 99, 4899-4907.

[9] M. J. S. Dewar et al., *J. Am. Chem. Soc.*, **1985**, 107, 3902-3909.

[10] R. O. Freire, *J. Chem. Theory Comput.*, **2010**, 6, 2019-2023.

[11] L. H. Thomas, *Proc. Cambridge Phil.*, **1927**, Soc. 23 (5), 542-548.

[12] E. Fermi, *Rend. Accad. Naz. Lincei*, **1927**, 6, 602-607.

[13] E. Schrödinger, *Phys. Rev.*, **1926**, 28 (6), 1049-1070.

[14] I. N. Levine, *Quantum Chemistry*, 6th ed., Pearson education inc., **2009**.

[15] A. D. Becke, *J. Chem. Phys.*, **1993**, 98, 5648-5652.

[16] J. P. Perdew, K. Burke, and M. Ernzerhof, *Phys. Rev. Lett.*, **1996**, 77, 3865-3868.

[17] C. Lee, W. Yang, and R. G. Parr, *Phys. Rev. B*, **1988**, 37, 785-789.

[18] T. Yanai, D. Tew, and N. Handy, *Chem. Phys. Lett.*, **2004**, 393, 51-57.

[19] Y. Zhao and D. G. Truhlar, *Theor. Chem. Acc.*, **2008**, 120, 215-241.

[20] E. Hohenstein and S. Chill, *J. Chem. Theory Comput.*, **2008**, 4, 1996-2000.

[21] E Runge, E. K. U. Gross, *Phys. Rev. Lett.*, **1984**, 52, 997-1000.

[22] J. B. Foresman, M. Head-Gordon, J. A. Pople, and M. J. Frisch, *J. Phys. Chem.*, **1992**, 96, 135-149.

[23] D. Hegarty and M. A. Robb, *Mol. Phys.*, **1979**, 38, 1795-1812.

[24] C. Adamo and V. Barone, *J. Chem. Phys.*, **1999**, 110, 6158-6169.

[25] J. Heyd and G. E. Scuseria, J. *Chem. Phys.*, **2004**, 121, 1187-1192.

[26] A. R. Leach, Molecular Modelling: Principles and Applications, 2nd ed., Prentice Hall: Dorchester, UK, **2001**.

[27] N. L. Allinger, Y. H. Yuh, and J-H. Lii, *J. Am. Chem. Soc.*, **1989**, 111, 8551-8565.

[28] N. L. Allinger, F. Li, L. Yan and J. C. Tai, *J. Comput. Chem.*, **1990**, 11, 868-895.

[29] A. K. Rappé and W. A. Goddard III, *J. Phys. Chem.*, **1991**, 95, 3358-3363.

[30] A. K. Rappé, C. J. Casewit, K. S. Colwell, W. A. Goddard III and W. M. Skiff, *J. Am. Chem. Soc.*, **1992**, 114, 10024-10035.

[31] L. Verlet, *Phys. Rev.*, **1967**, 159, 98-103.

[32] W. C. Swope, H. C. Andersen, P. H. Berens and K. R. Wilson, J. Chem. Phys., 1982, 76, 637-649.

[33] D. Beeman, *J. Comp. Phys.*, **1976**, 20, 130-139.

[34] A. Kukol, *J. Chem. Theory Comput.*, **2009**, 5, 615-626.

[35] L. Yang, C. H. Tan, M. J. Hsieh, J. Wang, Y. Duan, P. Cieplak, J. Caldwell, P. A. Kollman and R. Luo, *J. Phys. Chem. B*, **2006**, 110, 13166-13176.

[36] J. Hénin, W. Shinoda and M. L. Klein, *J. Phys. Chem. B*, **2008**, 112, 7008-7015.

[37] N. Metropolis and S. Ulam, *J. Am. Stat. Assoc.*, **1949**, 44, 335-341.

[38] N. Metropolis, A. W. Rosenbluth, M. N. Rosenbluth, A. H. Teller and E. Teller, *J. Chem. Phys.*, **1953**, 21, 1087-1092.

[39] J. R. Beeler, *Phys. Rev.* **1966**, 150, 470-487.

[40] A. F. Voter, Rad. Eff. Sol. **2007**, 235, 1568-2609.

[41] A. Nitzan, Chemical Dynamics in Condensed Phases: relaxation, transfer, and reactions in condensed molecular systems, 1st ed., Oxford University Press, Oxford, **2007**.

[42] Gaussian 09, Revision D.01, M. J. Frisch, G. W. Trucks, H. B. Schlegel, G. E. Scuseria, M. A. Robb, J. R. Cheeseman, G. Scalmani, V. Barone, B. Mennucci, G. A. Petersson, H. Nakatsuji, M. Caricato, X. Li, H. P. Hratchian, A. F. Izmaylov, J. Bloino, G. Zheng, J. L. Sonnenberg, M. Hada, M. Ehara, K. Toyota, R. Fukuda, J. Hasegawa, M. Ishida, T. Nakajima, Y. Honda, O. Kitao, H. Nakai, T. Vreven, J. A. Montgomery, Jr., J. E. Peralta, F. Ogliaro, M. Bearpark, J. J. Heyd, E. Brothers, K. N. Kudin, V. N. Staroverov, R. Kobayashi, J. Normand, K. Raghavachari, A. Rendell, J. C. Burant, S. S. Iyengar, J. Tomasi, M. Cossi, N. Rega, J. M. Millam, M. Klene, J. E. Knox, J. B. Cross, V. Bakken, C. Adamo, J. Jaramillo, R. Gomperts, R. E. Stratmann, O. Yazyev, A. J. Austin, R. Cammi, C. Pomelli, J. W. Ochterski, R. L. Martin, K. Morokuma, V. G. Zakrzewski, G. A. Voth, P. Salvador, J. J. Dannenberg, S. Dapprich, A. D. Daniels, Ö. Farkas, J. B. Foresman, J. V. Ortiz, J. Cioslowski, and D. J. Fox, Gaussian, Inc., Wallingford CT, **2009**. URL: http://www.gaussian.com

[43] J. W. Ponder and F. M. Richards, *J. Comput. Chem.*, **1987**, 8, 1016-1024. URL: http://dasher.wustl.edu/tinker/

[44] G.Schaftenaar and J.H. Noordik, *J. Comput.-Aided Mol. Design*, **2000**, 14, 123-134. URL: http://www.cmbi.ru.nl/molden/

[45] Humphrey, W., Dalke, A. and Schulten, K., *J. Molec. Graphics*, **1996**, 14, 33-38. URL: http://www.ks.uiuc.edu/Research/vmd/

[46] URL: http://www.gnuplot.info

[47] A. R. Allouche, *J. Comp. Chem.*, **2011**, 32, 174-182. URL: http://gabedit.sourceforge.net

Chapter 3

Theory of molecular excitons, aggregates, excimers

The molecular exciton theory, first proposed by Kasha et al. in 1965, describes the possible interactions between the electronic excited states of weakly interacting dimers. The theory relates the reciprocal molecular orientation to the energy and oscillator strength of the resulting excited states. This represents a fundamental starting point to develop models explaining the spectral features and the photophysics of molecular aggregates, on the assumption that only interactions between neighboring molecules are considered.

In the last section, a different kind of dimeric interaction usually associated to polycyclic aromatic hydrocarbons (PAHs) will be presented. This arises when two molecules that do not interact in their ground state possess instead a bound excited state, yielding excimers, or "excited dimers".

3.1   Exciton splitting in dimers

In this section, the fundamental theoretical framework underlying Kasha's exciton theory is presented [1], using the wavefunction formalism for an interacting dimer.

The ground state wavefunction of a dimeric species made by two identical molecules i and j has the form:

$$\Psi_G = \psi_i \psi_j \tag{3.1}$$

The Hamiltonian is

$$H = H_i + H_j + V_{ij} \tag{3.2}$$

where the first two terms represent the unperturbed molecules and the last term is a Coulomb intermolecular interaction potential. The ground state energy of the dimer is thus

$$E_G = E_i + E_j + \int \int \psi_i \psi_j (V_{ij}) \psi_i \psi_j d\tau_i d\tau_j \tag{3.3}$$

As for the excited state:

$$\Psi_E = n\psi_i^\dagger \psi_j + m\psi_i \psi_j^\dagger \tag{3.4}$$

Where $\psi_i^\dagger$ and $\psi_j^\dagger$ denote the localized excited states of molecules i and j, while m and n are coefficients to be determined. The corresponding Schrödinger equation is

$$H(n\psi_i^\dagger \psi_j + m\psi_i \psi_j^\dagger) = E(n\psi_i^\dagger \psi_j + m\psi_i \psi_j^\dagger) \tag{3.5}$$

If we multiply both sides by $\psi_i^\dagger \psi_j$ and integrate, then do the same thing for $\psi_i \psi_j^\dagger$, we end up with a set of equations having the following determinant:

$$\begin{vmatrix} 2H_{ii} - E_E & H_{ij} \\ H_{ji} & H_{jj} - E_E \end{vmatrix} = 0 \tag{3.6}$$

If the molecules i and j are the same, the $H_{ii} = H_{ii}$ and $H_{ij} = H_{ji}$. The solutions have the form:

$$E_E' = H_{ii} + H_{ij} \text{with} \Psi_E' = \frac{1}{\sqrt{2}}(\psi_i^\dagger \psi_j + \psi_i \psi_j^\dagger)$$

$$\tag{3.7}$$

$$E_E'' = H_{ii} - H_{ij} \text{with} \Psi_E'' = \frac{1}{\sqrt{2}}(\psi_i^\dagger \psi_j - \psi_i \psi_j^\dagger)$$

which can be rewritten as:

$$E_E' = E_i^\dagger + E_j \quad + \iint \psi_i^\dagger \psi_j (V_{ij}) \psi_i^\dagger \psi_j d\tau_i d\tau_j + \iint \psi_i^\dagger \psi_j (V_{ij}) \psi_i \psi_j^\dagger d\tau_i d\tau_j$$

$$\tag{3.8}$$

$$E_E'' = E_i^\dagger + E_j \quad + \iint \psi_i^\dagger \psi_j (V_{ij}) \psi_i^\dagger \psi_j d\tau_i d\tau_j - \iint \psi_i^\dagger \psi_j (V_{ij}) \psi_i \psi_j^\dagger d\tau_i d\tau_j$$

The last integral is known as the exciton splitting term ε, that can also be defined as

$$\varepsilon = \frac{\mathbf{M_i M_j}}{r^3} - \frac{3(\mathbf{M_i} \cdot \mathbf{r})(\mathbf{M_j} \cdot \mathbf{r})}{r^5} \tag{3.9}$$

which represents the interaction derived from the exchange of excitation energy between molecules i and j. $\mathbf{M_i}$ and $\mathbf{r}$ are respectively the transition dipole vector and the position vector. If we take the difference between the ground state and the

excited state energy of the dimer, we have

$$\Delta E_{dimer} = \Delta E_{monomer} + \Delta D \pm \varepsilon \qquad (3.10)$$

The first term is just the excitation energy of a single molecule, while the second represents the difference between van der Waals interaction terms.

To conclude, the model describes the exciton state as resulting from a resonance interaction between excited states localized on a single molecule. The nodes in the exciton wavefunction correspond to points where the phase relation between molecular transition dipole moments is changing. If the interaction between non-adjacent molecules is neglected, the theoretical framework developed for excitonic interaction in dimers can be applied to molecular aggregates. In the following section, the exciton energy states and the nature of the exciton splitting term ε will be used to explain the excitonic energy states in molecular aggregates.

3.2   J and H aggregates

Since the first discovery of the J-band by Jelley [2] and Scheibe [3], who studied the photophysics of pseudoisocyanine (PIC), a number of studies have reported this behaviour for a variety of conjugated organic molecules and also polymers. [4] Compared to the monomers, some molecular aggregates are know to exhibit a red shift in their absorption wavelength, while some others present a blue shift. The classification of these two kinds of aggregates has been a milestone in the study of the photophysics of conjugated supramolecular aggregates. The differences between J and H aggregates can be rationalized in terms of the reciprocal orientation of molecular dipole transition moments, that can be either face-to-face or side-to-side. In the first case, the allowed transition will have a lower energy respect to the monomer, while in the second the situation will be reversed (see Figure 3.1).

Besides the consistent red shift in their absorption wavelength, J aggregates are also characterized by a narrowing of the absorption band known as exchange narrowing. Their enhanced radiative constant is due to the strongly allowed nature of their 0-0 transition; this phenomenon is known as superradiance. [5, 6] Anyone who has ever used a camera with a color film has indirectly experienced the ability of J aggregates of cyanines to yield such intense and narrow bands, which allow to selectively react to specific wavelengths.

On the other side, H aggregates have blue-shifted absorption bands, usually with a rich vibrational structure. As for the emission properties, their 0-0 transition is forbidden and thermally activated, while phosphorencence is enhanced. [7]

Besides molecules forming only J or H aggregates, there are also many examples of aggregates having a bi-dimensional structure where both kinds of excitons are
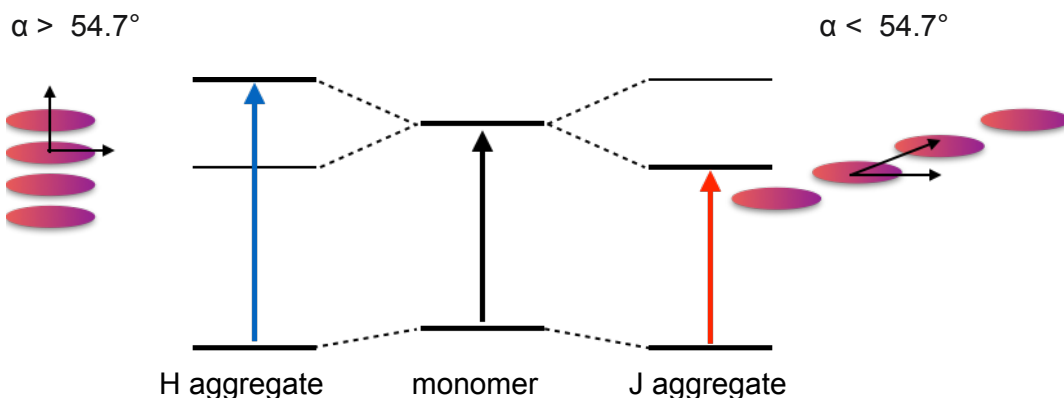
Figure 3.1: Scheme of intermolecular geometries in J and H aggregates. The arrows indicate the allowed transitions from the ground state.

formed. [8] This is typical of molecules like porphyrins. [9–13] In this case the exciton splitting energy, that is the difference between the excited states E' and E", can be defined as

$$\Delta \varepsilon = \frac{|\mathbf{M}|^2}{r_{ij}^3}(1 - 3cos^2\theta) \tag{3.11}$$

where the angle θ depends on the dipole moment orientations: for J aggregates $0 < \theta < 54.7°$, while for H aggregates $54.7° < \theta < 90°$.

3.3 Excimers

The formation of excimers - exc(ited) + (d)imers - is quite common among polyciclic aromatic hydrocarbons (PAHs) and highly π conjugated molecules. Excimers are formed whenever two molecules that are only weakly interacting at the ground state, when electronically excited, reach a bound state:

$$M + M^* \rightarrow [MM]^* \tag{3.12}$$

If we consider the frontier orbitals of each monomer, at the ground state each HOMO is doubly occupied. The four possible excited state configurations of the dimer, depicted in Figure 3.2, originate from all possible ways of promoting an electron from one of the HOMOs to one of the LUMOs.

Two of them can be defined as charge resonance states, while the other two are called exciton states. Within Configuration Interaction [14] scheme, it is possible to describe the excimer wavefunction with a linear combination of the four
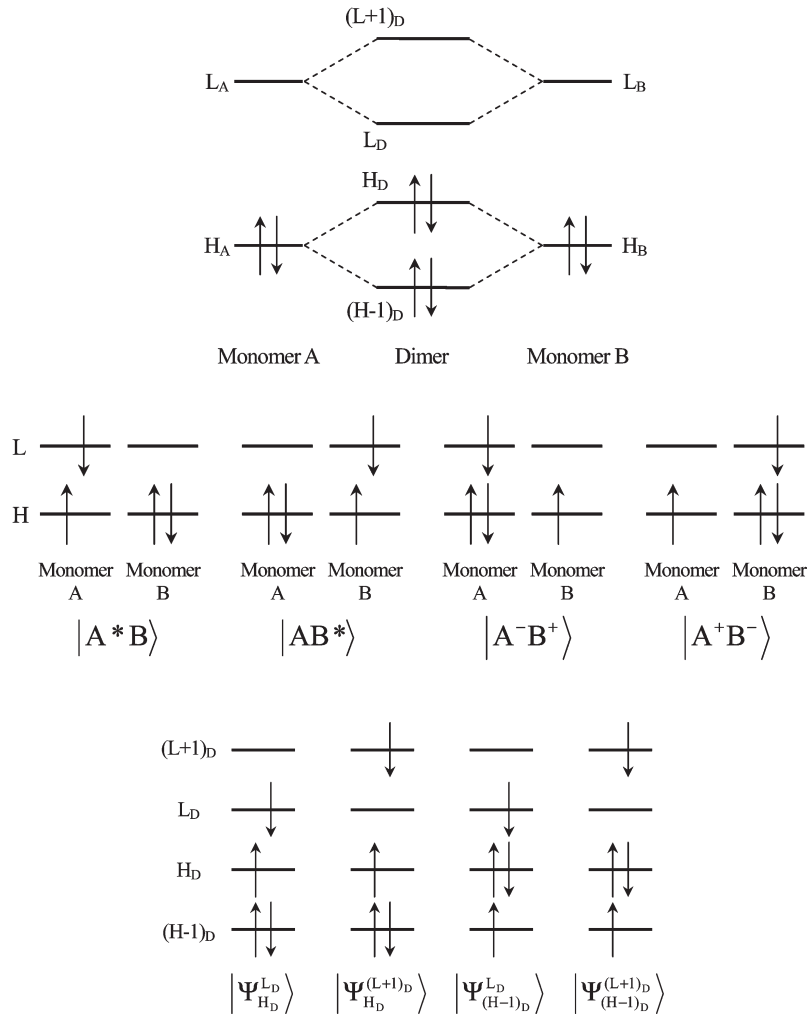
Figure 3.2: On top, the dimer orbitals in the ground state. At the center, the four possible configurations of the dimer excited states: the two exciton states $|A^*B\rangle$ and $|AB^*\rangle$, and the two charge resonance states $|A^+B^-\rangle$ and $|A^-B^+\rangle$. At the bottom, the CI states for the previously described dimer excitations. Adapted from [14].

47

contributions just mentioned. This theoretical approach, though, is computationally demanding and beyond the purpose of this work, that does not focus on the single excimer properties but wants to describe excimers in the context of supramolecular aggregates.

However, previous studies have underlined that some recurring characteristics between different aromatic excimers. First, Azumi and coworkers [15] have reported that there is a linear dependence between the excimer fluorescence band and the quantity IP - EA, where IP is the ionization potential and EA is the electronic affinity of the monomer. Second, another linear dependence connects the absorption energy of the monomer with the emission energy of the excimer: [16]

$$E_{abs,Mono} = 0.73 E_{em,Exc} \tag{3.13}$$

These concept will be further developed in Chapter 4, where the simulation of exciton dynamics of oligo(p-phenyleneethynylene) is discussed.

Bibliography

[1] 1 M. Kasha, H. R. Rawls and M. Ashraf El-Bayoumi, *Pure Appl. Chem.*, **1965**, 11, 371-392.

[2] E. E. Jelley, *Nature*, **1936**, 138, 1009-1010.

[3] G. Scheibe, *Angew. Chemie*, **1937**, 50, 212-219.

[4] D. Mobius, *Adv. Mater.*, **1995**, 7, 437-444.

[5] P. B. Walczak, A. Eisfeld and J. S. Briggs, *J. Chem. Phys.*, **2008**, 128, 044505.

[6] Y. Chen and J. Zhao, *Phys. B Condens. Matter*, **2011**, 406, 579-583.

[7] G. Scholes and G. Rumbles, *Nat. Mater.*, **2006**, 5, 683-696.

[8] A. Eisfeld and J. S. Briggs, *Chem. Phys.*, **2006**, 324, 376-384.

[9] N. C. Maiti, S. Mazumdar and N. Periasamy, *J. Phys. Chem. B*, **1998**, 102, 1528-1538.

[10] O. Ohno, Y. Kaizu and H. Kobayashi, *J. Chem. Phys.*, **1993**, 99, 4128.

[11] S. C. Doan, S. Shanmugham, D. E. Aston and J. L. McHale, *J. Am. Chem. Soc.*, **2005**, 127, 5885-5892.

[12] T. Hasobe, S. Fukuzumi and P. V. Kamat, *J. Am. Chem. Soc.*, **2005**, 127, 11884-11885.

[13] T. Hasobe, S. Fukuzumi and P. V Kamat, *J. Phys. Chem. B*, **2006**, 110, 25477-25484.

[14] S. Shirai, S. Iwata, T. Tani, and S. Inagaki, *J. Phys. Chem. A*, **2011**, 115, 7687-7699.

[15] T. Azumi and S. P. McGlynn, *J. Chem. Phys.*, **1964**, 41, 3131.

[16] A. K. Chandra, *J. Chem. Phys.*, **1968**, 48, 2589.

Chapter 4

Oligo(p-phenylene ethynylene) liquid crystals for organic electronics applications

Oligo(p-phenylene ethynylenes) (OPE) are a class of versatile mesogenic π-conjugated molecules, with possible applications ranging from the field of thermochromic materials to photovoltaic cells. In this chapter, a new family of functionalized OPE liquid crystals is presented and their photophysical and self-aggregating properties are shown. Moreover, a self-developed algorithm for the calculation of exciton dynamics in OPE aggregates is presented. Furthermore, the characterization of the first liquid crystal based on a OPE moiety coupled to a trimetallic nitride template endohedral metallofullerene (TNT-EMF) is outlined.

The photophysical, structural and computational study hereby presented is the result of a collaboration between the University of Bologna, represented by the research groups of Prof. Francesco Zerbetto and Prof. Paola Ceroni, and the CNRS in Strasbourg, represented by the research groups of Prof. Bertrand Donnio and Dr. Delphine Felder-Flesch.

4.1   Introduction

OPEs have been extensively used as molecular wires for opto-electronic devices. Their rigid, π-conjugated core explains both their mesogenic and self-organizing properties. Their propensity to form thermotropic liquid crystalline phases has been exploited to achieve long-range ordered nanostructures, which represent an advantage for both organic electronics and thermochromic nanomaterials. The latter are a kind of stimuli-responsive LCs, which exhibit a color variation upon
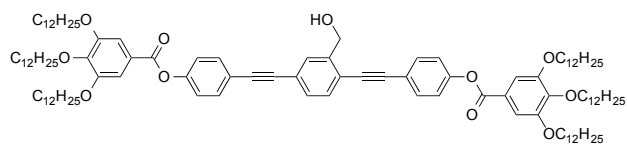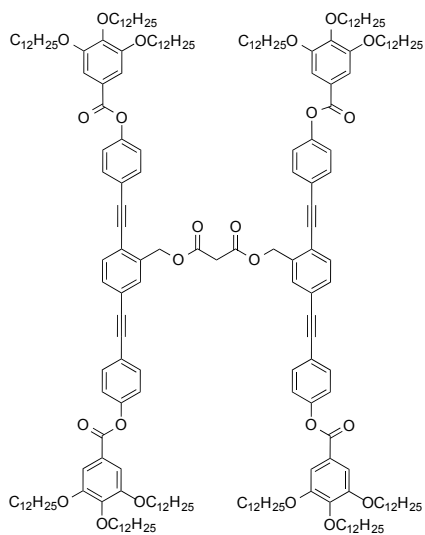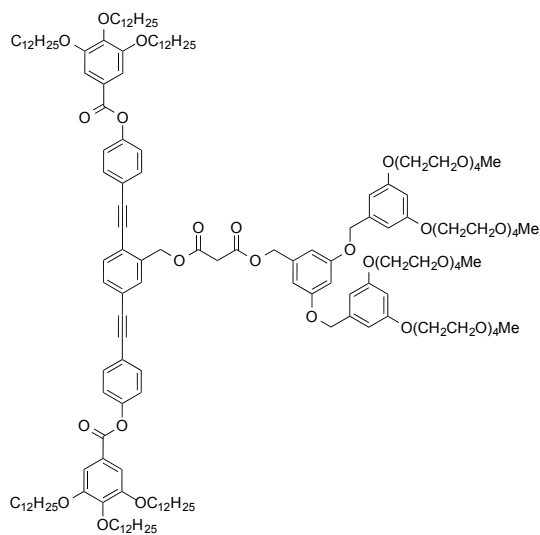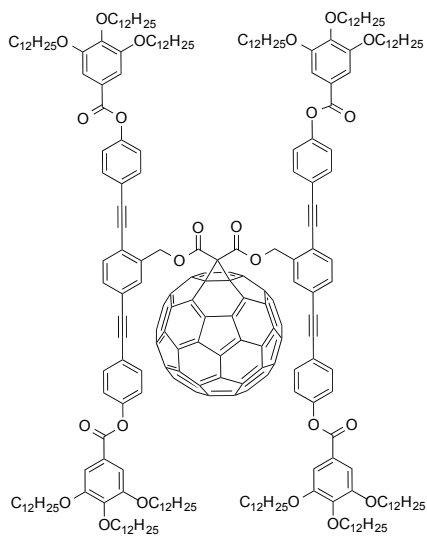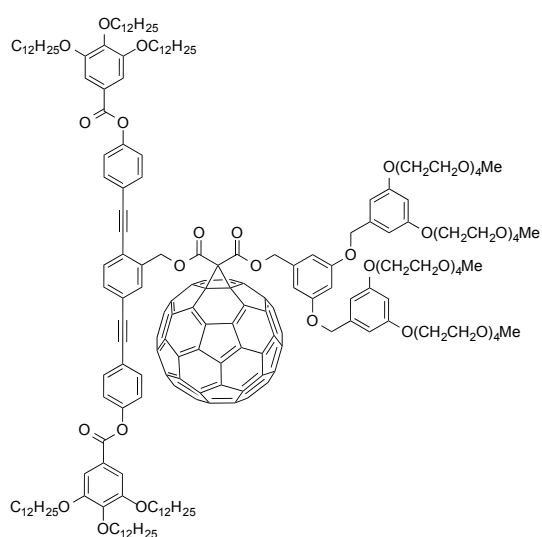
Figure 4.1: Structures of molecules **1-5**.
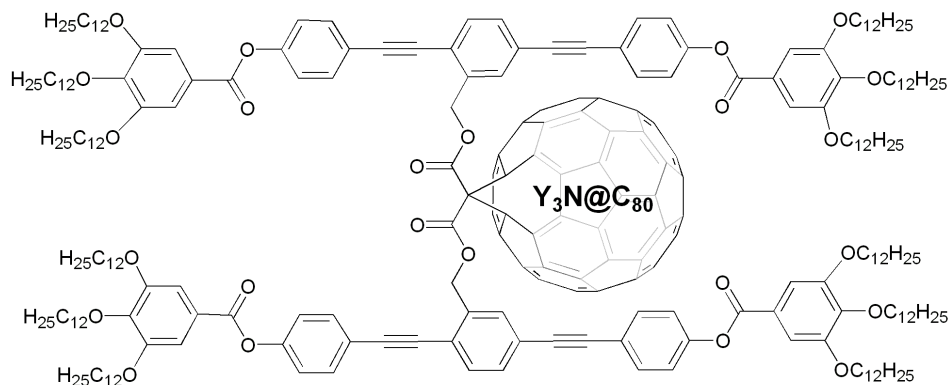
Figure 4.2: Structure of molecule **6**. Adapted from [2].

heating and/or cooling. This is due to the formation of mesophases characterized by a different kind of supramolecular interaction between monomeric units.

In relation to this, OPEs tend to form supramolecular aggregates, either in the solid state, as a thin film or in solution, depending on different factors: i) the presence of substituents and their steric hindrance; ii) the temperature; iii) the solvent. Most importantly, aggregation has an impact on the spectroscopic behaviour of these systems; the photophysics underlying these properties can be understood using a modified version of the theory of molecular aggregates. Therefore, the study of such aggregates appears to be fundamental in order to tune their optical properties. In the first part of this chapter, a study on the photophysical and mesomorphic properties of functionalized OPEs is presented. In more detail, a theoretical model that simulates the exciton dynamics of OPE aggregates is developed starting from experimental measurements in solution and in the LC. This model provides an estimate of the exciton coherence length of OPE aggregates, which is defined as the number of molecular units over which the exciton is delocalized. [3] This joint experimental and theoretical investigation contributes to define a clear picture of the structure-property relationship of OPEs and is a starting point for the further development of smart liquid crystalline materials.

Due to their high absorptivity and their self-organizing properties, OPE units can also be used as donor moieties in organic photovoltaic cells. In the second part of this chapter, the theoretical and experimental characterization of an OPE functionalized with an endohedral metallofullerene is discussed.

Metal-containing fullerenes, and particularly trimetallic nitride template endohedral metallofullerenes (TNT-EMFs), [4] are attracting increasing attention [5, 6] not only for their fascinating structure and the possibility to stabilize metallic

nitrides, but also for their outstanding electronic and optical properties. TNT-EMFs are noteworthy electron-acceptors. [7–12] They also possess larger absorption coefficients than C_{60} in the visible region, making them promising candidates for replacing the well-known phenyl-C61-butyric acid methyl ester (PCBM) in bulk heterojunction solar cells. [13, 14] They could then be used as potential auxiliary materials for singlet-exciton dissociation at the donor-acceptor interfaces, providing charge transport pathways across the semiconducting layer. [15] Thus, chemical functionalization of TNT-EMFs with mesogenic, π-conjugated moieties appears an original solution to reach self-organization and to obtain processable materials. Although many LC fullerenes have been reported since the early 90s, [10, 16–19] none of the previous studies concerns the TNT-EMFs family. [2] In the final part of this chapter the photophysical, structural and electronic properties of the first exemplar of this novel class of compounds will be outlined. This research work illustrates a new paradigm in the field of donor-acceptor solar cells.

4.2   Photophysical properties

The solution absorption spectra (CH_2Cl_2, c $= 5 \times 10^{-6}$ M) of molecules **1-6** are shown in Figures 4.3 and 4.5. They share a strong absorption band with a maximum centred at 326 nm, which is readily assigned to the OPE chromophore. This band is strongly present also in the spectrum of the simplest molecule, namely **1** (Figure 4.1). The bands at ca. 260 and 480 nm are typical of the fullerene chromophores and are indeed present only for the dyads **4** and **5**. Excitation at 326 nm in the absorption band of the OPE moiety yields the fluorescence spectra reported in Figure 4.4. The spectra are proportional to the relative emission quantum yields since they were recorded for solutions characterized by the same absorbance at the excitation wavelength. All spectra present a vibrationally resolved structured band with maximum at 360 nm due to the radiative deactivation of the fluorescent excited state of the OPE chromophore.   The absorption spectra of **4** and **6** in toluene solution show the contribution of the two constituent chromophores: the band at 325 nm is mainly due to the OPE units, while the absorption at $\lambda >$ 380 nm is characteristic of the fullerene core (Figure 4.5). In particular, the absorption coefficient of **6** in the visible region is much higher than that of **4** and extends up to 750 nm due to the presence of the endohedral fullerene core.
Emission spectra of **4** and **6** in de-aerated toluene solutions were recorded upon excitation at 325 nm, the absorption peak of OPE (4.4). The spectra feature two bands: the first one, at ca. 365 nm, belongs to the OPE moieties and is strongly quenched; the second one, in the 680-900 nm region, which can be attributed to the fullerene core (Table 4.2). The quenching of the OPE fluorescence and the sensitization of the fullerene emission is due to a $\backsim$ 100% efficient energy transfer.
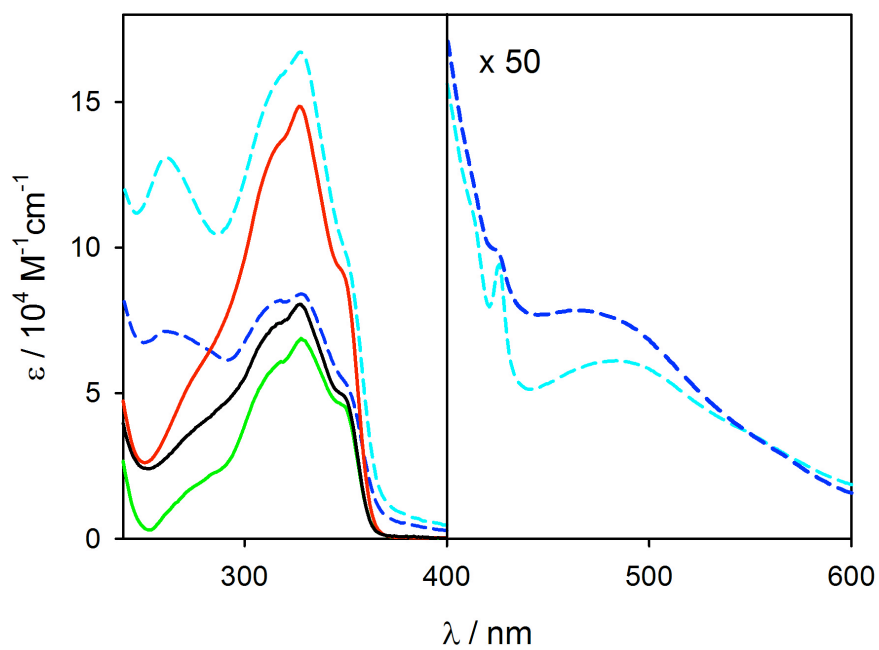
Figure 4.3: Absorption spectra of compounds **1** (black line), **2** (red line), **3** (green line) and of the dyads **4** (cyan line) and **5** (blue line) in dichloromethane solution. Reproduced with permission from [2].
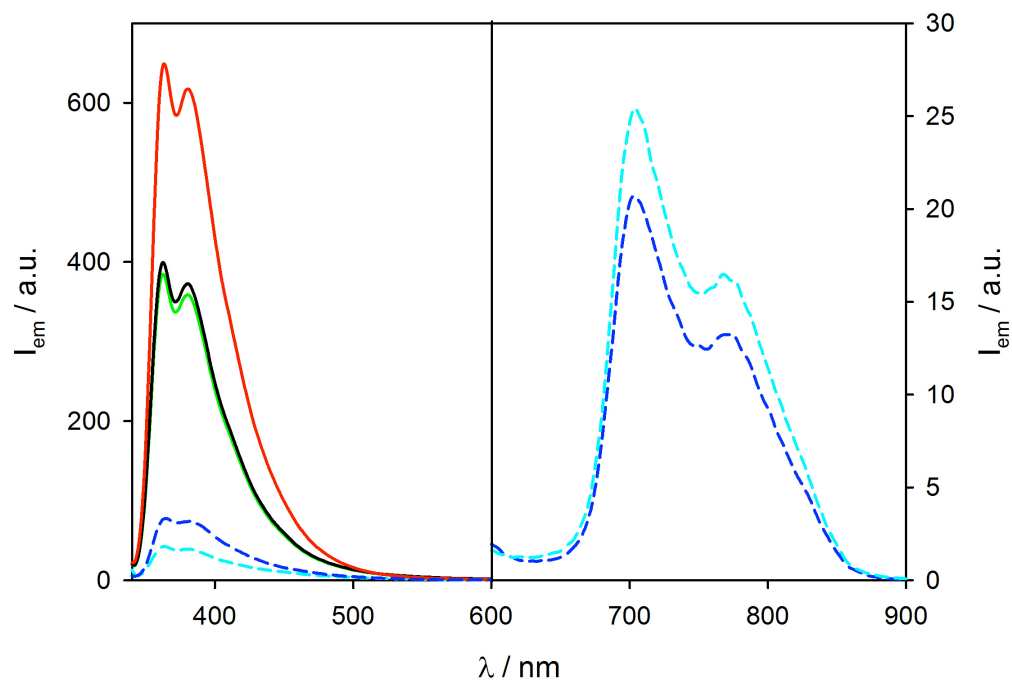
Figure 4.4: Fluorescence spectra of compounds **1** (black line), **2** (red line), **3** (green line) and of the dyads **4** (cyan line) and **5** (blue line)in air-equilibrated dichloromethane solution. The investigated solutions have the same absorbance at $\lambda_{ex} = 326$ nm in order to make possible a comparison of the relative quantum yields. Note that the emission spectra with maximum at 704 nm refer to the right axis. Reproduced with permission from [2].

Table 4.1: Summary of the photophysical data of compounds **1** - **5** in dichloromethane solution at 298 K. Adapted from [2].

	Absorption		Emission		
Compound	λ_{max} (nm)	/ $\varepsilon(10^4\ M^{-1}\ cm^{-1})$	λ_{max} (nm)	τ(ns)	Φ_{em}[a]
1	327	8.4	380	< 0.8	0.053
2	326	16.2	380	< 0.8	0.08
3	328	7.1	380	< 0.8	0.052
4	326	16.5	380	< 0.8	0.005
	482	0.12	704	1.5	3.5×10^{-4}
5	328	7.8	380	< 0.8	0.003
	470	0.16	704	1.6	3.3×10^{-4}

[a]Emission quantum yields were measured in dichloromethane using anthracene in EtOH as the standard.

The same result was observed for compound **4**. Therefore, the two OPE units act as highly efficient light-harvesting antennae for the sensitization of the fullerene emission.

An important difference between the two derivatives concerns the fullerene emission: in the case of **4**, a very weak fluorescence ($\varphi_{em} = 0.03\%$) with a lifetime of 1.5 ns is observed, as expected for C_{60} derivatives. In contrast, compound **6** shows outstanding luminescence properties in the near-IR region, even larger than the non-functionalized model $Y_3N@C_{80}$. As reported in [2], the emitting excited state of **6** is: (i) slightly lower in energy compared to the non-functionalized endohedral fullerene, (ii) quite highly emitting (8.0% in de-aerated solution), (iii) extremely long-lived (16 µs at 298 K, 20 times higher than $Y_3N@C_{80}$ and 13 ms at 77 K), and (iv) highly sensitive to the presence of dioxygen in fluid solution. The same emission band is observed in the solid phase, both in the amorphous and LC mesophase, with a strong quenching by dioxygen (see Table 4.2).

Aggregation

For the most emissive compounds **1** - **3**, the effect of aggregation and self-organization on the emission properties was investigated by two different approaches: (i) increase of the concentration of the chromophore in dichloromethane solution; (ii) addition of a more polar solvent like methanol to the dichloromethane solutions.
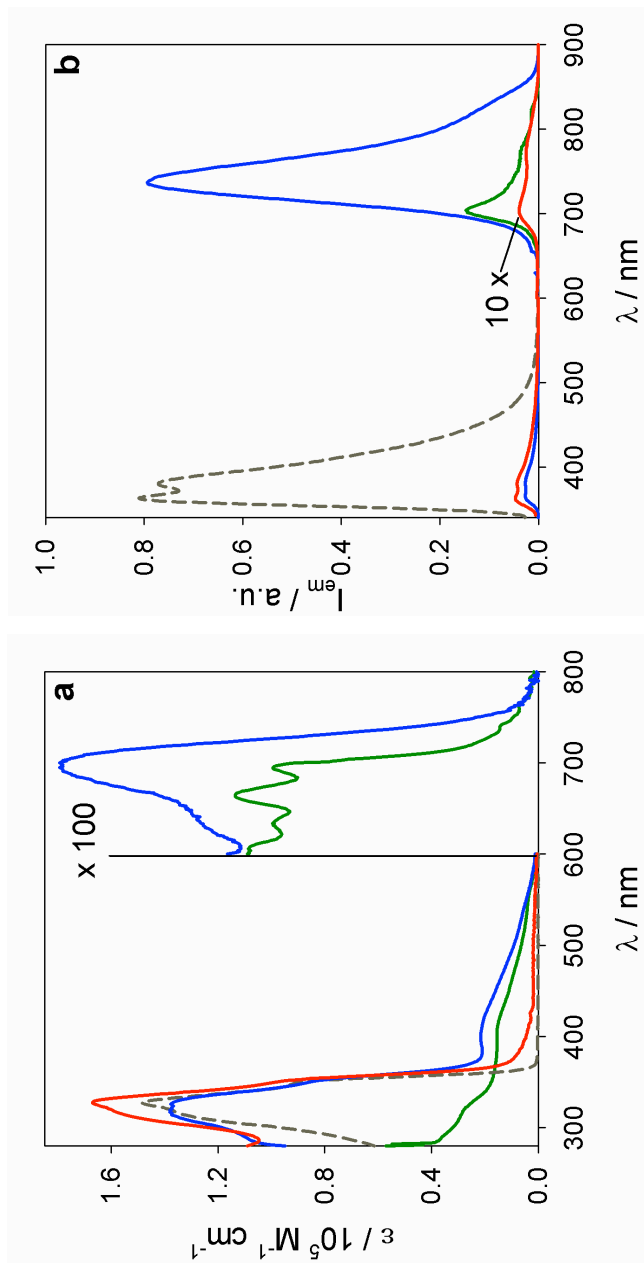
Figure 4.5: Absorption (a) and emission (b) spectra of **6** (blue line), **4** (red line), **2** (dashed gray line), and $Y_3N@C_{80}$ (green line) in de-aerated toluene solution at 298 K. $\lambda_{ex} = 325$ nm. The emission intensities are registered for isoabsorbing solutions at the λ_{ex}. Reproduced with permission from [2].

Table 4.2: Emission properties of **2**, **4**, **6** and $Y_3N_{@}C_{80}$ in air-equilibrated or de-aerated (values in brackets) toluene solution, unless otherwise noted. Reproduced with permission from [2].

	298 K				77 K[a]	
	λ_{max} (nm)	Φ_{em}	τ(ns)	$\Phi(^1O_2)$	λ_{max} (nm)	τ(ms)
2	363	0.08	< 0.8 (< 0.8)	-	380 420	-[c]
4	363 704	0.0035 3×10^{-4}	< 0.8 1.5	1	382 -[b]	-[b] -
6	366 743	0.0026 0.0026 0.0041 0.08	< 0.8 (< 0.8) 640 (16×10^3)	- 1	375 760	-[b] 13
$Y_3N_{@}C_{80}$	704	0.0025 0.011	200 780	0.7	690	12×10^{-3}

[a]In toluene:ethanol 1:1 (v/v) rigid matrix.
[b]The emission intensity is too low.
[c]Multiexponential decay.
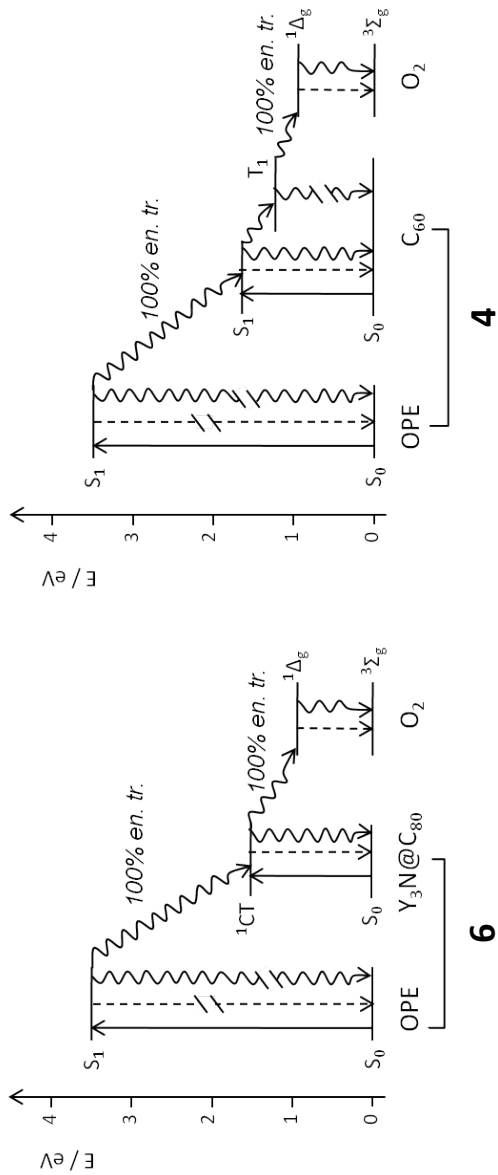
Figure 4.6: Energy level diagrams showing the most relevant radiative (straight lines) and non-radiative (wavy lines) processes for **4** and **6**. The excited states not relevant to the present discussion have been omitted for clarity reasons. Reproduced with permission from [2].

As to the first approach, in the range 1.7×10^{-7} - 8.6×10^{-6} M, no change in the shape of the absorption and emission spectra was observed. The absorbance was proportional to the concentration, as expected by the Lambert-Beer law, and the emission quantum yield was constant. On the other hand, in the case of compound **1** and **2** strong differences in the photophysical properties were observed in different solvents at a concentration of about 5.0×10^{-6} M. In dichloromethane, toluene and cyclohexane the emission spectra were very similar with a maximum at approximately 360 nm, but in a solution of $CH_3OH:CH_2Cl_2$ 90:10 (v/v) a remarkable shift in the emission maximum was observed (Figure 4.7). Also the fluorescence intensity decay exhibited a longer lifetime (τ= 3.6 and 4.1 ns for **1** and **2**, respectively) compared to that recorded in dichloromethane solution (Table 4.4). This behavior suggests the presence of aggregates in polar solvents, as supported by the presence of a tail in the absorption spectrum due to light scattering. A similar red-shifted emission was observed in $CH_2Cl_2:CHCl_3$ 1:1 (v/v) rigid matrix, suggesting that aggregation also occured in rigid matrix. Dynamic Light Scattering (DLS) experiments obtained very broad distributions of species in polar solvents. It is worth noting that no significant shift of the emission spectra was observed for compound **3** upon increasing the solvent polarity, suggesting that the dendronization of the OPE chromophore prevents aggregation in solution.

To better investigate the formation of aggregates and their emission properties as a function of their dimension different solvent mixtures and the effect of time were studied. A solution of **1** in $CH_3OH:CH_2Cl_2$ 82:18 (v/v) that, being freshly prepared, showing only the monomer spectral features, was measured again after six days. The emission spectrum presented features typical of the monomer and small aggregates. The emission of **1** monomer was then subtracted from the total emission to provide the emission spectrum of the aggregates in solution (see Figure 4.8). [1]

Finally, the emissive properties of compounds **1** as a solid film were also investigated. Solutions of **1** in dichloromethane were cast onto the surface of a glass slide and allowed to dry over 2 hours. The emission spectra of each solid film were recorded and the samples placed in the oven at 85°C. The sample emission was then recorded immediately after heating for 5 minutes and after heating over 2 hours: the emission spectra were very similar to that recorded in polar solvents and no substantial shift of the emission maximum was observed.

4.3   Simulation of exciton dynamics

The broad, featureless emission band at 470 nm, present both in solution (Figure 4.7) and in the LC phase and associated response to aggregation of **1**, could be of excimeric nature. Excimer formation for related molecules has been
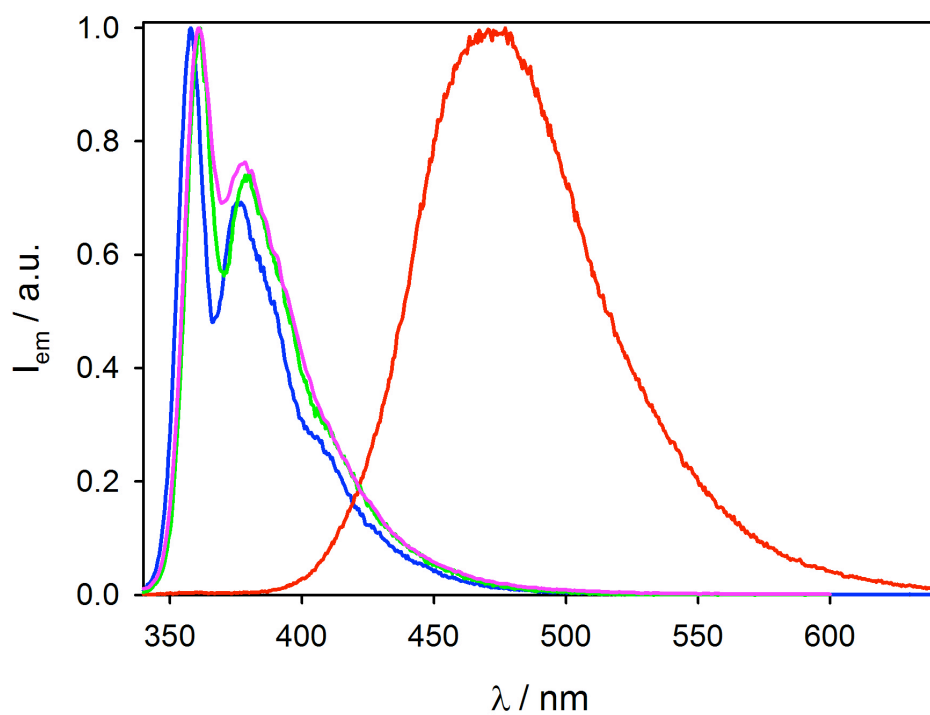
Figure 4.7: Normalised emission spectra of **1** in CH$_3$OH:CH$_2$Cl$_2$ 90:10 (v/v) (red line), cyclohexane (blue line), dichloromethane (pink line) and toluene (green line). Reproduced from [1].
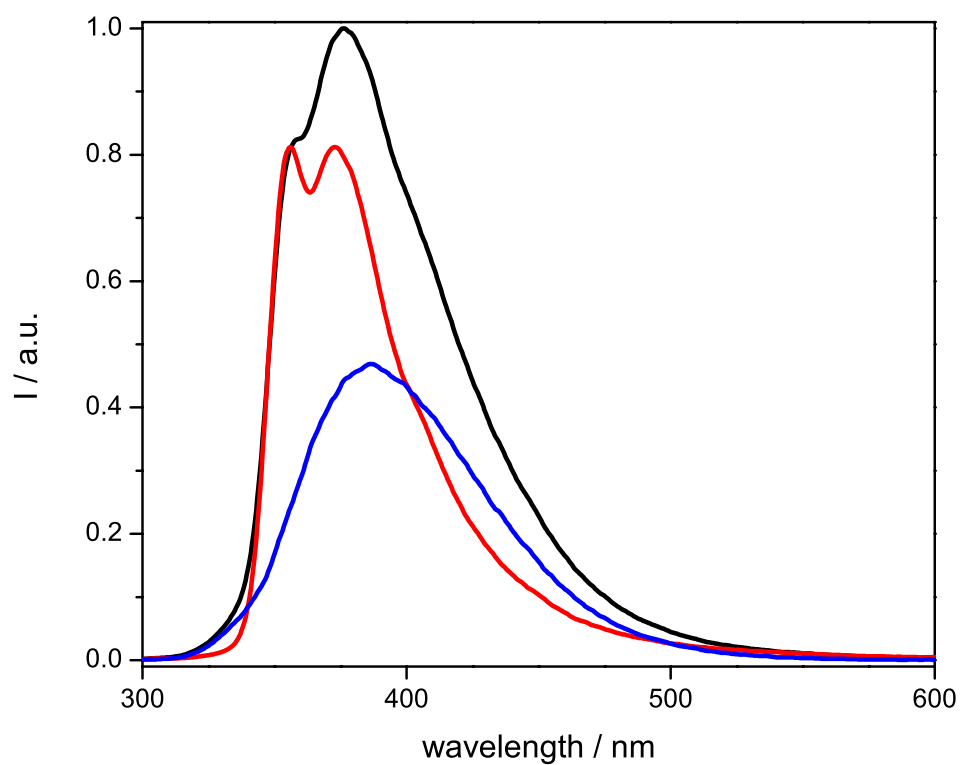
Figure 4.8: Emission spectra of **1** in solution. Black line: Emission spectrum of **1** in ceCH3OH:CH$_2$Cl$_2$ 88:12 (v/v), measured after one week, showing aggregate formation. Red line: Emission spectrum of **1** in DCM, freshly prepared, only due to the monomer. Blue line: estimate of the pure excimer emission obtained by subtracting the monomer contribution multiplied by a numerical parameter. The best fit is obtained when the parameter is set to 0.7. Reproduced from [1].

reported where the emission is characterized by i) a linear relationship between monomer absorption and the aggregate emission energy, and ii) a relationship with the ionization potentials and electron affinities (see Chapter 3). [20, 21] A mono-dimensional model based on interactions between first neighbors was implemented to describe the aggregate emission. This was possible on the assumption that either the different different LC phases (as seen from previous emission measurements of the thin film) or the aggregate obtained in solution with a polar solvent do not exhibit substantial differences in the wavelength and shape. This allows to assume that the extent of exciton delocalization, which depends on the mono-dimensional packing of the π- conjugated mesogens, is similar.

The approach of Gallos et al. [3] was implemented to simulate the emission of the aggregates. The model is based on presence of aggregates of different sizes, N, which are exponentially distributed around an average value N_0 according to Equation 4.1:

$$P(N) = \frac{1}{N_0} e^{-\frac{N}{N_0}} \tag{4.1}$$

where P(N) is the probability of having an aggregate with N molecules.

In general, the electronic states of the aggregates are described by a wavefunction derived from a Hamiltonian in tri-diagonal form:

$$| \Psi_k \rangle = \sqrt{\frac{2}{N+1}} \sum_{n=1}^{N} sin\left(\frac{kn\pi}{N+1}\right) | n \rangle \tag{4.2}$$

where the energies of each a state is given by

$$E_k = E_0 - 2V cos\left(\frac{k\pi}{N+1}\right) \tag{4.3}$$

where E_0 is the energy of the unperturbed non-aggregated state, V is the coupling, and k refers to the excited state involved. We only consider the first excited state of the aggregate, where k=1. E_0 is the energy of the excimer. In practice, because of the photophysical properties of aromatic moieties (see Chapter 3), it is sufficient to multiply it by 0.73. Equation 4.3 becomes

$$E_k = 0.73E_0 - 2V cos\left(\frac{k\pi}{N+1}\right) \tag{4.4}$$

N_0 and V are treated as unknown parameters and fitted to the experimental emission spectrum. To account for the relative intensities of each state, the oscillator strength

is taken as

$$f_k = \frac{2\mu_{exc}}{N+1} cot\left(\frac{k\pi}{2N+1}\right) \tag{4.5}$$

where μ_{exc} is the excimer transition dipole moment. The exciton is delocalized over the entire aggregate, so we can identify N as the exciton coherence length, which may not necessarily correspond to the actual physical dimensions of the aggregate. A Monte Carlo algorithm for the simulation of exciton dynamics in aggregates of **1** was implemented. The excitation pathway along the aggregate is followed until the excitation decays. At each time step the excitation has two possibilities: it can either move to one of the ten closest segments, or it can decay. The decay probability is proportional to the segment length N, while the probability of hopping to a certain segment defined as

$$p_i = W_1 W_2 \tag{4.6}$$

where W_1 is an electrostatic interaction term

$$\sqrt{W_1} \sim U_i = \frac{\mu_M^{*2}}{4\pi\varepsilon_0 \left(\frac{N_i+N_j}{2}\right)^3 a^3} \tag{4.7}$$

and W_2 is defined with a standard Monte Carlo criterion:

$$W_2 \sim \begin{cases} e^{-\Delta E/kT} & \text{if} \quad \Delta E > 0 \\ 1 & \text{if} \quad \Delta E \leq 0 \end{cases} \tag{4.8}$$

At each time step, three random numbers are drawn. The first one is compared to the decay probability; the second determines to which molecule the excitation jumps to, the third is compared to the Monte Carlo criterion of Equation 4.8. When the excitation decays, the energy and oscillator strength of the segment where it was located are collected and used to obtain the emission spectrum of the aggregate.

In order to reproduce the experimental spectral broadening, the Monte Carlo simulated spectrum was convolved with the previously calculated emission of small aggregates (Figure 4.7), which allowed to achieve a good agreement with experimental values (Figures 4.9 and 4.10). In more detail, the fitting was performed by keeping the same value of V for both spectra (measured in solution and in the LC phase) and varying N_0. Note that the exciton coupling parameter used to achieve a good agreement with experimental data is quite high (2500 cm^{-1}). This value is proportional to the spectral shift between the monomer absorption and the aggregate emission, and denotes the peculiarity of this system, reflecting its
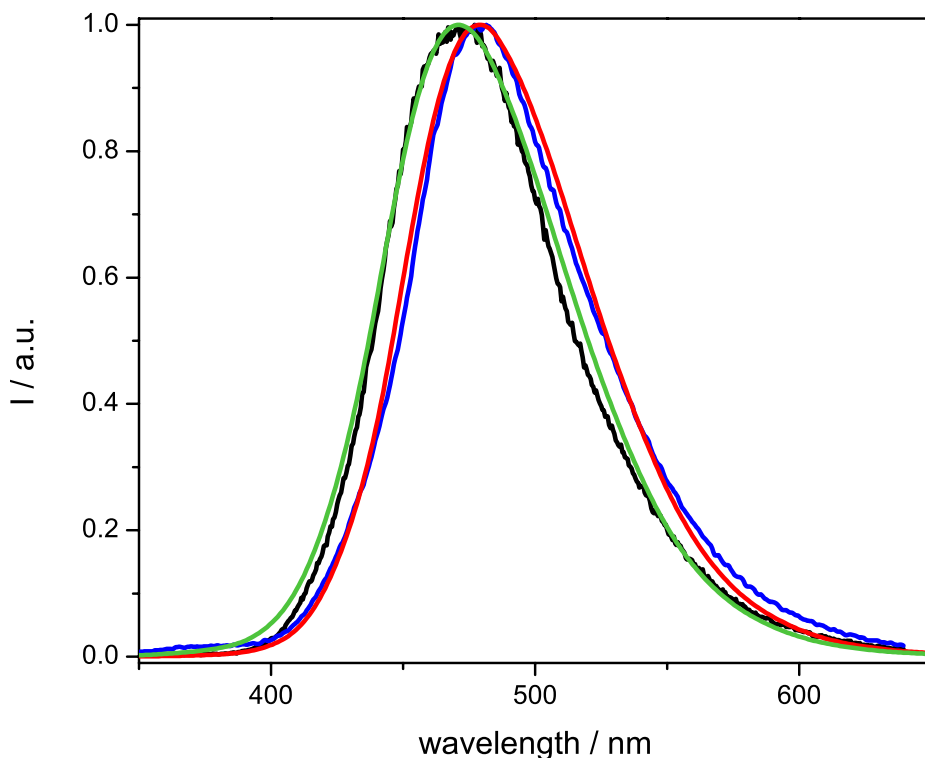
Figure 4.9: Experimental and simulated emission of molecular aggregates of **1**. Black line: emission spectrum of the aggregate in solution. Green line: simulated emission with parameters V = 2500 cm^{-1} and N_0 = 10. Blue line: emission spectrum of the aggregate in the LC phase. Red line: simulated emission with parameters V = 2500 cm^{-1} and N_0 = 55. Reproduced from [1].

remarkable tendency to aggregate even at low concentration. The values of N_0 reflect the lower degree of order of the aggregate formed in solution and represent a good qualitative indication of the aggregate coherence length, an information that would otherwise remain elusive due to the liquid-crystalline nature of OPEs.

4.4   DFT, TD-DFT and ZINDO calculations

OPE moiety

Absorption and emission of a model compound of **1** without the alkyl substituents have been calculated in the vacuum using TD-DFT at level CAM-B3LYP/6-311G*. The calculated absorption energy (324 nm) is very close to
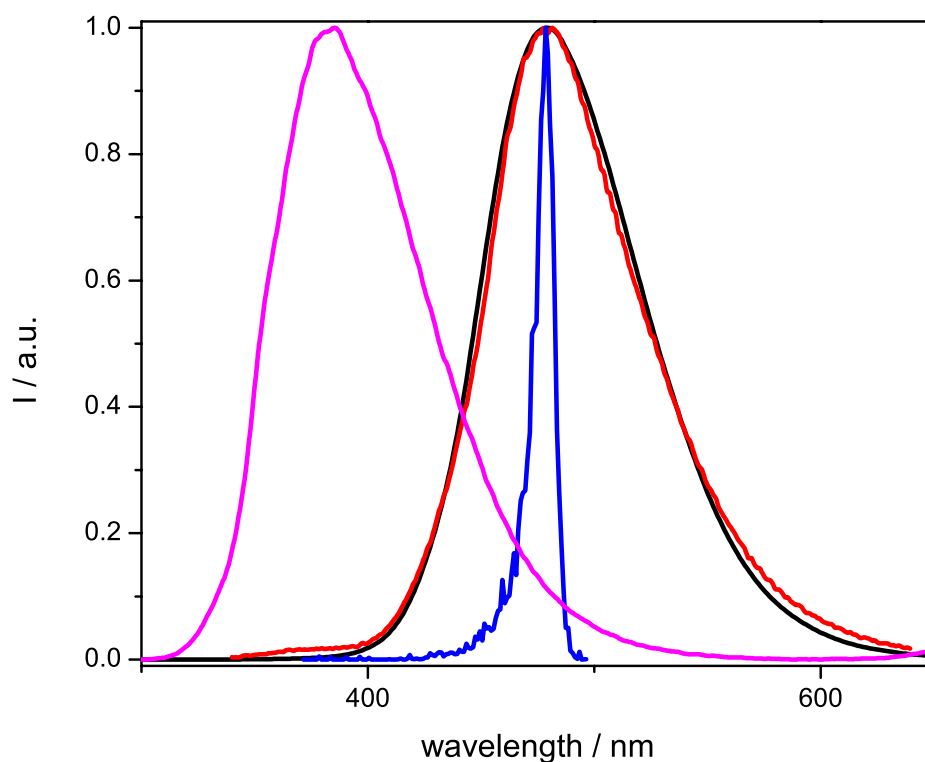
Figure 4.10: Experimental and simulated emission spectra of **1** molecular aggregates. Blue line: Monte Carlo simulation of excimer aggregates emission with parameters $V = 2500$ cm^{-1} and $N_0 = 55$. Pink line: emission of **1** obtained by subtracting the monomer contribution from the spectrum of a sample containing contributions by both excimer and monomer (see Figure 4.8). Black line: Convolution of the two above emission spectra. Red line: Experimental emission of a **1** aggregate in solution. Reproduced from [1].

the experimental value (327 nm). The first excited state was optimized at the same level of theory, yielding a fluorescence peak at 380 nm, while the experimental value is 360 nm. The inaccuracy is less than 1500 cm^{-1}.

Endohedral fullerenes

In order to assess the nature of the long-lived emitting excited state of **4**, DFT and ZINDO calculations were performed on $Y_3N@C_{80}$.

The influence of functionalization on the fullerene states was assessed by comparing the results obtained for $Y_3N@C_{80}$ to those of its model malonate derivative, $Y_3N@C_{80}$-$C(COOCH_3)_2$. Since the outcome of all calculations was very similar for both systems, we concluded that the properties of the fullerene moiety of **1** can be effectively reproduced by only studying $Y_3N@C_{80}$.

Furthermore, results obtained with $Y_3N@C_{80}$ and compared to those obtained for $Sc_3N@C_{80}$, a closely related EMF with a similar absorption spectrum, which although does not emit.

Initially, the clusters were pre-optimized at level PM6. [22] The resulting structures were then reoptimized using DFT. The DFT optimized geometries at B3LYP/6-311G*/MWB28 level agreed with the structures proposed earlier. [23] Both Sc_3N and Y_3N are planar. The amount of intramolecular charge transfer is larger for $Y_3N@C_{80}$ than $Sc_3N@C_{80}$, with the Y_3N doped-cage that receives 3.84 (4.99) electrons while the corresponding value for the Sc_3N doped cage is 2.98 (3.41) with the B3LYP (HSE06) functional. The large values of charge-transfer suggest that molecule-cage Coulomb interactions play an important role in the structure and properties of these endohedral clusters.

Further time-dependent DFT and ZINDO calculations confirmed that the lowest electronically excited singlet state S_1 of both $Sc_3N@C_{80}$ and $Y_3N@C_{80}$ is mainly a HOMO-LUMO transition. The HSE06/6-311G*, CAM-B3LYP/6-311G* and INDO/S results locate S_1 of $Y_3N@C_{80}$ at 2.02, 2.55, and 1.72 eV (Figure 4.11). For $Sc_3N@C_{80}$, the corresponding values are 1.72, 2.20, 1.74 eV. Remarkably, ZINDO is the only method able to correctly locate both the lowest and highest energy states of $Y_3N@C_{80}$, yielding a better qualitative and quantitative description of the absorption transitions with respect to DFT.

A crucial difference between $Sc_3N@C_{80}$ and $Y_3N@C_{80}$ emerges when the molecular orbitals involved in S_1 are inspected visually and the sum of squares of their coefficients is calculated. (Table 4.3). Figure 4.12 shows the HOMOs and LUMOs of the two endohedral clusters. In the non-emitting, short-lived S_1 state of $Sc_3N@C_{80}$ [28] the electron excitation is spread over the entire molecule: both the cage and the endohedrally confined Sc_3N participate in the excitation. In order to better
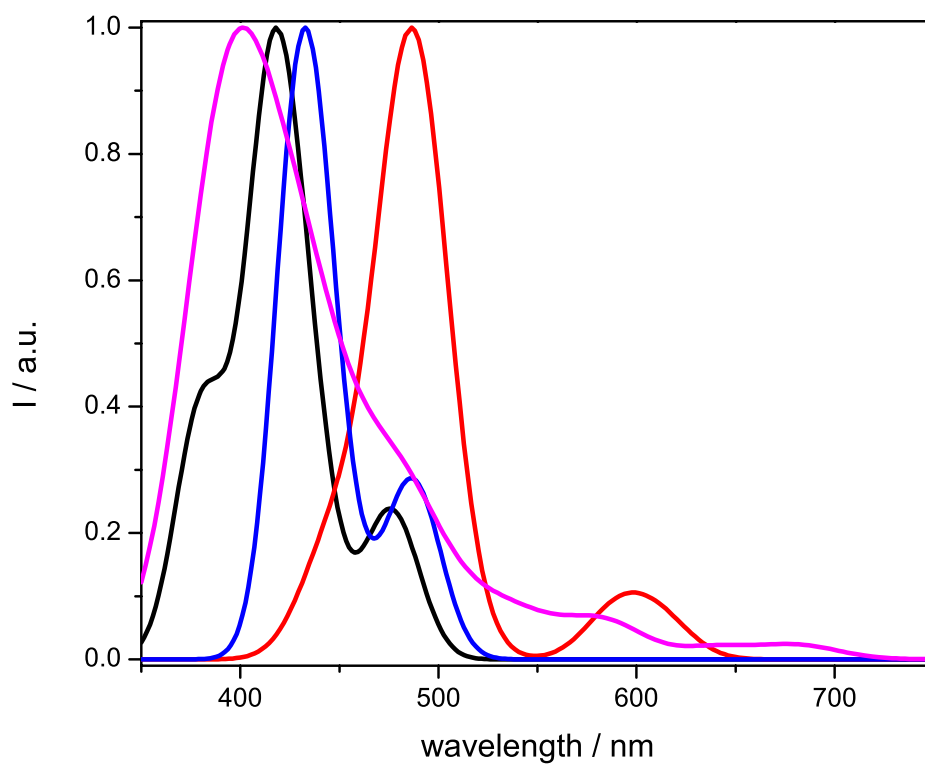
Figure 4.11: Calculated absorption spectra of $Y_3N@C_{80}$ at ZINDO [24] level (pink) and with TDDFT/6-311G*/MWB28 using different functionals (HSE06 [25], red; M06-2X [26], blue; CAM-B3LYP [27], black).

understand the differences in the excited states of $Sc_3N@C_{80}$ and $Y_3N@C_{80}$, some considerations on the nature of Sc and Y ions have to be pointed out. To begin with, Y is commonly associated to lanthanides, mainly Er and Ol, because of its radius (0.89 Åfor Y^{3+}) and the chemistry of its trivalent state. On the other side, Sc^{3+} has a much smaller ionic radius (0.73 Å) and can be instead regarded as similar to Al or Ga. Furthermore, in a previous study of their endohedral complexes $M@C_{24}$, the orbital population analysis highlights that, upon complexation: i) in the case of Sc^{3+}, the occupation of 4s orbitals lowers, but the occupation of 3d orbitals raises; ii) for Y^{3+}, the occupation of both 5s and 4d orbitals lowers. [29] This confirms that Y^{3+} is more prone to transfer its electronic density to the fullerene cage. As far as I_h-C_{80} is concerned, the same pattern is obtained when looking at the ZINDO [24] population analysis, reported in Table 4.3.

To conclude: in the emitting, long-lived S_1 state of $Y_3N@C_{80}$ the electron excitation has a strong charge transfer character from the carbon cage to the endohedrally trapped Y_3N. The peculiar photophysical differences between $Sc_3N@C_{80}$ and $Y_3N@C_{80}$ are now easily accounted for. The electron-excitation to the cage-screened Y_3N determines the long lifetime of S_1 and inhibits the typical fullerenic deactivation pathway characterized by very low emission quantum yields. These findings also agree with previous calculations that showed the charge-transfer character of S_1 of $Y_3N@C_{80}$. [14]

Table 4.3: Orbital population analysis obtained from ZINDO calculations on $Y_3N@C_{80}$, $Y_3N@C_{80}-C(COOCH_3)_2$ and their Sc analogues. The values refer to the sum square of the HOMO and LUMO coefficients relative to the M_3N species. Reproduced with permission from [2].

	$\sum_{MOs} c_i^2$ for M_3N moieties	
EMF	HOMO	LUMO
$Y_3N_@C_{80}$	0.033	0.890
$Y_3N_@C_{80}-C(COOCH_3)_2$	0.046	0.850
$Sc_3N_@C_{80}$	0.031	0.056
$Sc_3N_@C_{80}-C(COOCH_3)_2$	0.033	0.083
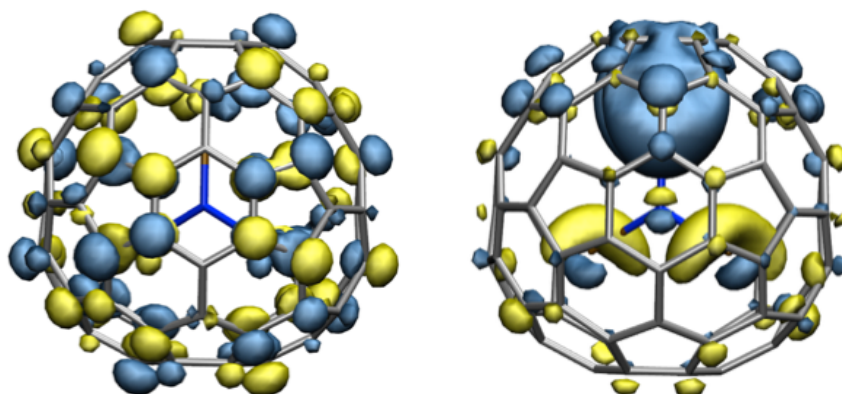
Figure 4.12: HOMO (left) and LUMO (right) of $Y_3N@C_{80}$ at ZINDO level.

Table 4.4: Mesomorphic behaviour of OPE derivatives **1-5**. Reproduced from [1].

Compound	Phase sequence	T_{Peak} (°)	ΔH (J g^{-1})
1	M1 - M2	44	1.9
	M2 - M3	81	0.5
	M3 - Iso	87	17.5
2	M1a - M2a	40	0.8
	M2a - Iso	100	13.2
3	Cr - SmA	38	44.7
	Sm_A - Iso	81	2.5
4	Col_{rec} - Iso	96	3.8
5	Sm_A - Iso	90-100	4.8

Cr: crystalline phase; Sm_A: smectic A phase; Col_{rec}: columnar rectangular phase; Iso: isotropic liquid; M1, M1a, M2, M2a, and M3: two- and three-dimensional mesophases (monoclinic and triclinic).

4.5 Liquid-crystalline properties

OPE 1-3 and 5

All the OPEs exhibit liquid crystalline behavior, as deduced from the investigations by differential scanning calorimetry (DSC), polarized optical microscopy (POM) and small-angle X-ray scattering (SAXS). In fact, despite the presence of the lateral CH_2OH group borne by the central ring, this molecules are based on a typical phasmidic mesogen and are known to self-assemble into columnar phases with temperature. [30] A scheme of the columnar organization is reported in Figure 4.13. The formation of supramolecular structures originates from the folding of the aliphatic tails in excess in between the mesogens sub-layers that consequently break into one-dimensional ribbons, forming the columns at the nodes of a two-dimensional lattice. [31] Preferential orientations of the mesogens within the ribbons are preserved, as sometimes observed in other polycatenar systems.
In table 4.4, the main structural data for molecules **1**-**3** and **5** are reported. As for **1**, the retention of sub-lattice and cell geometry suggests that the lateral packing of the ribbons is maintained beyond the columnar phase. However, he correlation length of the columnar lattice is reduced when going from the M2 to M3.
The aspect and optical textures of the dimer **2** are very similar to those of the monomer **1**, and also compatible with room temperature mesomorphism, although not as rich, which extends even to a slightly higher temperature than for the smaller compound (the isotropization temperature is increased by ca 10°C, Table 4.4). Only one transition between mesophases is visible in the DSC. SAXS analysis confirms this sequence of mesophases (labeled M1a and M2a on increasing temperature).The M2a phase is very similar to the M3 phase of **1**, consisting in a three-dimensional cell with a Col_{rec} sub-lattice containing two strings of bundles. Patterns within the M1a and M1 phases are also similar and indicate for both phases a similar 2D-organization of continuous columns with reduced correlation length.
The SAXS diffractogram of **3** registered at 50°C is consistent with the formation of a lamellar liquid-crystalline phase. The absence of reflections related to columnar superstructures and to ribbon periodicities suggest that neighboring mesogenic sublayers are not registered and that the space filling within these sublayers is statistical.
The SAXS diffraction patterns of the related D-A dyad **5**, recorded at various temperatures, reveal a similar type of mesophase, and overall are in agreement with the formation of a smectic A phase even at room temperature. Indeed, the lamellar periodicity is 94 Å, which is almost double of that of **3**. The layer doubling implies a shift along the layer normal between the electronic density profiles of adjacent mesogenic sublayers. However, beyond this layer doubling, neither reflections of
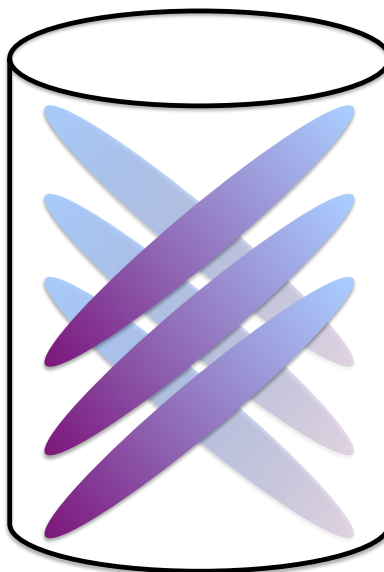
Figure 4.13: Scheme of a possible organization of tilted mesogens inside a columnar LC phase. The number of mesogens occupying a column section is chosen for clarity. Adapted from [30].

ribbon periodicities nor columnar superstructures were detected in the patterns.

Compounds 4 and 6

Fullerene adducts **4** and **6** self-organize into a LC mesophase upon heating (at ca. 70°C for **6** and ca. 80°C for **4**). The mesophase is retained upon cooling down to room-temperature, and can be also recovered when cooling down after having reached the isotropization temperature (at approximately 80°C for **6** and 100°C for **4**).

The characterization of the self-organizing mesophase was performed by small angle X-ray scattering (SAXS) measurements, and results were compared to the outcome of MD calculations.

The columnar structures obtained for **6** and **4** are overall very similar. The central bridge of dOPE generates an unusual triblock architecture which leads to the triple micro-segregation between fullerenes, mesogenic cores and chains in different zones. [32, 33] The data suggest the image of successive molecular plates with a core of 3 interacting fullerenes stacked into columns with an alternating 60°rotation, yielding a strand of hexagonally close packed bowls, as schematized in Figure 4.15. The associated three pairs of OPE mesogens are pressed again the fullerene strands and, due to the short spacers, are spatially constrained. They form a sort
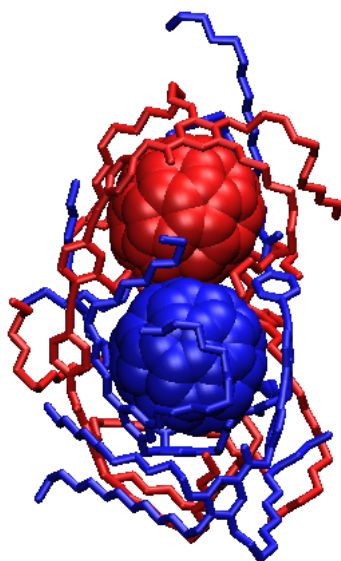
Figure 4.14: Optimized structure of a dimer of **5**, obtained via MD simulations. The colors indicate the different molecules; hydrogens are omitted for clarity.

of two-dimensional net between the fullerenes and the aliphatic chains tubes, to give a structure reminiscent of a Kagome lattice: a periodic 2D tiling of regular hexagons (filled by stacked fullerenes) and triangles (filled by the aliphatic chains) in a 1:2 ratio. [34] The lateral mesogens can adopt various orientations around a preferential one that lies between the parallel and perpendicular limit cases.

Quenched MDs modelling of 5 and 6

A dimer of **5** was optimized using quenched Molecular Dynamics in vacuum. To begin with, the two molecules were brought together in a face-to-face geometry analogous to the supramolecular structure obtained by interpretation of SAXS data. Then, MD simulations were performed (3.5 ns, 400 K, timestep = 1 fs). At every picosecond, the coordinates of the **5** dimer were saved and those having the higher intermolecular energy were optimized separately. The most stable geometry is reported in Figure 4.14, showing a good agreement with the SAXS data.
The structural information obtained via SAXS was the starting point for the optimization of a supercell made by 18 molecules of **6** using quenched MD. First, **6** was optimized as an isolated molecule, then three molecules were brought together at the fullerene-fullerene distance found by SAXS measurements. The trimer was then replicated and rotated by 60°, thus achieving a structure similar to that
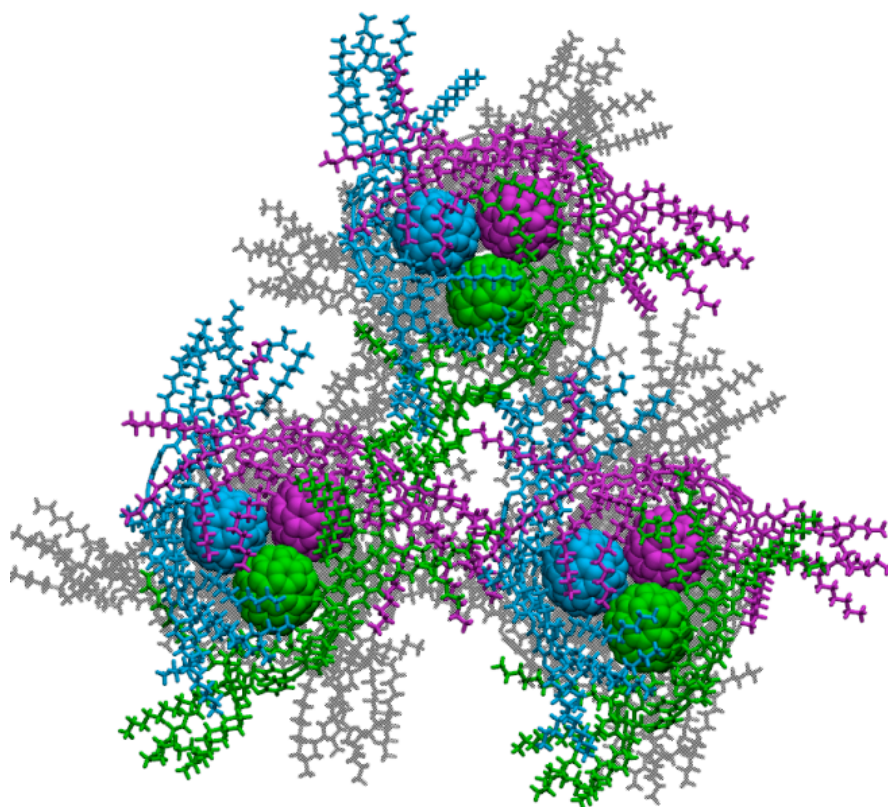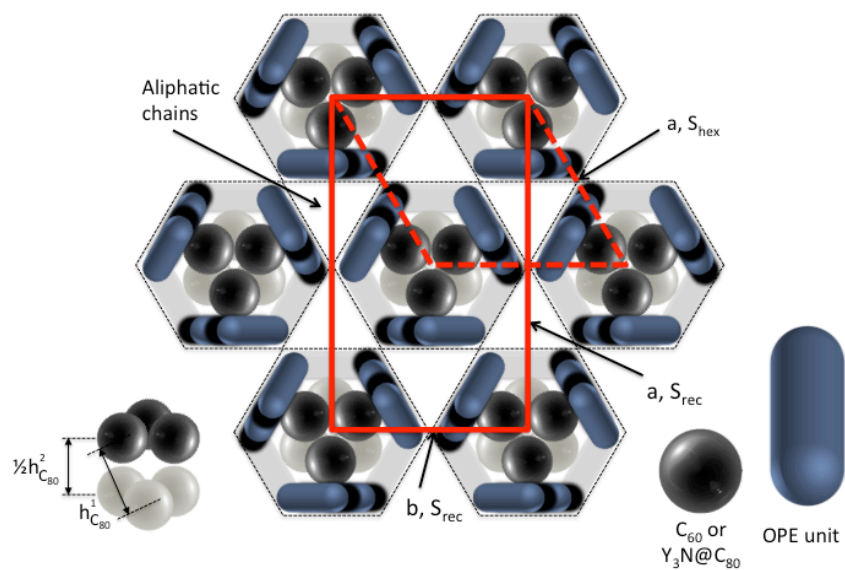
Figure 4.15: Top: schematic view of the supramolecular packing of adducts **4** and **2** (solid and dotted red lines: S_{hex} and S_{rec} lattices of the Col_{hex} and Col_{rec} phases, respectively; dotted-black lines: Kagome lattice). Bottom: MD modelling of a supercell of 18 molecules of **6** arranged as in the (a), the different colors are used to assist the eye. Reproduced with permission from [2].

previously described and depicted in Figure 4.15, which was also optimized, keeping the C_{80}-C_{80} positions fixed and allowing the alkylated dOPE units to relax. Finally, the latter was replicated three times, and quenched MD calculations (500 ps, 300 K, time step = 1 fs) were performed without constraints, yielding a cell of 78.8 × 45.5 Å(Figure 4.15) that compares well with the XRD data of 80.9 × 46.7 Å.

4.6   Conclusion

A highly emissive family of liquid crystalline OPEs has been characterized using spectroscopical, computational and structural tools. This has allowed to establish a structure-property relationship between the observed spectroscopical features and the molecular arrangement in the LC phases. In addition to this, a model for the evaluation of the exciton coherence length of aggregates of **1**, both in the LC phase and in solution, has been successfully applied to this kind of molecules for the first time, to describe one of the first cases of excimer emission from an OPE liquid crystal phase. The exciton dynamics simulations allow to give a qualitative picture of the extent of exciton delocalization in **1**, which complements the structural data obtained via SAXS. Overall, the obtained result should be taken as a starting point to develop a wider library of OPE-based liquid crystals, where a further effort aimed at tuning non-bonding intermolecular interactions would allow to achieve functional thermochromic materials.

Furthermore, the first example of a liquid-crystalline derivative of $Y_3N@C_{80}$ has sen characterized, showing good solubility and remarkable photophysical properties: OPE units acts as 100% efficient light-harvesting antennae to sensitize a bright and long-lived fullerene core emission. These luminescence properties are retained in the mesophase and, coupled to a quite strong absorption in the visible region extending up to 750 nm, open up a variety of applications and especially near-IR luminescent sensors with time-gated detection to shut down fluorescence of the matrix or competing species. The grafting of the mesomorphic dOPE onto the fullerenes promotes mesomorphism in the fullerene adducts, with the induction of columnar phases resulting from the triple segregation between the fullerene (core), mesogens (walls) and chains (continuous medium) accordingly to a Kagome lattice. Such a novel design paradigm should be further exploited to produce an unique class of lanthanidomesogens, with original luminescent and magnetic properties. [35, 36]

Bibliography

[1] K. Toth, J. K. Molloy, M. Matta, B. Heinrich, D. Guillon, G. Bergamini, F. Zerbetto, B. Donnio, P. Ceroni, D. Felder-Flesch, *in preparation*, **2015**.

[2] K. Toth, J. K. Molloy, M. Matta, B. Heinrich, D. Guillon, G. Bergamini, F. Zerbetto, B. Donnio, P. Ceroni, D. Felder-Flesch, *Angew. Chem. Int. Ed.*, **2013**, 52(47), 12303-12307.

[3] L. K. Gallos, A. V. Pimenov, I. G. Scheblykin, M. Van der Auweraer, G. Hungerford, O. P. Varnavsky, A. G. Vitukhnovsky and P. Argyrakis, *J. Phys. Chem. B*, **2000**, 104, 3918-3923.

[4] S. Stevenson, G. Rice, T. Glass, K. Harlch, F. Cromer, M. R. Jordan, J. Craft, E. Hadju, R. Bible, M. M. Olmstead, K. Maltra, A. J. Fisher, A. L. Balch and H. C. Dorn, *Nature*, **1999**, 401, 55-57.

[5] L. Dunsch and S. Yang, *Small*, **2007**, 3, 1298-1320.

[6] J. Zhang, S. Stevenson and H. C. Dorn, *Acc. Chem. Res.*, **2013**, 46, 154.

[7] J. C. Duchamp, A. Demortier, K. R. Fletcher, D. Dorn, E. B. Iezzi, T. Glass and H. C. Dorn, *Chem. Phys. Lett.*, **2003**, 375, 655-659.

[8] C. R. Wang, T. Kai, T. Tomiyama, T. Yoshida, Y. Kobayashi, E. Nishibori, M. Takata, M. Sakata and H. Shinohara, Nature, **2000**, 408, 426-427.

[9] J. Aihara, *J. Phys. Chem. A*, **2002**, 106, 11371-11374.

[10] H. Mamlouk, B. Heinrich, C. Bourgogne, B. Donnio, D. Guillon and D. Felder-Flesch, *J. Mater. Chem.*, **2007**, 17, 2199-2205.

[11] J. R. Pinzón, D. C. Gasca, S. G. Sankaranarayanan, G. Bottari, T. Torres, D. M. Guldi and L. Echegoyen, *J. Am. Chem. Soc.*, **2009**, 131, 7727-7734.

[12] J. R. Pinzón, M. E. Plonska-Brzezinska, C. M. Cardona, A. J. Athans, S. S. Gayathri, D. M. Guldi, M. A. Herranz, N. Martín, T. Torres and L. Echegoyen, *Angew. Chem. Int. Ed. Engl.*, **2008**, 47, 4173-4176.

[13] Y. Takano, S. Obuchi, N. Mizorogi, R. García, M. Á. Herranz, M. Rudolf, D. M. Guldi, N. Martín, S. Nagase and T. Akasaka, *J. Am. Chem. Soc.*, **2012**, 134, 19401-19408.

[14] Y. Takano, S. Obuchi, N. Mizorogi, R. García, M. Á. Herranz, M. Rudolf, S. Wolfrum, D. M. Guldi, N. Martín, S. Nagase and T. Akasaka, *J. Am. Chem. Soc.*, **2012**, 134, 16103-16106.

[15] R. B. Ross, C. M. Cardona, D. M. Guldi, S. G. Sankaranarayanan, M. O. Reese, N. Kopidakis, J. Peet, B. Walker, G. C. Bazan, E. Van Keuren, B. C. Holloway and M. Drees, *Nat. Mater.*, **2009**, 8, 208-212.

[16] S. Campidelli, P. Bourgun, B. Guintchin, J. Furrer, H. Stoeckli-Evans, I. M. Saez, J. W. Goodby and R. Deschenaux, *J. Am. Chem. Soc.*, **2010**, 132, 3574-3581.

[17] J. Vergara, J. Barberá, J. L. Serrano, M. B. Ros, N. Sebastián, R. de la Fuente, D. O. López, G. Fernández, L. Sánchez and N. Martín, *Angew. Chem. Int. Ed. Engl.*, **2011**, 50, 12523-12528.

[18] R. Deschenaux, B. Donnio and D. Guillon, *New J. Chem.*, **2007**, 31, 1064.

[19] Y. Matsuo, A. Muramatsu, Y. Kamikawa, T. Kato and E. Nakamura, *J. Am. Chem. Soc.*, **2006**, 128, 9586-9587.

[20] A. K. Chandra, *J. Chem. Phys.*, **1968**, 48, 2589.

[21] T. Azumi and S. P. McGlynn, *J. Chem. Phys.*, **1964**, 41, 3131.

[22] J. J. P. Stewart, J. Mol. Model., 2007, 13, 1173-1213.

[23] L.-H. Gan and R. Yuan, *ChemPhysChem*, **2006**, 7, 1306-1310.

[24] J. E. Ridley and M. C. Zerner, *Chem. Acc.*, **1973**, 32, 111-134.

[25] T. Yanai, D. P. Tew and N. C. Handy, *Chem. Phys. Lett.*, **2004**, 393, 51-57.

[26] Y. Zhao and D. G. Truhlar, *Acc. Chem. Res.*, **2008**, 41, 157-167.

[27] J. Heyd and G. E. Scuseria, *J. Chem. Phys.*, **2004**, 121, 1187-1192.

[28] J. R. Pinzón, C. M. Cardona, M. A. Herranz, M. E. Plonska-Brzezinska, A. Palkar, A. J. Athans, N. Martín, A. Rodríguez-Fortea, J. M. Poblet, G. Bottari, T. Torres, S. S. Gayathri, D. M. Guldi and L. Echegoyen, *Chemistry*, **2009**, 15, 864-877.

[29] X. Lu, L. Echegoyen, A. L. Balch, S. Nagase and T. Akasaka, Endohedral metallofullerenes, Taylor & Francis Group, **2015**.

[30] H.-T. Nguyen, C. Destrade and J. Malthete, *Adv. Mater.*, **1997**, 9, 375-388.

[31] B. Donnio, B. Heinrich, H. Allouchi, J. Kain, S. Diele, D. Guillon and D. W. Bruce, *J. Am. Chem. Soc.*, **2004**, 126, 15258-15268.

[32] C. Tschierske, *Chem. Soc. Rev.*, **2007**, 36, 1930-1970.

[33] C. Tschierske, *Top. Curr. Chem.*, **2012**, 318, 1-108.

[34] B. Glettner, F. Liu, X. Zeng, M. Prehm, U. Baumeister, M. Walker, M. A. Bates, P. Boesecke, G. Ungar and C. Tschierske, *Angew. Chem. Int. Ed. Engl.*, **2008**, 47, 9063-9066.

[35] C. Piguet, J.-C. G. Bünzli, B. Donnio and D. Guillon, *Chem. Commun. (Camb).*, **2006**, 3755-3768.

[36] K. Binnemans and C. Görller-Walrand, *Chem. Rev.*, **2002**, 102, 2303-2346.

Chapter 5

Effect of an applied electric field on pentacene molecules: from dimers to thin films

Pentacene and its derivatives play a central role in organic electronic applications, and are widely employed in OFETs. In this chapter, pentacene behaviour under the effect of a constant electric field is explored by means of DFT and molecular mechanics, with the aim of identifying some of the issues that limit the stability of these devices.

In the first part of the chapter, the dimerization of pentacene in the presence of an electric field is investigated.The results indicate that cycloaddition can be a possible degradation pathway in low crystallinity thin films, ultimately leading to a worsening of device performances and stability. In the second part, the effect of gate bias on the tilt angle of pentacene in correspondence to grain boundaries is simulated, using two model systems: a pentacene tetramer and a monolayer made by a supercell of 24 molecules. The results are then compared to X-ray measurements performed in real time on working OFETs, as part of a collaboration with Prof. Fabio Biscarini (University of Modena and Reggio Emilia) and Prof. Silvia Milita (CNR-IMM). The general picture given by computational and experimental results could provide a further explanation of the phenomenon of bias stress.

5.1   Introduction

Molecular organization at multiple length scales has a fundamental role in determining the operation characteristics of Organic Field Effect Transistors (OFETs). [1–5] Up to now, a lot of knowledge has been gained on how molec-

ular packing and morphology of thin films affect charge transport in OFETs. It is a matter of fact that the field effect mobility, μ_{fe}, can be improved by increasing the degree of crystallinity and the texturing of the organic semiconductor film. In pentacene, sexithienyl and perylene derivatives [2, 6] it has been reported that molecular order changes across the monolayers, evolving from the thin film phase in the lower layer towards one of the bulk phase polymorphs in the upper layers. It has been also observed the coexistence of molecules with planar orientation and domains of standing molecules in correspondence to island edges and grain boundaries. [7] Whether or not these planar molecules can be incorporated at later stage into the crystalline domains is still a matter of debate. In-plane structural inhomogeneity induced by the dielectric surface has also been reported. [8]

The external electric field applied in OFET has the key function of generating free charge carriers, as previously discussed in Chapter 1. If, up to know, substantial effort has been devoted to control the molecular packing and orientation in thin films, the impact of the electric field produced by the device operation on the film structure is still unknown. Only a single investigation showed a structural modification in pentacene thin films induced by the electric fields during OFET operation, which was measured using Raman spectroscopy, an indirect structural technique. Up to date, substantial evidence of this phenomena remained elusive.

The high reactivity of pentacene is also a major issue for the development of its applications in molecular electronics. [10, 11] Pentacene photo-reactivity and photo-oxidation by singlet oxygen sensitization with the formation of endo-peroxides have been considered responsible for the degradation of pentacene. [12, 13] However, the extremely low solubility of pentacene in all organic solvents accounts for the lack of information with respect to the photochemistry involved.

Dimerization - either thermally or photochemically activated , is crucial in the solution chemistry of pentacene and its substituted derivatives; [14–16] yet its occurrence in the solid state has been more challenging to prove. In 2005, Coppo et al. [17] observed the photodimerization of a substituted pentacene in solution, amorphous and semi-crystalline thin films upon exposure to sunlight. The degree of crystallinity of the sample was proportional to its photostability. In tightly packed domains, dimerization (and also oxidation) is prevented. At grain boundaries, where molecules have more degrees of freedom, there is a higher probability of degradation.

As far as thermal dimerization is concerned, Zade et al. [18] found that the reaction proceeds through a two-step mechanism involving biradical intermediates. Remarkably, the pentacene dimer occupies a special position among acene dimers: while its formation is more exothermic than that of lower acenes, [19] the competing polymerization product is not as favored as it is for longer acenes. In fact, starting

from heptacene, the dimerization tends to proceed further, yielding acene-based polymers. [20]

Despite it being one of the most studied semiconductors in OFET devices, only a few experimental studies on pentacene behavior and reactivity under an applied electric field exist. [21–23] Therefore, it is important to determine whether the application of an electric field favors the dimerization pathway. The latter could in fact concur to the irreversible deterioration of device performances observed in OFETs, reducing their shelf life.

In the first part of this chapter, the thermal cycloaddition pathway of pentacene under the influence of an external electric field is investigated using DFT calculations. The obtained results are then compared to the situation inside the OFET thin film. In the remainder of the chapter, the effect of V_{GS} on the pentacene crystal structure is studied by means of Molecular Dynamics (MD) and Density Functional Theory (DFT) simulations coupled to direct measurements of the structural evolution of pentacene thin film observed during the OFET operation. This investigation was achieved by a collaboration among several research groups involved in the fabrication and characterization of the devices. In particular, the results of X-Ray Diffraction (XRD) measurements in real time on operating OFETs are compared to the outcome of theoretical simulations.

Overall, the interplay between molecular simulations and experimental results provide an insightful perspective on the structural evolution of operating transistors.

5.2   Pentacene dimerization

A DFT study of pentacene cycloaddition mechanism was performed by Zade and coworkers [18], who investigated the formation of the symmetric "butterfly dimer", obtained from cycloaddition at the central rings. The asymmetric 2,3' and 1,3' products are energetically less favored. The preferential reaction path starts by a syn addition taking place in the Van der Waals complex, which represents the most stable configuration for two interacting pentacene molecules (-18.4 kcal mol^{-1}). The first transition state TS1 lies 17.3 kcal mol^{-1} above the dimer, and is a biradicaloid species with an incipient bond length of 2.04 Å. The next intermediate is M_{in}, a local minimum (-8.2 kcal mol^{-1}); its newly formed C-C bond measures 1.62 Åwhile the dihedral C-C-C'-C' is 52°. The reaction then terminates through TS2, where the second C-C bond is being formed (C-C' = 1.66 Å, C-C-C'-C' = 12°). The 3,3' dimer is finally obtained, 34.5 kcal mol^{-1} more stable than its isolated precursors. All biradical species involved are singlets, as predicted by the theory of acene biradicals. [24]

In order to reproduce the reaction pathway, all the intermediates were first
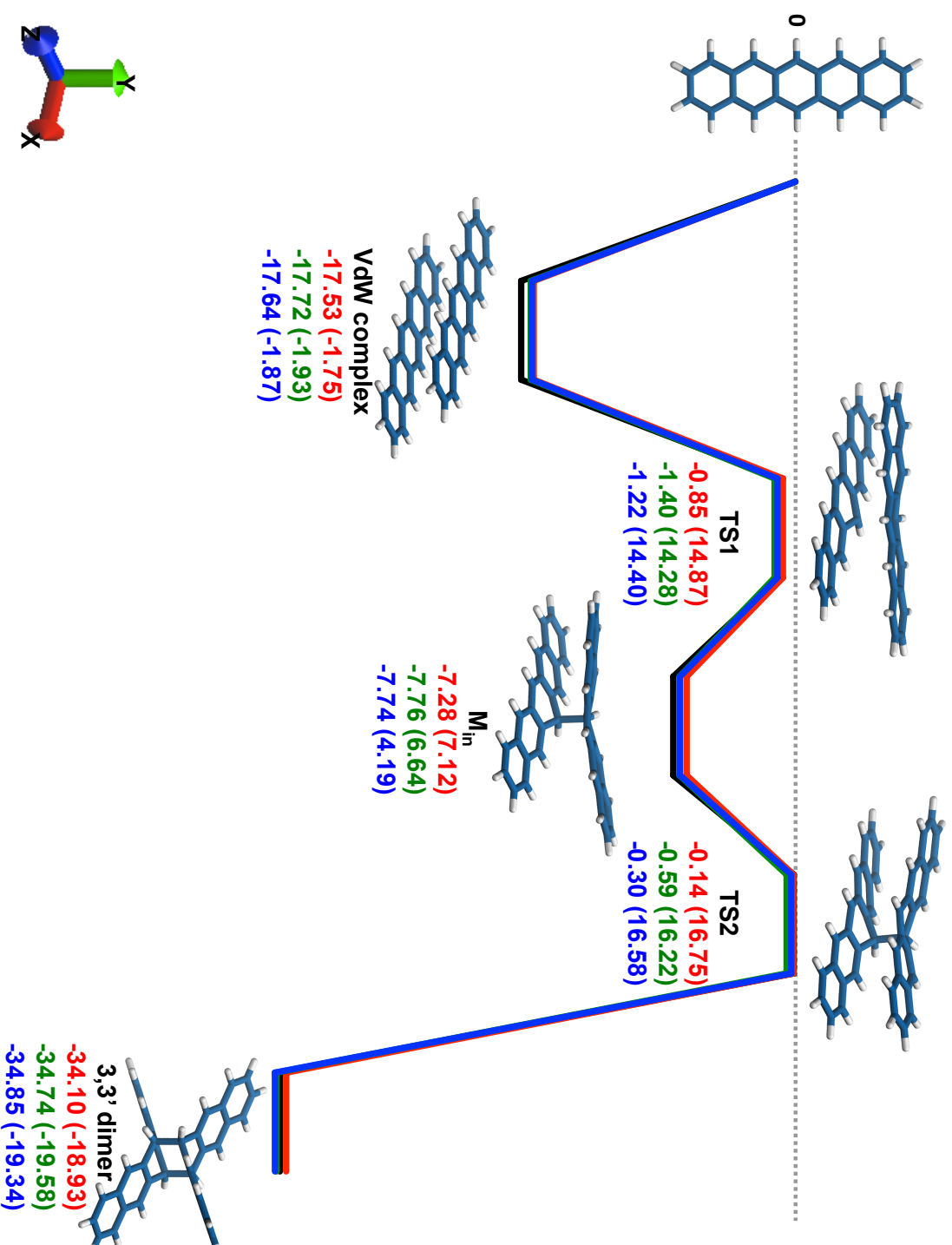
Figure 5.1: Pentacene dimerization scheme in the presence of an applied electric field of 1 V/nm along X (red line), Y (green line) or Z (blue line). X corresponds to the pentacene long axis, Y to the direction of the sp^3 bonds, and Z to the short axis. The black line refers to the reaction path in the absence of an applied electric field. The relative energies with ZPVE and Gibbs free energies in parentheses are calculated with respect to two isolated pentacene molecules (see Table 5.2). Reproduced from [9].
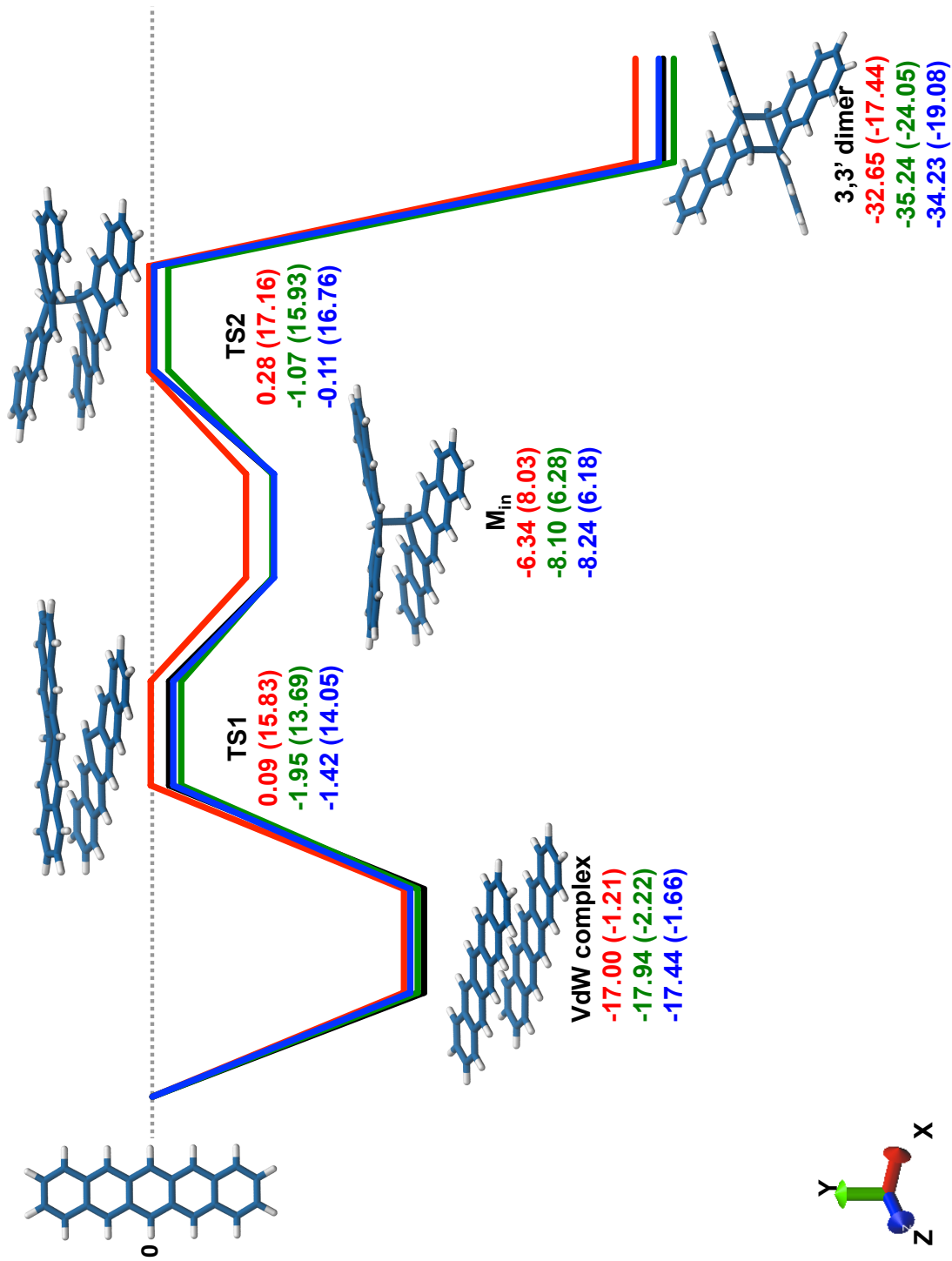
Figure 5.2: Pentacene dimerization scheme in the presence of an applied electric field of 2 V/nm along X (red line), Y (green line) or Z (blue line). X corresponds to the pentacene long axis, Y to the direction of the sp3 bonds, and Z to the short axis. The black line refers to the reaction path in the absence of an applied electric field. The relative energies with ZPVE and Gibbs free energies in parentheses are calculated with respect to two isolated pentacene molecules (see Table 5.2). Reproduced from [9].
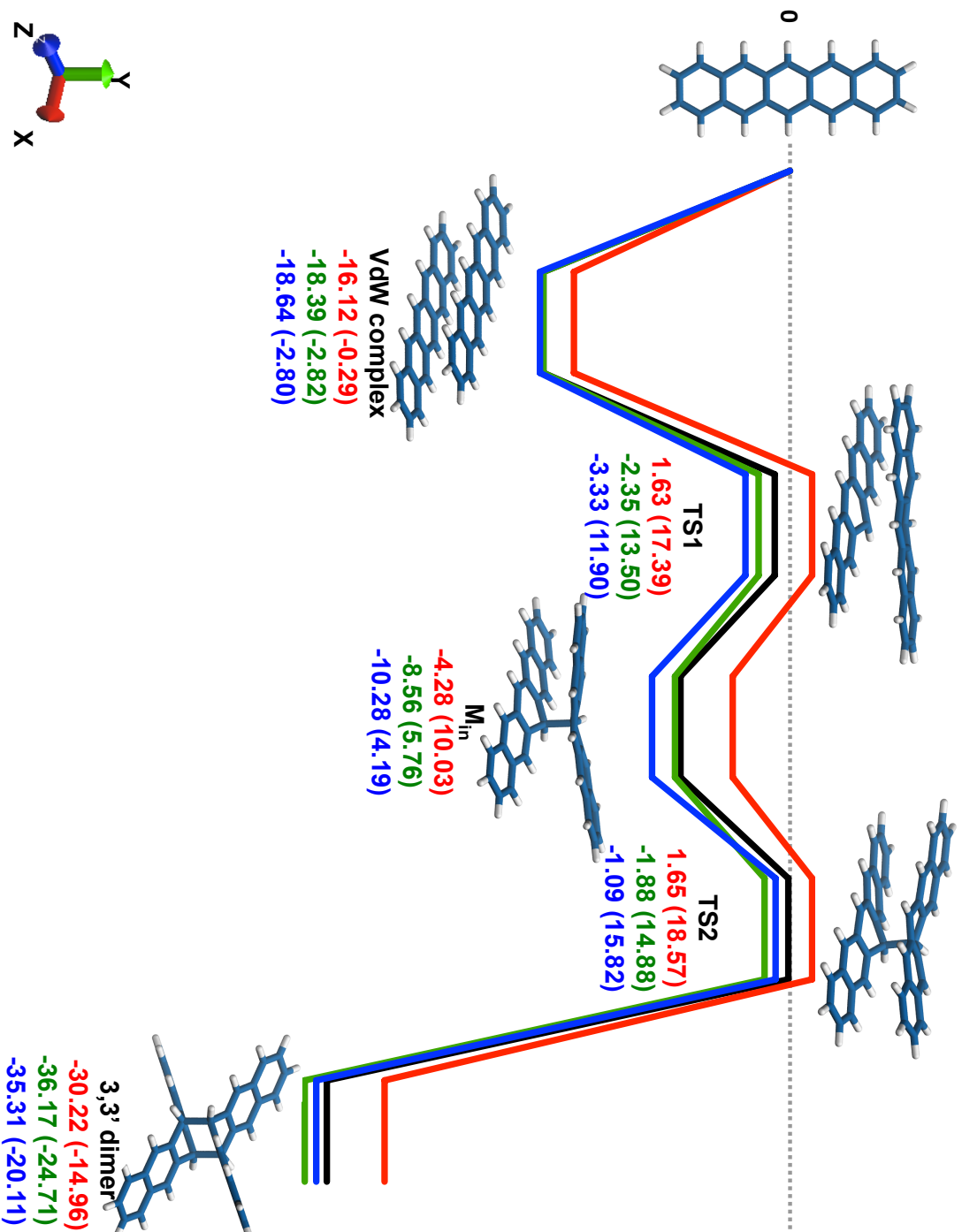
Figure 5.3: Pentacene dimerization scheme in the presence of an applied electric field of 3 V/nm along X (red line), Y (green line) or Z (blue line). X corresponds to the pentacene long axis, Y to the direction of the sp^3 bonds, and Z to the short axis. The black line refers to the reaction path in the absence of an applied electric field. The relative energies with ZPVE and Gibbs free energies in parentheses are calculated with respect to two isolated pentacene molecules (see Table 5.2. Reproduced from [9].

characterized without an applied electric field; then, the stationary points were re-optimized in the presence of a uniform electric field of 1, 2 or 3 V/nm along the three cartesian axes, where X corresponds to the pentacene long axis, Y to the direction of the sp^3 bonds, and Z to the short axis. DFT simulations were performed at level M06-2X/6-31G*. For the calculation of biradical intermediates M_{in}, TS1 and TS2, the unrestricted form UM06-2X/6-31G* was used instead.

The results reported in Tables 5.2 and 5.3 and Figures 5.1, 5.2 and 5.3 show that, although the electric field lowers the absolute energy of all intermediates, not all the species involved in the dimerization are stabilized equally respect to each other, or in comparison with two isolated pentacene molecules. Also, the direction of the field is fundamental to determine which intermediate is most favored and thus affects the dimerization energy.

The strongest effect is found when the electric field lies parallel to the pentacene long axis, the most polarizable direction. In this case, while all reaction intermediates fall very low in energy, they are still less stable than two isolated pentacenes. As a consequence, dimerization energy is lowered (up to 4.4 kcal mol^{-1}) with an electric field applied along the X direction (see Table 5.2). The 3,3' dimer is the less favored species. The effect is probably due to the eclipsed configuration of the anthracene "wings" that lie on the same side of the single bonds, which have the same charge and cannot readjust much to minimize Coulomb repulsion (see Figure 5.4). When the field magnitude is higher than 1 V/nm, the energy of the transition states is particularly high respect to the minima; this is probably caused by the higher electronic density in correspondence to the incipient C-C' bonds. This situation could reproduce the effect of the gate bias in an OFET.

The Y and Z directions of the electric field correspond roughly to the direction of the applied source-drain bias in an OFET. When the electric field is directed along Y, corresponding to the direction of incipient C-C' bonds, the dimer is the most stabilized species. At the same time, the Van der Waals complex is destabilized by the electric field; this results in a higher dimerization energy (see Table 5.2). Furthermore, in the same conditions the transition states are more stabilized; this results in the lowering of reaction barriers **3** and **4**, as reported in Table 5.1. Overall, the cycloaddition is more exothermic. In addition, Tables 5.2, 5.3 and 5.1 show that the effect of an electric field along the Z direction is to destabilize the Van der Waals complex while stabilizing the dimer. This situation also increases the dimerization energy, even if the formation of the second bond appears to be less favored if a stronger electric field is used.

Finally, in order to interpret the results, some symmetry considerations must be carried out. While the product, and to a lesser extent, the Van der Waals complex, are symmetric with respect to all the directions of the electric field, the biradicaloid

85

species are not. Therefore, the effect of an applied field along the Y or Z directions is reversed with an opposite direction of the electric field or with inverted atomic coordinates.

To summarize, the results indicate that pentacene cycloaddition may be enhanced by the applied source-drain bias in working OFET devices, while the effect of gate bias may instead reduce the exothermicity of dimerization. As suggested by previous studies, [21] pentacene dimerization may take place in disordered domains and particularly at grain boundaries of polycrystalline thin films. During OFET operation, the synergic effect of the applied electric field and, possibly, some other factors such as a low surface energy of the dielectric interface, could slowly affect the device performances leading to a lower mobility. This phenomenon is different from what is commonly defined as bias stress, which is mostly attributed to charge trapping: while the latter is reversible, dimerization would result in an irreversible loss of charge carrier density. This has been observed in a previous study, where such deterioration of the OFET performances was detected even in the absence of oxygen and light. [25]

5.3 Molecular reorientation in pentacene OFETs during operation

The OFETs studied here feature six-to-ten monolayer (ML) thick pentacene thin films. The OFET is schematically depicted in Figure 5.5. Channel length and width are 300 μm and 10 mm, respectively. This channel length is larger than typical devices: this setup allows the X-ray beam to probe the channel region during device operation, avoiding the electrodes.

The time dependent evolution of pentacene structure during OFET operation was studied by monitoring changes in different electrical and structural parameters, as detailed in the following discussion.

Out-of-plane reorientation

In order to sample the preferred orientation in the films along the (001) periodicity, rocking-curve (RC) experiments were performed. This measurement is performed by rocking the thin-film sample while the detector is kept a fixed angle. The obtained diffraction intensities arise from the differently oriented lattice planes. Thus, the rocking curve profile yields the orientation distribution in the film, as shown in Figure 5.6 b.

During operation, the RC peak was found to shift towards smaller angles. In more detail, after six hours at $V_{GS} = V_{DS} = $ -20 V, the RC peak shifted by 2×10^{-3} and

Table 5.1: Reaction barrier heights in kcal/mol: absolute energies including ZPVE and Gibbs free energies, in bold. Reproduced from [9].

E. Field (V/nm)		Reaction barrier									
		1		**2**		**3**		**4**		**5**	
	0	*18.37*	*2.80*	*17.23*	*17.38*	*7.04*	*9.12*	*8.05*	*11.65*	*34.39*	*36.45*
X	1	17.53	**1.75**	16.68	**16.62**	6.43	**7.75**	7.14	**9.63**	33.96	**35.68**
	2	17.00	**1.21**	17.09	**17.04**	6.44	**7.80**	6.62	**9.13**	32.93	**34.60**
	3	16.12	**0.29**	17.75	**17.68**	5.91	**7.36**	5.93	**8.54**	31.86	**33.53**
Y	1	17.72	**1.93**	16.32	**16.22**	6.36	**7.65**	7.17	**9.58**	34.15	**35.80**
	2	17.94	**2.22**	15.99	**15.91**	6.15	**7.41**	7.03	**9.65**	34.17	**35.98**
	3	18.39	**2.82**	16.03	**16.32**	6.21	**7.74**	6.68	**9.12**	34.29	**39.59**
Z	1	17.64	**1.87**	16.42	**16.27**	6.52	**7.73**	7.45	**9.91**	34.56	**35.92**
	2	17.44	**1.66**	16.02	**15.72**	6.82	**7.87**	8.13	**10.58**	34.12	**35.84**
	3	18.64	**2.80**	15.31	**14.70**	6.95	**7.71**	9.19	**11.63**	34.22	**35.93**

Table 5.2: Stabilization energies (including ZPVE) and Gibbs free energies at 298 K (in bold) for the reaction starting point (VdW complex), transition states (TS1 and TS2), local minimum (M$_{in}$) and product (3,3'-dimer), relative to the energy of two isolated pentacene molecules, in kcal/mol, obtained at level (U)M06-2X/6-31G*. Reproduced from [9].

E. Field (V/nm)		WdV complex	TS1	M$_{in}$	TS2	3,3' dimer
0		*-18.37* / **-2.80**	*-1.14* / **14.58**	*-8.18* / **5.46**	*-0.13* / **17.11**	*-34.52* / **-19.34**
X	1	-17.53 / **-1.75**	-0.85 / **14.87**	-7.28 / **7.12**	-0.14 / **16.75**	-34.10 / **-18.93**
	2	-17.00 / **-1.21**	0.09 / **15.83**	-6.34 / **8.03**	0.28 / **17.16**	-32.65 / **-17.44**
	3	-16.12 / **-0.29**	1.63 / **17.39**	-4.28 / **10.03**	1.65 / **18.57**	-30.22 / **-14.96**
Y	1	-17.72 / **-1.93**	-1.40 / **14.28**	-7.76 / **6.64**	-0.59 / **16.22**	-34.74 / **-19.58**
	2	-17.94 / **-2.22**	-1.95 / **13.69**	-8.10 / **6.28**	-1.07 / **15.93**	-35.24 / **-20.05**
	3	-18.39 / **-2.82**	-2.35 / **13.50**	-8.56 / **5.76**	-1.88 / **14.88**	-36.17 / **-24.71**
Z	1	-17.64 / **-1.87**	-1.22 / **14.40**	-7.74 / **6.67**	-0.30 / **16.58**	-34.85 / **-19.34**
	2	-17.44 / **-1.66**	-1.42 / **14.05**	-8.24 / **6.18**	-0.11 / **16.76**	-34.23 / **-19.08**
	3	-18.64 / **-2.80**	-3.33 / **11.90**	-10.28 / **4.19**	-1.09 / **15.82**	-35.31 / **-20.11**

88

Table 5.3: Stabilization energies (including ZPVE) and Gibbs free energies at 298 K (in bold) for the reaction starting point (VdW complex), transition states (TS1 and TS2), local minimum (Min) and product (3,3'-dimer), relative to the energy in absence of an applied electric field, in kcal/mol, obtained at level (U)M06-2X/6-31G*. Reproduced from [9].

E. Field (V/nm)		Pentacene		VdW complex		TS1		M_{in}		TS2		3,3'-dimer	
X	1	-1.23	**-1.20**	-0.38	**-0.16**	-0.94	**-0.91**	-0.33	**0.45**	-1.24	**-1.57**	-0.81	**-0.79**
	2	-5.12	**-5.09**	-3.74	**-3.50**	-3.88	**-3.83**	-3.28	**-2.51**	-4.71	**-5.03**	-3.24	**-3.18**
	3	-11.63	**-11.59**	-9.37	**-9.08**	-8.86	**-8.78**	-7.73	**-7.02**	-9.85	**-10.13**	-7.32	**-7.20**
Y	1	-0.15	**-0.14**	0.50	**0.72**	-0.41	**-0.44**	0.27	**1.04**	-0.61	**-1.03**	-0.37	**-0.37**
	2	-0.78	**-0.80**	-0.35	**-0.22**	-1.60	**-1.69**	-0.70	**0.02**	-1.72	**-1.99**	-1.50	**-1.51**
	3	-1.80	**-1.84**	-1.81	**-1.86**	-3.01	**-2.91**	-2.18	**-1.54**	-3.55	**-4.07**	-3.45	**-3.46**
Z	1	-0.48	**-0.46**	0.26	**0.48**	-0.56	**-0.63**	-0.04	**0.76**	-0.64	**-0.99**	-0.81	**-0.45**
	2	-2.11	**-2.08**	-1.18	**-0.95**	-2.39	**-2.61**	-2.17	**-1.36**	-2.09	**-2.43**	-1.82	**-1.81**
	3	-3.31	**-3.32**	-3.57	**-3.32**	-5.50	**-5.99**	-5.41	**-4.59**	-4.27	**-4.61**	-4.09	**-4.09**
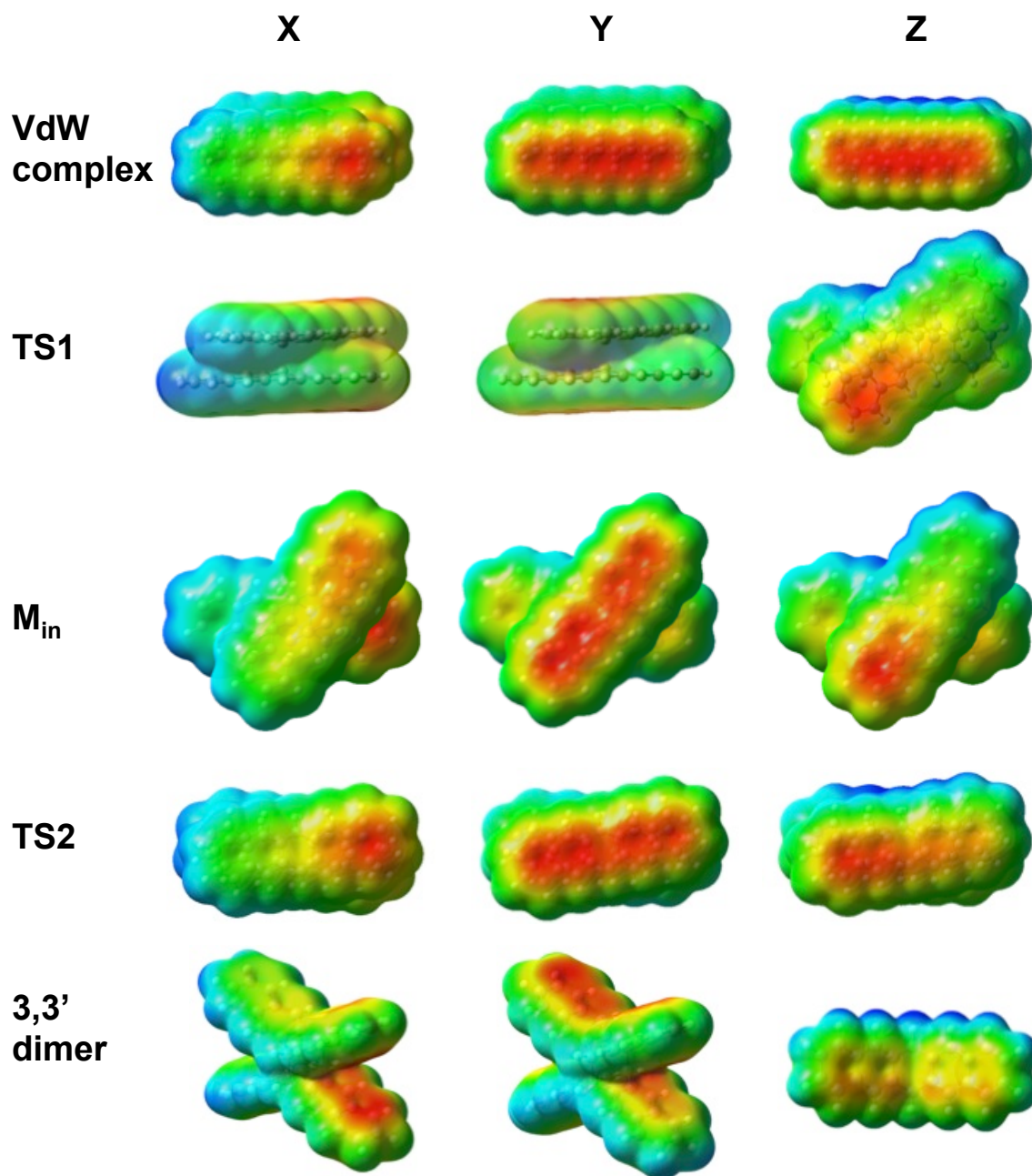
Figure 5.4: Electrostatic potential maps for all stationary points optimized with an electric field of 3 V/nm along X, Y and Z. In the color code, blue (red) indicates positively (negatively) charged areas. Reproduced from [9].

Table 5.4: C-C' bond length (in Å) and C-C-C'-C' dihedral angle (in degrees) for the transition states (TS1 and TS2), the intermediate M_{in} and the 3,3'-dimer.

E. Field (V/nm)		TS1		M_{in}		TS2		3,3'-dimer	
		C-C'	C-C-C'-C'	C-C'	C-C-C'-C'	C-C'	C-C-C'-C'	C-C'	C-C-C'-C'
X	1	2.039	43.05	1.616	58.40	1.656	13.33	1.607	0.00
	2	2.039	42.96	1.616	58.13	1.657	13.19	1.608	0.00
	3	2.039	42.81	1.618	57.64	1.658	13.13	1.609	0.00
Y	1	2.037	43.03	1.616	58.43	1.656	13.38	1.607	0.04
	2	2.034	42.94	1.616	58.23	1.657	13.84	1.607	0.08
	3	2.018	42.76	1.618	57.84	1.658	15.40	1.607	0.12
Z	1	2.041	43.25	1.616	58.71	1.656	13.50	1.607	0.00
	2	2.043	43.60	1.616	59.21	1.656	13.71	1.607	0.00
	3	2.047	44.25	1.616	59.84	1.656	13.91	1.607	0.00
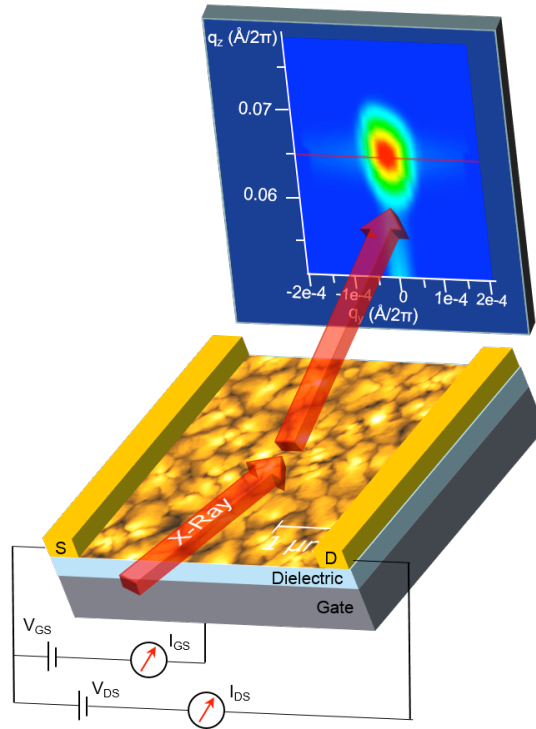
Figure 5.5: Schematics of the experimental OFET setup, reporting an AFM image of the pentacene thin film and the X-ray incident beam, together with the corresponding reciprocal space map around the (001) reflection of the pentacene thin film. Reproduced from [27].

the threshold voltage, V_{TH} shifted from 0V to -1.7 V. This variations are reversible, i.e. they are visible when a gate bias is applied and they return to the initial value when the bias is switched off to re-appear when gate bias is re-applied. The RC shift without any intensity decrease could be ascribed to a lattice expansion along the film thickness (i.e. molecular layer thickness) of 0.016Å, due to a molecular tilt of 2.3 mrad towards the surface normal axis. This was also confirmed by the shift of the Bragg peak, detected via 2D grazing incidence diffraction (2DGIXD), before and after applying $V_{GS} = V_{DS} = $ -30 V for one hour.

Interestingly, when a significant leakage current appears the RC peak shifts back following the same trend observed when transistor is switched off. This behaviour can be due to the fact that when the leakage current increases, the effective electric field in the transistor channel decreases, pointing out the relationship between the vertical electric field effect and the pentacene structural vertical stress.
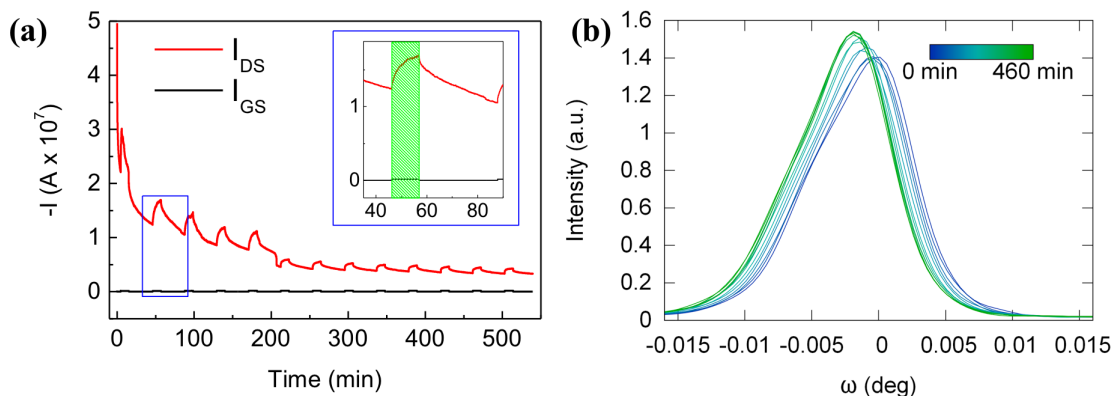
Figure 5.6: a) Electrical response of the device during the experiment. The green box in the inset indicates the time when an XRD scan is performed. The increase of the I_{DS} is due to the photocurrent generated upon X-ray irradiation of the sample. b) Rocking curve (RC) experiment showing the shift in the RC peak during OFET operation. Reproduced from [27].

In-plane reorientation

The evolution of the in-plane structure was followed by collecting 2D GIXD images around the strongest in-plane reflection {11}, when applying $V_{GS} = V_{DS} = $ -40 V. After 120 minutes of applied bias, the intensity increases, however neither a significant shift nor a width change can be detected. This indicates that both in-plane lattice parameter and the lateral domain coherence remain constant, the latter being estimated equal to 58 nm [33]. The in-plane peak evolution can be explained as an improvement of the crystalline order during OFET operation. This effect can be attributed to the healing of point defects inside crystal domains, and to the molecular rearrangement at both grain boundaries and terrace edges, where molecules can lie planar as demonstrated by AFM and STM measurements, [7] or adopt a configuration that differs from that of the crystal phase. [2]

Computational study

In order to corroborate and understand the experimental findings, computational studies were performed on two different systems. The first one concerned four pentacene molecules in vacuum forming a tetramer, without periodicity constraints. DFT calculations performed at level M06-2X/6-31G* [34] have shown that in the absence of electrical field tetramer stabilizes in a structure (named A in Figure 5.7 a) more compact and at lower energy than the thin film phase structure [35, 36] (structure B in Figure 5.7 b). In the second system, pentacene molecules were

Table 5.5: Optimization of lattice parameters and atomic coordinates for a supercell made of 24 pentacene molecules, with an applied electric field simulating gate voltage.Reproduced from [27].

El. Field (V/nm)	Rel. Energy[a] (kcal mol^{-1})	ϑ_{tilt}[b] (°)	Optimized lattice parameters				
			a (Å)	b (Å)	α(°)	β(°)	γ(°)
0	-	0.58	24.9172	21.5002	81.39	95.48	89.99
0.5	-0.013	0.33	24.9214	21.5019	81.46	95.75	90.01
1	-0.110	0.32	24.9129	21.5036	81.38	95.88	89.98
1.5	-0.218	0.36	24.9142	21.5038	81.36	95.83	89.99
2	-0.353	0.32	24.9043	21.5122	81.45	95.73	90.01

[a] Relative energies are calculated with respect to the structure optimized without applied electric field.

[b] The tilt angle is measured respect to the z axis, normal to the thin film surface.

constrained in the periodic structure of the thin film phase [35] on top of an implicit surface that corresponds to the SiO_2 surface in the experimental setup. Molecular dynamics simulations on the thin film were performed using an in-house modified version of the TINKER software suite [37, 38], with MM3 [39–41] force field and charges derived from the charge equilibration (QEq) [42] scheme. The implicit surface was modelled using a shallow Lennard-Jones 6-3 potential with a minimum depth of 0.5 kcal mol^{-1}. The gate bias was implemented for each atom as an applied potential along the normal to the surface, multiplied by the QEq charge (calculated in the absence of the external potential). A full crystal minimization was performed using MD calculations. The charges were initially fixed and not recalculated during the minimization. In this case the vertical electrical field slightly affects the crystal structure (see Table 5.5), causing the molecules to align to the vertical axis and reducing the tilt angle from 0.56°(0 V/nm) to 0.32°(1 V/nm).

By applying a field of 1V/nm, molecules tilt only 2 mrad (0.11°) towards the direction normal to the surface, according to the experimental results. In the MD simulations, the applied field is higher than the real one and the strain effect response is almost immediate respect to the several hours needed to observe the Bragg peak shift. These discrepancies can be explained as follows. First of all, due to the algorithm used to simulate the external electric field, the simulations were constrained to only 1 monolayer (ML). However, XRD measurements probe the full film depth (6 or 10MLs), where molecules are constrained by the upper neighbors potentially restricting their degrees of freedom. Moreover, the simulated

94
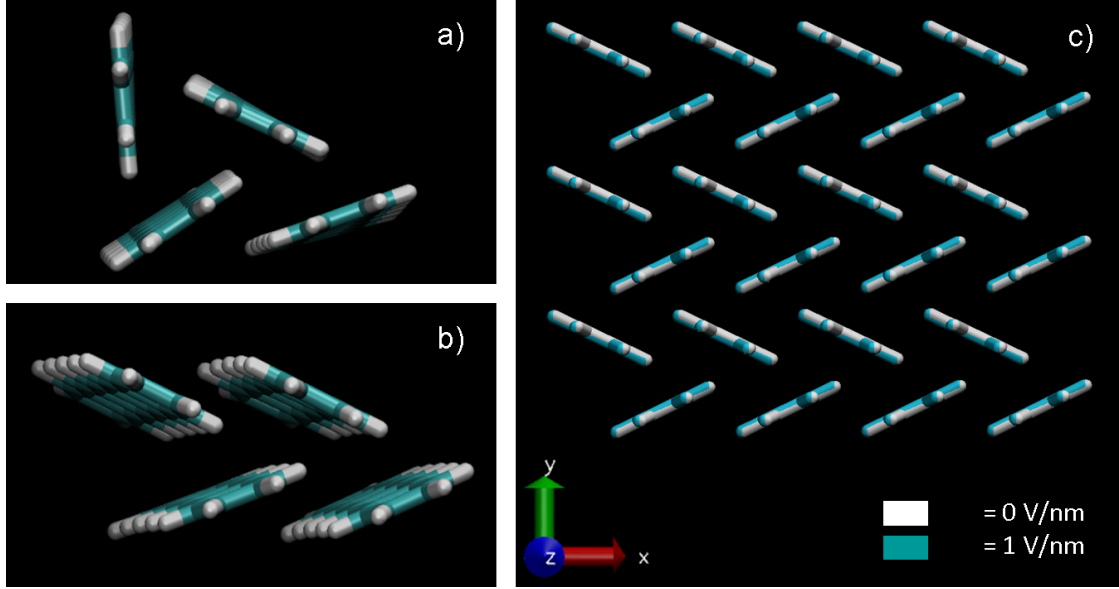
Figure 5.7: Representation of structure A (a) and structure B (b) of a tetramer in vacuum and the thin film phase. c) Optimization of lattice parameters and atomic coordinates for a supercell made of 24 pentacene molecules (see Table 5.5). with an applied electric field along the z direction simulating gate voltage. The optimized structures at 0 V/nm (white) and 1 V/nm (cyan) are reported. Reproduced from [27].

electric field is constant, while in the real system each layer screens the upper ones from the transversal electric field, reducing the field effect until the fourth ML, as deduced from the effective Debye length calculated on films grown in the same conditions. [3] The tetramer field-induced reorganization can be associated to situations having a lower molecular packing than the bulk crystal, for instance, at grain boundaries and terrace edges. The presence of a field may modify these structures toward the crystalline one, thus explaining the increasing of the in-plane peak intensity as a structural ordering. Due to the small amount of molecules forming the grain boundaries, the crystal domain size remains mostly unaffected by the molecular reorganization justifying why the in-plane Bragg peak width is unchanged, regardless of the OFET operation. The change of packing motif at the grain boundaries may also perturb the charge hopping between crystal grains [31]: molecules reorganizing according to the molecular packing of the closest crystalline grain may open a gap between two crystalline grains creating, therefore, charge traps [30]. It follows that this phenomenon may be related with the V_{TH} variation, thus to the bias stress, introducing a new scenario for the understanding of charge transport where OFET operation does not only depend on the of the

semiconductor film structure, but also on how the latter responds to the applied field and modulates the carrier transport over time.

5.4 Conclusion

The reaction path of pentacene [4+4] thermal cycloaddition was characterized in the presence of an electric field. If the latter is applied along the molecular long axis, dimerization is less favored due to the destabilization of the 3,3' product. On the other side, the "butterfly dimer" is particularly favored if the field is normal to the pentacene long axis. This relates also to the alignment of the electric field generated in OFETs, with the gate-source bias V_{GS} and drain-source bias, V_{DS} that would thus respectively disfavor and enhance the dimerization. Therefore, pentacene dimerization could be enhanced in correspondence to grain boundaries or amorphous domains. Since the dimer is by far more stable than pentacene, dimerization would result in an irreversible loss of possible charge carriers, thus decreasing the OFET performances. Pentacene dimerization could therefore contribute to the irreversible mobility loss that is observed after long operation time. [25] This study ultimately represents a further step towards the understanding of the phenomenon of fatigue in pentacene-based OFETs.
XRD measurements were performed in real time on pentacene-based OFETs, detecting small structural modifications induced by the electric field during the transistor operation. The experimental results, coupled with the computational studies, showed that the application of a transversal electrical field (V_{GS}) slightly perturbs the molecular arrangement by inducing a molecular tilt towards the applied field direction. In addition, molecules seem to re-organize at grain boundaries causing a V_{TH} shift, characteristic of the bias tress phenomenon. The structural modification was observed on apolar molecules arranged in high crystalline and high textured crystal grains. This phenomena may be more intense for polar molecules and/or disordered system, opening up a new prospective to the interpretation of charge transport in organic materials.

Bibliography

[1] F. Dinelli, M. Murgia, P. Levy, M. Cavallini, F. Biscarini and D. M. De Leeuw, *Phys. Rev. Lett.*, **2004**, 92, 116802.

[2] F. Liscio, C. Albonetti, K. Broch, A. Shehu, S. D. Quiroga, L. Ferlauto, C. Frank, S. Kowarik, R. Nervo, A. Gerlach, S. Milita, F. Schreiber and F. Biscarini, *ACS Nano*, **2013**, 7, 1257-1264.

[3] A. Shehu, S. D. Quiroga, P. D'Angelo, C. Albonetti, F. Borgatti, M. Murgia, A. Scorzoni, P. Stoliar and F. Biscarini, *Phys. Rev. Lett.*, **2010**, 104, 246602.

[4] M. Mas-Torrent and C. Rovira, *Chem. Rev.*, **2011**, 111, 4833-4856.

[5] R. Pfattner, M. Mas-Torrent, I. Bilotti, A. Brillante, S. Milita, F. Liscio, F. Biscarini, T. Marszalek, J. Ulanski, A. Nosal, M. Gazicki-Lipman, M. Leufgen, G. Schmidt, W. M. Laurens, V. Laukhin, J. Veciana and C. Rovira, *Adv. Mater.*, **2010**, 22, 4198-4203.

[6] S. Kowarik, A. Gerlach, S. Sellner, F. Schreiber, L. Cavalcanti and O. Konovalov, Phys. Rev. Lett., **2006**, 96, 125504-125507.

[7] F. Dinelli, C. Albonetti and O. V. Kolosov, *Ultramicroscopy*, **2011**, 111, 267-272.

[8] R. Li, J. W. Ward, D. M. Smilgies, M. M. Payne, J. E. Anthony, O. D. Jurchescu and A. Amassian, *Adv. Mater.*, **2012**, 24, 5553-5558.

[9] M. Matta, F. Zerbetto, F. Biscarini, *in preparation*, **2015**.

[10] Q. Ye and C. Chi, *Chem. Mater.*, **2014**, 26, 4046-4056.

[11] P. A. Bobbert, A. Sharma, S. G. J. Mathijssen, M. Kemerink and D. M. De Leeuw, *Adv. Mater.*, **2012**, 24, 1146-1158.

[12] R. Reddy and M. Bendikov, *Chem. Commun. (Camb).*, **2006**, 1179-1181.

[13] B. H. Northrop,O K. N. Houk and A. Maliakal, *Photochem. Photobiol. Sci.*, **2008**, 7, 1463-1468.

[14] A. Maliakal, K. Raghavachari, H. Katz, E. Chandross and T. Siegrist, *Chem. Mater.*, **2004**, 16, 4980-4986.

[15] S. Li, Z. Li, K. Nakajima, K. Kanno and T. Takahashi, *Chem. Asian J.*, **2009**, 4, 294-301.

[16] S. H. Chan, H. K. Lee, Y. M. Wang, N. Y. Fu, X. M. Chen, Z. W. Cai and H. N. C. Wong, *Chem. Commun. (Camb).*, **2005**, 66-68.

[17] P. Coppo and S. G. Yeates, *Adv. Mater.*, **2005**, 17, 3001-3005.

[18] S. S. Zade, N. Zamoshchik, A. R. Reddy, G. Fridman-Marueli, D. Sheberla and M. Bendikov, *J. Am. Chem. Soc.*, **2011**, 133, 10803-10816.

[19] S. S. Zade and M. Bendikov, *J. Phys. Org. Chem.*, **2012**, 25, 452-461.

[20] N. Zamoshchik, S. S. Zade and M. Bendikov, *J. Org. Chem.,* **2013**, 78, 10058-10068.

[21] M. Mottaghi and G. Horowitz, *Org. Electron. physics, Mater. Appl.*, **2006**, 7, 528-536.

[22] T. Mandal, A. Garg and Deepak, *J. Appl. Phys.*, **2013**, 114. 154517.

[23] H. L. L. Cheng, W. Y. Y. Chou, C. W. W. Kuo, Y. W. W. Wang, Y. S. S. Mai, F. C. C. Tang and S. W. W. Chu, *Adv. Funct. Mater.*, **2008**, 18, 285-293.

[24] H.-J. Kim, X. Wang, J. Ma and J.-H. Cho, *Chem. Phys. Lett.*, **2011**, 516, 141-145.

[25] C. Di, G. Yu, Y. Liu, Y. Guo, X. Sun, J. Zheng, Y. Wen, Y. Wang, W. Wu and D. Zhu, *Phys. Chem. Chem. Phys.*, **2009**, 11, 7268-7273.

[26] Y. Zhao and D. G. Truhlar, *Acc. Chem. Res.*, **2008**, 41, 157-167.

[27] F. Liscio, L. Ferlauto, M. Matta, R. Pfattner, M. Murgia, C. Rovira, F. Zerbetto, S. Milita and F. Biscarini, *in preparation*, **2015**.

[28] W. H. Lee, J. H. Cho and K. Cho, *J. Mater. Chem.*, **2010**, 20, 2549.

[29] D. Gentili, F. Valle, C. Albonetti, F. Liscio and M. Cavallini, *Acc. Chem. Res.*, **2014**, 47, 2692-2699.

[30] P. Annibale, C. Albonetti, P. Stoliar and F. Biscarini, *J. Phys. Chem. A*, **2007**, 111, 12854-12858.

[31] J. Rivnay, L. H. Jimison, J. E. Northrup, M. F. Toney, R. Noriega, S. Lu, T. J. Marks, A. Facchetti and A. Salleo, *Nat. Mater.*, **2009**, 8, 952-958.

[32] D. Gentili, F. Di Maria, F. Liscio, L. Ferlauto, F. Leonardi, L. Maini, M. Gazzano, S. Milita, G. Barbarella and M. Cavallini, *J. Mater. Chem.*, **2012**, 22, 20852-20856.

[33] B. E. Warren, *X-ray diffraction*, Dover: New York, **1990**.

[34] Y. Zhao and D. G. Truhlar, *Acc. Chem. Res.*, **2008**, 41, 157-167.

[35] S. Schiefer, M. Huth, A. Dobrinevski and B. Nickel, *J. Am. Chem. Soc.*, **2007**, 129, 10316-10317.

[36] A. Brillante, I. Bilotti, R. G. Della Valle, E. Venuti, A. Girlando, M. Masino, F. Liscio, S. Milita, C. Albonetti, P. D'Angelo, A. Shehu and F. Biscarini, *Phys. Rev. B - Condens. Matter Mater. Phys.*, **2012**, 85.

[37] TINKER Software Tools for Molecular Design. http://dasher.wustl.edu/tinker

[38] N. Sändig and F. Zerbetto, *Chem. Commun. (Camb).*, **2010**, 46, 667-676.

[39] N. L. Allinger, Y. H. Yuh and J. H. Lii, *J. Am. Chem. Soc.*, **1989**, 111, 8551-8566.

[40] J. H. Lii and N. L. Allinger, *J. Am. Chem. Soc.*, **1989**, 111, 8576-8582.

[41] J. H. Lii and N. L. Allinger, *J. Am. Chem. Soc.*, **1989**, 111, 8566-8575.

[42] A. K. Rappé and W. A. Goddard III, *J. Phys. Chem.*, **1991**, 95, 3358-3363.

Conclusion

The subject of this dissertation has regarded the modeling of smart materials for organic electronic applications by means of various computational techniques, with the aim of shedding light on some molecular and supramolecular-scale processes that influence their efficiency. In particular, the charge and exciton transfer in liquid crystals has been studied, providing a rationale for the observed experimental results. Another focus of this thesis has concerned the investigation on the effect of electric fields in pentacene-based transistors, that has provided important insight for the interpretation of device characteristics. In both cases, the development of ad-hoc computational tools has been performed in order to achieve the desired results.

The photophysical and structural properties of OPE liquid crystals have been explored using a wide range of methods, including ab initio, molecular dynamics, semi-empirical and stochastic simulations. The results for the $Y_3N@C_{80}$-OPE diad have allowed to correctly identify the charge transfer state involved in the sensitized emission of the $Y_3N@C_{80}$ moiety, and provided support to structural data. This system is the first liquid crystalline endohedral metallofullerene, showing self-organizing and mesomorphic properties suitable for photovoltaic applications. As for the OPE aggregation in solution and in the LC state, the theoretical model implemented in this work has yielded a coherent picture of the molecular excitonic interactions by reproducing the spectroscopic features of the system. In this framework, the tuning of OPE aggregation is of great interest for their possible exploitation in stimuli-responsive LCs; this work represents therefore a starting point for the future implementation of OPE in sensing devices.

The algorithm developed for exciton dynamics simulation has been modified to describe a system made of self-assembled protonated porphyrins in a CNT matrix, discussed in the following chapter, Perspectives. Simulations on porphyrin H-J aggregates will be carried out with the aim of describing the extent of exciton localization in the aggregate, and will be compared to the results of molecular dynamic simulations on the aggregate. The latter require a careful parameterization of the porphyrin interactions with the counter-ion, the solvent and the CNT, that

is currently being carried on. The overall purpose of this research is to achieve a nanoscale description of the aggregate, together with the key parameters governing its self-assembly, and correlate it to its efficiency as a possible donor-acceptor system in organic solar cells.

The response of pentacene thin films to strong electric fields, modelled via ab initio and molecular mechanics simulations, has been investigated. The obtained results show that the source-drain bias can influence the reaction path of pentacene dimerization, enhancing the reaction by both lowering the barriers and stabilizing the "butterfly dimer". This observation can be related to the phenomenon of device fatigue, that translates in mobility loss over time, observed even in the absence of external agents. Furthermore, the effect of gate bias has been studied using molecular mechanics simulations performed on a pentacene monolayer. In agreement with experimental XRD measurements performed on operating devices, the simulated system shows a molecular reorientation along the direction of the applied electric field. Overall, these findings are particularly interesting due to the central role of pentacene in OFET technology, where still many unsolved issues persist. With this respect, even if the size of the simulated systems is small, the results presented in this thesis provide a new perspective on macroscopically observed phenomena such as fatigue and bias stress.

The systems studied throughout the present dissertation, although quite different from each other, are all being extensively studied for and employed in organic electronic devices. It is important to remark that, although computational methods have intrinsic limitation in terms of size and accuracy of the system that can be modelled, the information they convey allows to better understand the basic phenomena governing molecular behaviour in organic devices. Therefore, while their outcome is not always immediately transferable to practical applications, they represent a fundamental step towards their progress. To summarize this concept, the development of theoretical and computational models in the field of nano-structured devices has an indirect effect on their technological advancement. Once again, the results presented in this thesis highlight the importance of theoretical and computational modeling in the field of nanotechnology as an affordable and reliable tool able to complement and predict experimental results when dealing with the molecular building blocks of complex functional architectures.

Perspectives:
Self-assembled protonated
porphyrin-CNT systems for organic
solar cells

Based on a previous work by Hasobe and coworkers [1, 2], the self-assembly of a system made of protonated porphyrins and carbon nanotubes is investigated using MD simulations. Furthermore, the exciton dynamics of the porphyrins are studied using a specifically developed algorithm aim at reproducing the spectroscopic features of H-J aggregates formed in the CNT matrix. The aim of this work is to establish a relationship between the aggregate morphology and its photophysical properties, in order to exploit it as a nano structured donor-acceptor in photovoltaic devices. Being a work in progress, this chapter describes the fundamental framework regarding porphyrin-CNT aggregates and the preliminary steps of this research line, together with the experimental characterization of the system, in light of the general interest for such materials in organic solar cells.

.1 Photophysical properties of porphyrins

Porphyrins are a class of natural macrocyclic compounds involved in metabolic processes in animals and plants. Their structure is made of four pyrrole rings connected by methine bridges. Their highly conjugated π electron system gives them a characteristic UV-Visible absorption spectrum, that has two distinct sets of bands. The transitions from the ground state S_0 to the second excited state S_2, known as Soret bands or B bands, are located in the 380-500 nm region. Below, the transitions from the ground state to the first excited state, called Q bands, occupy the visible region (500-750 nm), have a much lower oscillator strength. The absorption spectrum of porphyrins can be interpreted using the Gouterman
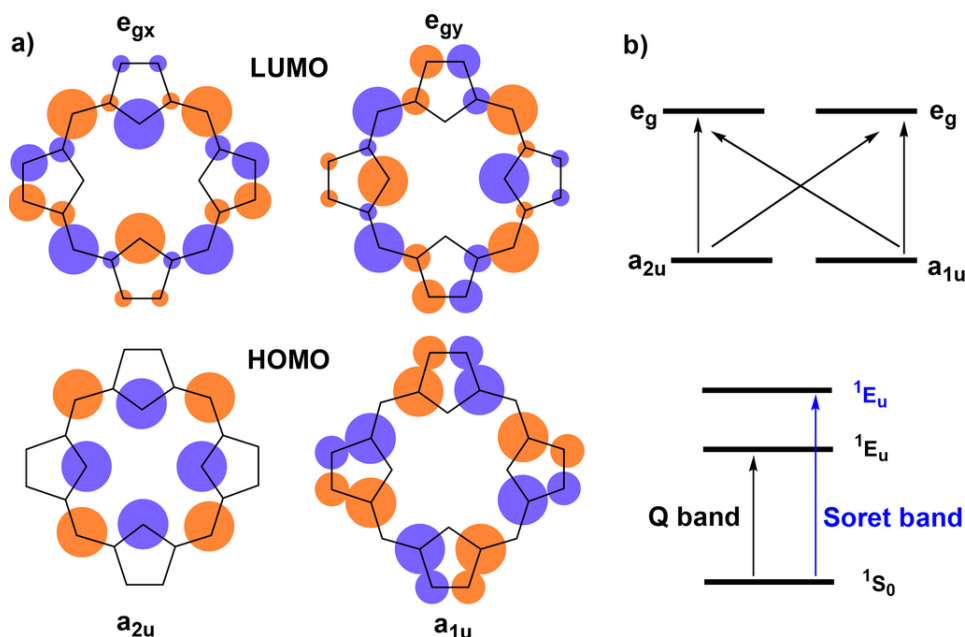
Figure 1: a) Frontier orbitals involved in porphyrin transitions; the two degenerate HOMOs (LUMOs), at the bottom (top). b) Resulting transitions, divided respectively in forbidden Q-type and allowed B-type (or Soret) bands. Adapted from [5].

four-orbital model (see Figure 1), based on LCAO theory. The doubly degenerate HOMO and LUMO orbitals give rise to four possible transitions, two allowed ($\Delta M = \pm 1$) and two forbidden ($\Delta M = \pm 9$).

Porphyrin photophysics is highly sensitive to any changes in the molecular structure, like protonation or the binding of a metal. In these circumstances, the Q band structure is simplified due to the higher simmetry of the system. However, a substantial difference exists between metallated porphyrin and its diprotonated form: while the former is planar, the latter is distorted in a saddle-like geometry, where the pyrroles hydrogens are alternatively tilted above and below the porphyrin plane, together with their bound hydrogens (see Figure 2). [3, 4]

.2   Porphyrin aggregation

Aggregation has a major influence on the absorption spectra of porphyrins. The literature provides many examples of self-assembled systems made of charged porphyrins, especially those bearing charged substituents [6–17]. The aggregation

process is guided by the electrostatic interaction of the positively charged porphyrin core and the negative counter-ion. In neutral systems, instead, the only $\pi - \pi$ stacking interaction do not seem to be enough to provide long-range ordered structures. In the recent years, with the rapid popularity increase of CNTs, a parallel need to effectively disperse and solubilize them has found in porphyrins an ideal agent to promote CNT unbundling. [18–21] The interest in CNT-porphyrin aggregates, though, is mainly due to the possibility of coupling the light harvesting properties of porphyrins with the electron-acceptor behaviour of CNTs, thus obtaining a donor-acceptor system suitable for photovoltaic applications. [1, 2, 22, 23]

Hasobe and coworkers [1, 2] reported the formation of a rod-like, nanometer-size aggregate made of porphyrins and single-wall CNTs. The absorption spectrum of the aggregate in the UV region, only weakly affected by the presence of the carbon nanotubes, denotes the presence of two kinds of porphyrin-porphyrin interactions: a blue shifted band corresponding to H-aggregate formation and a red-shifted band corresponding to J-aggregate formation (see Figure 3). In the former, interacting porphyrins are presumed to be arranged on top of each other, while in the latter they are placed side by side, as reported in Figure 3.1. In more detail, the study involved three different porphyrins: a di-substituted one ($H_4P_2{}^+$), and two tetra-substituted ones ($H_4PTP_2{}^+$ and $H_4PtBuP_2{}^+$), reported in Figure 2. However, for the two tetra-substituted systems, the H-J aggregation was not observed, possibly due to their steric hindrance.
In order to investigate the structure and photophysical properties of the aggregate, the exciton coupling model presented in Chapter 4 has been modified to describe porphyrin H-J aggregates. This approach, coupled with MD simulations, could provide further details on the structure-properties relationship of this system.

.3   Modelling porphyrin-CNT aggregates

The atomistic study can help understand the dynamics of aggregate formation, together with the relative weight of many factors governing the aggregation process (e.g., the porphyrin counter-ion, the carbon nanotube role and the steric hindrance of the porphyrin substituents). The exciton simulations are parameterized against experimental spectroscopic data and allow to determine the exciton coherence length of the aggregate, which can be defined as the number of simultaneously excited molecules and is related to the degree of order in the aggregate. On the whole, not only these two methods will provide a clear picture of the system structure-properties relationship, but the outcome of MD simulations will serve as a "test bench" for the exciton model.

H₄P²⁺: R₁ = R₃ = H, R₂ = R₄ = 3,5-Di-tBuPh
H₄PTP²⁺: R₁ = R₂ = R₃ = R₄ = Ph
H₄PtBuP²⁺: : R₁ = R₂ = R₃ = R₄ = 3,5-Di-tBuPh
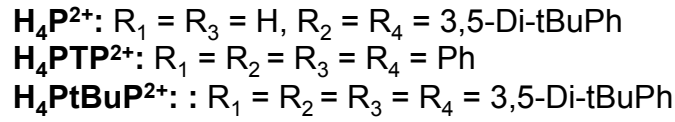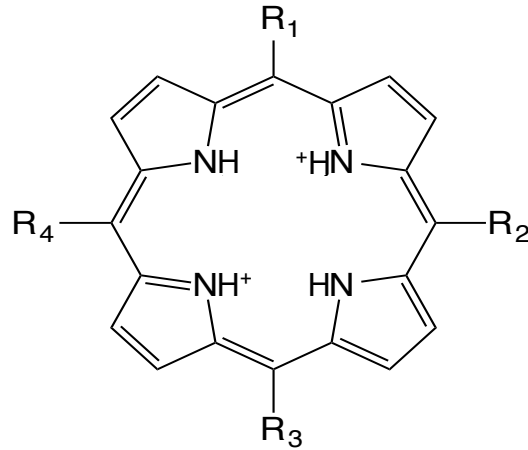
Figure 2: Doubly protonated porphyrins $\mathbf{H_4P_2^+}$, $\mathbf{H_4PTP_2^+}$ and $\mathbf{H_4PtBuP_2^+}$.

Exciton simulations

The exciton model [24] discussed in Chapter 4 has been modified to describe the absorption bands of H and J aggregates, where each one is treated as an independent mono-dimensional distribution although the entire aggregate is of course 3-dimensional. Respect to the previous model, two main changes have been made. First, when calculating the aggregate energies according to the equation:

$$E_k = E_0 + 2V cos\left(\frac{k\pi}{N+1}\right) \tag{1}$$

the value of k, that is the phase of the excited state corresponding to the observed transition, is set as 1 for the J aggregate (since the lowest excited state is populated) and N for the H aggregate (because the highest excited state is populated). The second difference involves the Gaussian distribution by which Equation 1 is multiplied. For H aggregates, a constant σ of 150 cm⁻¹ is used; for J aggregates, the broadening of the band is taken as

$$\sigma_{aggregate} = \frac{\sigma_{mono}\sqrt{N_0}}{\sqrt{N}} \tag{2}$$
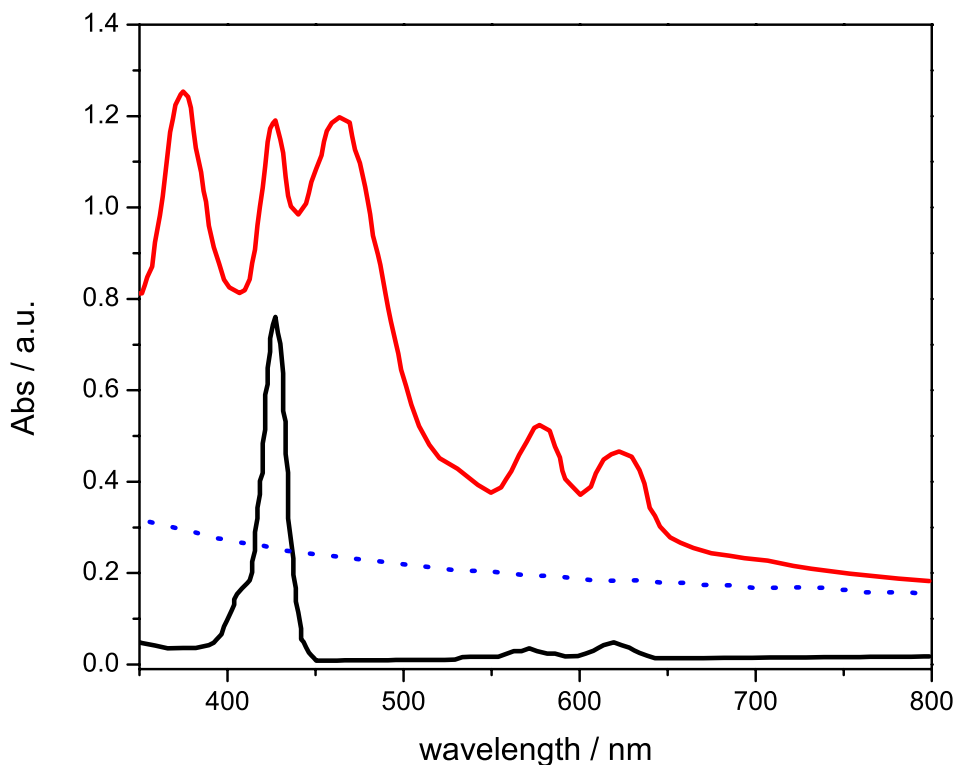
Figure 3: Absorption spectra of the $H_4P_2^+$- CNT aggregate (red), $H_4P_2^+$ (black), a suspension of CNTs (blue). Adapted from [1].

The J aggregate band in the porphyrin-CNT absorption spectrum appears to be quite broad, respect to the monomer. This is apparently in contrast with the theory of J aggregates, which predicts that the aggregate wavelength should increase as a function of $1/\sqrt{N}$. [25, 26] Therefore, the J band must be deconvolved into different components, and a separate fitting must be performed for each of them.

MD simulations

The size of the porphyrin-CNT aggregate being modelled requires the use of a quite sizable simulation box for MD. Furthermore, a reliable representation of the system must of course include a proper electrostatic treatment of the protonated porphyrin and its counter ion. Therefore, before proceeding to the actual simulation task, a parameterization step is required. As a preliminary step for the MD simulation of the system, the protonated porphyrins $H_4P_2^+$ and $H_4PTP_2^+$ were optimized at DFT level (PBE0/6-311+G*). The electrostatic potential was then used to derive atomic charges used for MD. The same procedure

was used for the sulfate counter-ion and the solvent (THF). In addition to this, a reparameterization of the torsion angles between the porphyrin ring and the phenyl substituent was performed. The other parameters were taken from the GAFF Force Field. [27]

As far as the CNTs are concerned, a single-wall nanotube with chiral indexes m = 14 and n = 0, was chosen as representative of the experimental sample. The MD simulations will then be run using initially one CNT, allowing the porphyrins to adjust around it; then, this minimal system will be replicated to reproduce a realistic environment for aggregate formation.

Bibliography

[1] T. Hasobe, S. Fukuzumi and P. V. Kamat, *J. Am. Chem. Soc.*, **2005**, 127, 11884-11885.

[2] T. Hasobe, S. Fukuzumi and P. V Kamat, *J. Phys. Chem. B*, **2006**, 110, 25477-25484.

[3] D.-M. Chen, X. Liu, T.-J. He and F.-C. Liu, *Chem. Phys.*, **2003**, 289, 397-407.

[4] A. Marcelli, P. Foggi, L. Moroni, C. Gellini, P. R. Salvi and I. J. Badovinac, *J. Phys. Chem. A*, **2007**, 111, 2276-2282.

[5] M. Senge, A. Ryan, K. Letchford, S. MacGowan and T. Mielke, Symmetry (Basel)., 2014, 6, 781-843.

[6] D. L. Akins, H.-R. Zhu and C. Guo, *J. Phys. Chem.*, **1996**, 100, 5420-5425.

[7] T. S. Balaban, R. Goddard, M. Linke-Schätzel and J.-M. Lehn, *J. Am. Chem. Soc.*, **2003**, 125, 4233-4239.

[8] S. C. Doan, S. Shanmugham, D. E. Aston and J. L. McHale, *J. Am. Chem. Soc.*, **2005**, 127, 5885-5892.

[9] T. Hasobe, *Phys. Chem. Chem. Phys.*, **2012**, 14, 15975-15987.

[10] K. Kano, K. Fukuda, H. Wakami, R. Nishiyabu and R. F. Pasternack, *J. Am. Chem. Soc.*, **2000**, 122, 7494-7502.

[11] N. C. Maiti, S. Mazumdar and N. Periasamy, *J. Phys. Chem. B*, **1998**, 102, 1528-1538.

[12] N. C. Maiti, M. Ravikanth, S. Mazumdar and N. Periasamy, *J. Phys. Chem.*, **1995**, 99, 17192-17197.

[13] O. Ohno, Y. Kaizu and H. Kobayashi, *J. Chem. Phys.*, **1993**, 99, 4128.

[14] R. F. Pasternack, K. F. Schaefer and P. Hambright, *Inorg. Chem.*, **1994**, 33, 2062-2065.

[15] J. M. Ribo, J. Crusats, J.-A. Farrera and M. L. Valero, *J. Chem. Soc. Chem. Commun.*, **1994**, 681.

[16] Z. Wang, C. J. Medforth and J. A. Shelnutt, *J. Am. Chem. Soc.*, **2004**, 126, 15954-15955.

[17] V. N. Zozulya, O. A. Ryazanova, I. M. Voloshin, M. M. Ilchenko, I. Y. Dubey, A. Y. Glamazda and V. A. Karachevtsev, *Biophys. Chem.*, **2014**, 185, 39-46.

[18] F. Cheng and A. Adronov, Chemistry, 2006, 12, 5053-5059.

[19] T. W. Ebbesen, *J. Phys. Chem. Solids*, **1996**, 57, 951-955.

[20] J. K. Sprafke, S. D. Stranks, J. H. Warner, R. J. Nicholas and H. L. Anderson, Angew. Chem. Int. Ed. Engl., **2011**, 50, 2313-2316.

[21] S. S. D. Stranks, J. J. K. Sprafke, H. H. L. Anderson and R. R. J. Nicholas, *ACS Nano*, **2011**, 5, 2307-2315.

[22] V. A. Karachevtsev, A. M. Plokhotnichenko, A. Y. Glamazda, V. S. Leontiev and I. A. Levitsky, *Phys. Chem. Chem. Phys.*, **2014**, 16, 10914-10922.

[23] M. R. Wasielewski, *Acc. Chem. Res.*, **2009**, 42, 1910.

[24] L. K. Gallos, A. V. Pimenov, I. G. Scheblykin, M. Van der Auweraer, G. Hungerford, O. P. Varnavsky, A. G. Vitukhnovsky and P. Argyrakis, *J. Phys. Chem. B*, **2000**, 104, 3918-3923.

[25] P. B. Walczak, A. Eisfeld and J. S. Briggs, *J. Chem. Phys.*, **2008**, 128, 044505.

[26] Y. Chen and J. Zhao, *Phys. B Condens. Matter*, **2011**, 406, 579-583.

[27] J. Wang, R. M. Wolf, J. W. Caldwell, P. A. Kollman and D. A. Case, *J. Comput. Chem.*, **2004**, 25, 1157-1174.

List of Figures

111

112

List of Tables